Experimental and Numerical Study of Heat Flow under Low-Enthalpy Hydrothermal Conditions

Proefschrift

ter verkrijging van de graad van doctor
aan de Technische Universiteit Delft,
op gezag van de Rector Magnificus prof.ir. K.C.A.M. Luyben,
voorzitter van het College voor Promoties,
in het openbaar te verdedigen
op 09 februari 2015 om 15:00 uur

door

SANAZ SAEID

Master of Science in Mining Engineering, Technical University of Tehran
geboren te Shahrood, Iran

Dit proefschrift is goedgekeurd door de promotor:

Prof. Dr. M. A. Hicks

Samenstelling promotiecommissie:

Rector Magnificus	voorzitter
Prof. Dr. M. A. Hicks	Technische Universiteit Delft, promotor
Dr. R. Al-Khoury	Technische Universiteit Delft
Prof. Dr. -Ing. R. Katzenbach	Technische Universität Darmstadt
Prof. Dr. R. J. Schotting	Utrecht University
Prof. Dr. D. F. Bruhn	Technische Universiteit Delft
Dr. K. H. A. A. Wolf	Technische Universiteit Delft
Dr. P. J. Vardon	Technische Universiteit Delft
Prof. Dr. Ir. T. J. Heimovaara	Technische Universiteit Delft, reservelid

Published and distributed by:

Sanaz Saeid

Section of Geo-Engineering

Faculty of Civil Engineering and Geosciences

Delft University of Technology

P.O. Box 5048, 2600 GA Delft, the Netherlands

E-mail: sanaz.saeid@gmail.com

ISBN/EAN: 978-94-6186-418-5

Published by: Uitgeverij BOXPress, ‘s-Hertogenbosch

Once you realize

*That **the road is the goal**,*

And that you are always on the road,

Not to reach a goal,

But to enjoy its beauty and its wisdom,

Life ceases to be a task,

And becomes natural and simple,

In itself and ecstasy…

-Sri Nisaragadatta Maharaj

Summary

Energy and its management and environmental impact constitute one of the most important issues in the 21st century. Since fossil fuels are environmentally hazardous and sooner or later are going to be depleted, there is a pressing need for alternatives. Renewable energies, such as solar, wind and geothermal energy are vital sources of energy that are clean and abundantly available. Wind and solar energy sources, in spite of their several advantages, are naturally intermittent. They might not be available at times of peak energy demands and abundant at times of no demand. On the contrary, geothermal energy is available at all times. This makes geothermal energy sources a plausible alternative to fossil fuels. Several types of geothermal energy sources are available, including high, intermediate, and low-enthalpy which have different applications. In countries with low thermal gradients and relatively high permeable aquifers, such as the Netherlands, geothermal energy can be used for space heating using hydrothermal heating plants.

A prerequisite to safe, economic and viable geothermal systems is a good understanding of the geology and the physical processes in the sub-surface. In a hydrothermal system, heat conduction and convection takes place in a rather highly disproportionate geometry. This combination of physical processes and geometry make numerical analysis of such a system complicated and resource-consuming. Hence, in developing numerical tools for geothermal systems, important efforts are devoted to tackling the discretization of two main issues: geometry and heat convection. Deep geothermal systems consist of very slender boreholes embedded in a large soil mass. This geometrical peculiarity exerts an enormous computational burden, as a combination of very fine elements (cells) and coarse elements (cells) is normally needed to discretize the physical domain. For three-dimensional systems, this normally requires hundreds of thousands to millions of elements, necessitating parallel computing using multiple processor computers and making the CPU times unrealistic for engineering practice. Additionally, heat flow in a hydrothermal system involves density and viscosity variation with temperature, and thermal dispersion. These phenomena make the problem non-linear and must be well understood and taken into consideration in optimizing a geothermal system.

In this thesis, these physical and geometrical issues have been studied experimentally and numerically. The objectives of this thesis are:

1. To investigate the variation of the formation fluid density and viscosity, with temperatures typically existing in hydrothermal conditions.
2. To investigate thermal dispersion due to heat flow in a porous domain.
3. To establish a discretization technique that covers all important features of the hydrothermal system geometry and physical processes, and, at the same time, is computationally efficient such that it can be run on a normal PC (500 MHz, 4GB RAM).
4. To formulate a prototype model for a preliminary estimation of the reservoir lifetime by knowing its porosity and initial temperature for different design parameters, namely, discharge, well spacing and injection temperature.

The outcome of the experimental-numerical study in this thesis emphasizes the significance of several manmade and physical parameters on the system lifetime. In conducting a viable design of a hydrothermal system, these parameters need to be carefully evaluated. The proposed prototype model can be utilized in the preliminary phases of a project, from which the project lifetime and consequently the cost and the amount of the extracted energy, can be estimated.

Samenvatting

Het energievraagstuk en de daarmee gepaard gaande milieuproblematiek is een van de meest dringende kwesties van de 21e eeuw. Aangezien fossiele brandstoffen milieuonvriendelijk zijn en zijn bovendien niet onuitputtelijk, is er meer en meer behoefte aan alternatieven. Duurzame energiebronnen zoals zonne-, wind- of geothermische energie (aardwarmte) zijn schoon en in ruime mate aanwezig. Het aanbod van wind- en zonne-energie is onderhevig aan fluctuaties; het is afhankelijk van de weersomstandigheden en kan niet altijd voldoen aan de pieken en dalen in de vraag. Geothermische energie daarentegen is ten alle tijde beschikbaar. Dit maakt geothermische energiebronnen een geschikt alternatief voor fossiele brandstoffen. Geothermische energiebronnen kunnen worden onderscheiden in vindplaatsen met hoge, midden en lage temperatuur (enthalpie); elk is geschikt voor verschillende toepassingen. In landen met een lage thermische gradiënt en waterbronnen met een hoge permeabiliteit, zoals in Nederland het geval is, kan geothermie gebruikt worden voor verwarming van ruimten met behulp van hydrothermale warmte units.

Een eerste vereiste voor een veilig en rendabel geothermaal systeem is een goed begrip van de geologie en ondergrondse fysische processen. In een hydrothermaal systeem geschieden warmtetransmissie en -convectie volgens heterogene modellen. De combinatie van ondergrondse processen en complexe warmte stromingen maakt numerieke analyse van dergelijke geo-systemen zeer ingewikkeld en het vergt veel rekenkracht. derhalve wordt er bij de ontwikkeling van numerieke modellen veel aandacht geschonken aan de discretisatie van zowel de geometrische component als als de warmteconvectie-component. Een specifieke uitdaging in de geometrie van geothermische systemen zijn de dunne boorgaten die in een volumineuze ondergrond zijn geplaats. Deze combinatie van gedetailleerde en grootschalige elementen (cellen) legt een grote druk op de rekenkracht bij het discretiseren van de fysieke ondergrond en putten. Voor drie-dimensionale systemen resulteert dit al snel in honderdduizenden tot miljoenen elementen; dat vereist een exceptionele grote rekenkracht, welke onrealistische is voor de dagelijkse praktijk. Daarbij komen nog temperatuur-afhankelijke parameters gerelateerd aan warmtestroming in hydrothermale systemen, zoals dichtheid en viscositeit. Deze verschijnselen maken het probleem niet-lineair en moeten dus goed worden begrepen om geothermische systemen te kunnen optimaliseren.

Dit proefschrift beschrijft experimentele en numerieke studies naar de bovengenoemde fysische en geometrische aspecten van geothermische systemen. De doelstellingen van dit proefschrift zijn:

1. Het onderzoeken van de vloeistofdichtheids- en viscositeitsvariaties van formatie vloeistoffen bij temperaturen die kenmerkend zijn voor in-situ hydrothermale systemen.
2. Het onderzoeken van thermische dispersie als gevolg van warmtestroming in een poreus medium.
3. Het opstellen van een discretisatietechniek die alle belangrijke eigenschappen van een hydrothermaal systeem kan behelzen, en die tegelijkertijd efficiënt is met rekenkracht, zodat het op eenpc kan worden uitgevoerd.
4. Het formuleren van een prototype model voor een levensduur beoordeling van een hydrothermaal systeem, uitgaande van een bekende porositeit en initiële temperatuur maar met variërende parameters zoals uitstroming, afstand tussen de boringen en injectietemperatuur.

De uitkomst van de experimenteel-numerieke studie in dit proefschrift benadrukt het belang van verschillende vooraf gedefinieerde en natuurlijke parameters voor de levensduur van het systeem. Voor het opstellen van een valide model voor een hydrothermaal systeem moeten deze parameters zorgvuldig worden gekozen. Het beschreven basis-model kan gebruikt worden voor de modelstudie voorafgaandaan een project, waarna de levensduur en vervolgens de kosten en de onttrokken energie ingeschat kunnen worden.

Contents

Chapter 1

Introduction

This chapter gives a brief description of geothermal energy and its utilization. Focus is placed on low-enthalpy geothermal resources, which constitutes the core topic of this thesis. An overview addressing current important experimental and numerical works for modeling low-enthalpy geothermal systems is given, followed by a summary of the work and objectives of this study.

1.1 Geothermal energy

Geothermal energy is a vast source of renewable energy stored in the interior part of the earth. Renewable energy is generally described as energy obtained from sources that are essentially inexhaustible, in contrast to the fossil fuels, which are depletable. Unlike other renewable energy sources, such as solar and wind, geothermal energy is continuous. The majority of the geothermal sources worldwide are of the medium-low enthalpy type (Franco and Vaccaro, 2014).

Local use of natural geothermal water for various heating purposes is old. It is anticipated that the presence of volcanoes, hot springs, geysers, and other thermal phenomena must have led ancient peoples to guess that parts of the interior of the earth were hot. The main utilization of geothermal heat was limited to using hot mineral springs for bathing and heating. In between the

sixteenth and seventeenth century, when the first mines were excavated to a few hundred metres below ground level, people understood that the earth's temperature increases with depth (Dickson and Fanelli, 2004). The first large scale commercial use of geothermal steam was at Larderello in Italy. This geothermal field has been producing electricity since 1904. After that, geothermal energy has been utilized commercially for electricity production in New Zealand, United States and Iceland, and recently in many other parts of the world.

In general, geothermal energy has experienced a considerable growth in the last 35 years. This is due to its attractive features such as: availability, independence on climate, broad range of applicability (depending on the geothermal reservoir conditions), and being environmentally friendly. It is foreseen that its use will be significantly increased by the development of production technologies, the easier transformation to other types of energy, and the ease in long distance transportation. Geothermal energy will have a significant share of the future global energy use, only if it can be offered at a reasonable price, compared to the fossil fuels (specifically oil). Fossil fuels prices are varying with market, economic, and political conditions. As a consequence, the competitiveness of geothermal energy varies accordingly, becoming more or less attractive in times of high or low oil prices, respectively (Clauser, 2006).

The ultimate source of geothermal energy is the immense heat stored within the earth. The sources of this heat are (Clauser, 2006): Radioactive decay of elements, gravity force, chemical reaction and crystallization, friction by tidal movement in the outer core and mantle, green-house effect, among others.

Earth heat can be divided into low-enthalpy and high-enthalpy resources. Enthalpy is a measure of the total energy of a thermodynamic system, equivalent to the system internal energy plus the product of pressure and its volume. The exact boundary between low and high enthalpy resources is not clear. Dickson and Fanelli (2013) present a table (Table 1-1) in which different classifications are proposed for low, intermediate, and high enthalpy geothermal sources by a number of authors. This table presents 5 different classifications, which shows a wide range of temperatures describing the low, intermediate and high enthalpy systems. In this thesis, the classification proposed by Benderitter & Cormy is followed as it suits the Netherlands' hyrothermal situation better.

Table 1-1. Classification of geothermal resources [°C] (Dickson and Fanelli, 2013)

	Muffler & Cataldi (1978)	Hochstein (1990)	Benderitter & Cormy (1990)	Nicholson (1993)	Axelsson & Gunmlaugsson (2000)
Low enthalpy	<90	<125	<100	≤150	≤190
Intermediate enthalpy	90-150	125-225	100-200	-	-
High enthalpy	>150	>200	>200	>150	>190

There is a combination of geological conditions that could result in a variety of geothermal systems, such that earth heat can be divided into low-enthalpy and high-enthalpy and sometimes intermediate enthalpy appearances. Based on Clauser (2006),"…the origin of the geothermal resource is of no importance at all to its use; It is where the heat is stored which defines how it can be mined and used". Four types of geothermal resources are usually distinguished based on this idea (Clauser, 2006):

- **Hydrothermal:** Hot water or steam at moderate to deep depths with temperatures of up to 350 [°C] in a permeable reservoir of porous rock with active free or forced convection systems.
- **Geo-pressured:** Hot high-pressure reservoir brines containing dissolved natural gas (methane).
- **Hot Dry Rock (HDR):** Systems where fluids are not produced spontaneously. Therefore these systems require stimulation before energy can be extracted. They may occur within or at the margins of active hydrothermal reservoirs, or may be associated only with an elevated heat flow in a conduction dominated geologic setting.
- **Magma:** Molten rock at temperatures of 700 - 1200 [°C] at accessible depth (about < 7 [km]). A geothermal system in which the dominant source of heat is a large reservoir of igneous magma within an intrusive chamber or lava pool is called a magma geothermal reservoir (Gupta and Roy, 2006).

The focus of this thesis is on deep low-enthalpy hydrothermal systems.

1.2 Low-enthalpy hydrothermal systems

A low-enthalpy hydrothermal resource is a kind of geothermal energy resource that has a temperature range of less than 100 [^{o}C], located at a depth of around 150-3000 [m]. The reservoir constitutes porous rocks containing fluid.

One of the well-known applications of these resources is space heating. Hydrothermal heating systems consist of one or several boreholes, which can be deep or shallow. They are utilized to inject and produce geothermal fluid from and into a hydrothermal reservoir. Shallow hydrothermal systems, which are located at a depth of around 150 [m], are referred to as aquifer thermal energy storage, ATES. Deep hydrothermal systems, which are located at a depth of 1-3 [km], are referred to as hydrothermal heating plants (Clauser, 2006).

1.2.1 Low-enthalpy hydrothermal reservoir

The characteristics of deep low-enthalpy hydrothermal sources vary widely, but three components are essential:

- a subsurface heat source (mainly important for deep systems);
- pores and/or fractures in the formation rocks that allow the heated fluid to flow from the heat source to the surface;
- fluid to transport the heat.

The amount of heat being generated by the earth is one of the key factors that determines the temperature gradient at any location. The other two major factors are the thermal conductivity and heat capacity of the rocks, which control how well the rocks can transfer and trap the generated heat. An insulating layer of impermeable rock over the heat source traps that heat and creates a high thermal gradient. Some rocks make better insulators than others, but, in general, fine grained sedimentary rocks such as shale and clay are better insulators than sandstones. The highest thermal gradients are therefore found in regions with both high heat flow and heat capacity insulated by a cap rock with low thermal conductivity.

Transport of hot fluid is also very important and depends on rock permeability and porosity. Rocks such as sandstone are relatively high in porosity and permeability. Limestone is also considered a good medium for the transfer of geothermal fluid, although normally it has low porosity, but due to some geological processes the created fractures makes it high in permeability.

In hydrothermal heating systems, convection is the main phenomenon responsible for the production of large volumes of hot fluid. Therefore, the most critical properties which affect thermal convection and consequently hot fluid production are hydraulic conductivity, permeability, porosity, thickness, transmissivity (the product of reservoir thickness and hydraulic conductivity).

Most of the hydrothermal heating systems are placed in sedimentary rocks often in a sedimentary basin, such as the Pannonian and Paris basins or the Rhine Graben in Europe, with temperature ranging from about 60 [°C] to 100 [°C] (Clauser, 2006).

In the Netherlands, aquifers of sufficient thickness, permeability and temperature for extraction of low-enthalpy hydrothermal energy are mainly located in the northern and western parts. The potential is higher in lower Cretaceous and Triassic sandstones which are located between 1 and 3 [km] depth (Wong et al., 2007).

1.2.2 Hydrothermal heating plants

A hydrothermal heating plant consists of one or several deep well boreholes for producing and injecting geothermal fluid from and into the hydrothermal reservoir. Although there are various configurations for hydrothermal heating plants, the common point is that hot geothermal fluid (water or brine) is extracted from the reservoir, cooled down by extracting heat from it at the surface and injected back into the reservoir. This closed cycle helps to conserve the mass balance and thus avoids geotechnical problems, such as ground surface subsidence. Moreover, this cycle is important for the environment, particularly when highly mineralized geothermal fluids cannot be disposed of above the surface (Kaltschmitt et al., 2007).

Heat production and transportation in a hydrothermal plant are controlled at a surface unit. In this unit, heat is extracted from the produced hot water or brine in a heat exchanger and fed into a secondary distribution circuit. In some cases, a heat pump is also switched into the secondary circuit at an appropriate position to increase the temperature. Due to this geothermal circuit, the produced hot fluid is continuously replaced by a cooled injected water. This leads to an increasing volume of thermal drawdown propagating from the injection to the production well. After the thermal breakthrough time, the temperature of the produced fluid will decrease at a rate depending on the production rate, the distance between the boreholes, as well as on the physical and geometrical properties of the reservoir.

A sufficient minimum offset between the two well bottoms prevents a reduced lifetime, which is commonly 20 to 30 years for low-enthalpy deep hydrothermal systems. The offset is of the order of 1000 [m] to 2000 [m]. Frequently, the two wellheads are equally offset. However, sometimes it may be attractive or even necessary to drill both boreholes from the same platform and deviate one or both of them. Figure 1-1 shows a schematic picture of a hydrothermal heating plant. A common range of depths and well offsets has been shown on this figure.

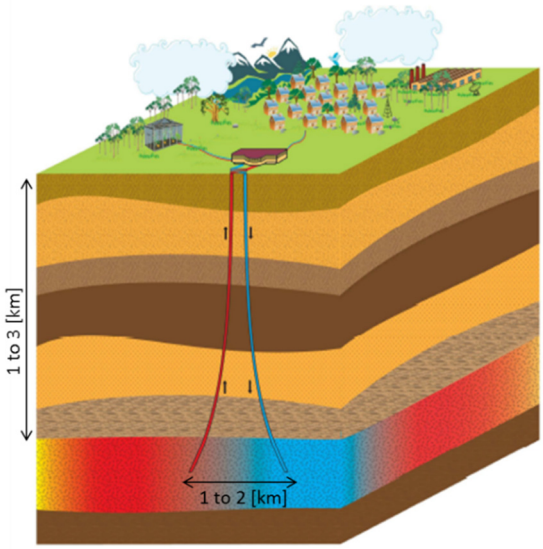

Figure 1-1. Schematic picture of a hydrothermal heating plant

Recently, in the Netherlands, a low-enthalpy geothermal heating project was initiated at Delft University of Technology by the name of DAP (Delft Aardwarmte Project). This is a consortium of governmental and industrial partners that aims to develop an innovative geothermal system at the campus of Delft University of Technology (Salimi et al., 2011). In this project, geothermal wellbores target the Delft Sandstone Member, a fluvial sandstone formation located at depths ranging from 1.7 to 2.3 [km] below the surface. In order to drill wellbores, a new light weight composite tubing is proposed. The tubing of the injection and production wells also contains a thermoplastic inner wall, which is expected to be less corrosive and less expensive, when

compared to regular steel tubing (Wolf et al., 2008). The project will be utilized for heating offices and student houses on the campus.

1.3 An overview of current numerical-experimental studies

In the literature, an enormous number of experimental and numerical studies have been presented. Here, an overview of the most important experimental and numerical studies, which are relevant to the work involved in this thesis, is given.

1.3.1 Current experimental studies

During fluid flow in a geothermal reservoir, the hydrothermal properties including density, viscosity, thermal conductivity, heat capacity, thermal dispersion, and hydraulic conductivity vary with temperature variation. The variation of some of these parameters are more important than others and affect the heat transfer mechanism more. Among those viscosity, density, thermal dispersion, and hydraulic conductivity can be named.

Injection of a fluid with a certain temperature in shallow geothermal systems inevitably changes the reservoir temperature. This change affects the fluid density, viscosity and consequently reservoir hydraulic conductivity, which is an important property affecting the system performance. Therefore it is important to study the significance of these effects and their influence on the reservoir lifetime.

The dependency of density and viscosity on temperature (and also concentration) is an interesting macroscopic physical phenomenon and extensively discussed by Kolditz et al. (2002), Elbashbeshy and Bazid (2000), and Adams and Bachu (2002) among others. This dependency, however, is often ignored in studying heat flow and transport problems in low-enthalpy geothermal systems (Simmons, 2005). There are inconsistent ideas about the importance of the effect of these dependencies on the heat flow process, as in Simmons (2005) and Fossoul et al. (2011). Fossoul et al. (2011), by comparing two modeling scenarios, a model with constant fluid properties and one with variable density and viscosity, showed that these effects can be neglected in analyzing heat flow in shallow low-enthalpy geothermal systems. However, Simmons (2005) numerically showed that this dependency is important and should be considered.

Thermal dispersion mainly occurs due to variations in fluid flow paths and velocity in pore spaces in heterogeneous domains (Molina-Giraldo et al., 2011). Thermal convection and conduction interactively give rise to thermal dispersion along the flow direction (longitudinal dispersion) as well as perpendicular to the flow direction (transversal dispersion). Despite the uncertainty and contradiction in defining and quantifying the causes of thermal dispersion, several empirical formulae based of experimental works have been proposed. They mostly quantify the thermal dispersion coefficient in terms of Darcy fluid velocity. For example, Sauty et al. (1982), Lu et. al. (2009), and Rau et al. (2012) among others. Sauty, et al. (1982) described the thermal dispersion as a linear function of velocity. However, Rau et al. (2012) recently suggested a dispersion model as a function of the square of the thermal front velocity. The magnitude of thermal dispersivity is another issue of disagreement. Smith and Chapman (1983) assert that thermal dispersion has the same order of magnitude as solute dispersivities, while Ingebritsen and Sanford (1999) totally ignore it. Vandenbohede et al. (2009) suggested that thermal dispersivities are less scale-dependent and small in comparison to solute dispersivity values.

1.3.2 Current numerical modeling

Numerical modeling is a fundamental instrument for the elaboration and assessment of a strategic utilization of geothermal energy. Simulation can be very important in order to define and progressively modify the management strategy of the geothermal field (Franco and Vaccaro 2014). The accuracy of a numerical simulation of a hydrothermal system depends on two factors: model accuracy and physical properties accuracy. If either of these two factors is not accurate, the simulation results will be dubious and the design will be unreliable.

Model accuracy can be controlled by several means; among them is the comparison with analytical solutions and history data. Analytical solutions, usually, can be easily utilized to verify relatively simple 1D models and, in some cases, 2D models. However for a complex non-linear 3D system, analytical solutions are not valid. In such cases, using history data and history matching will be the best (but not an easy) option for model validation. On the other hand, construction of the numerical model must be supported by a detailed and accurate knowledge of the physical properties of the system; including proper geological and geometrical characteristics of the reservoir, accurate initial hydrothermal properties of the reservoir and proper information about the production scenarios.

Complexity in numerical modeling for a geothermal systems arises from two issues: geometry and heat convection. Large geometries can be discretized with large elements as long as the convection is not dominant. Highly convective phenomena require fine element (grids) to obtain proper accuracy. This creates expensive computational calculations. These calculations become even more complicated when wellbores are added to the system. The slenderness of the wellbores requires a large amount of elements, consequently making the CPU time unrealistic for engineering practice. The governing equations in such cases have a relatively high Peclet number that makes them behave like hyperbolic functions, which require fine meshes (grids) and proper upwind schemes. This kind of numerical constraint exerts a considerable limitation on the applicability of current numerical tools. For practical purposes, they are normally utilized to simulate limited regions. However, if a more general simulation is pursued, such as modeling the whole region with wellbores, parallel computing using multiple processor systems is needed.

Currently, several models have been developed to simulate heat flow in geothermal reservoirs and wellbores. Different computational tools are available. They can be divided into two categories: reservoir simulators, and wellbore simulators. TOUGH and its derivatives (Battistelli et al., 1997 and Kiryukhin, 1996), Eclipse (Brouwer et al., 2005), and FEFLOW (Blocher et al., 2010), among others, have been widely utilized for geothermal reservoir simulation. On the other hand, HOLA (Bjornsson and Bodvarsson, 1987 and Kiryukhin and Yampolsky, 2004), and WELLSIM (Gunn and Freeston, 1991 and Gunn et al., 1992), among others, are widely utilized as wellbore simulators. Most of the existing wellbore simulators are capable of solving mass and energy conservation equations for geothermal fluid flow in wellbores. Reservoir and wellbore simulators have been coupled to simulate integrated reservoir-wellbore geothermal systems. Hadgu and Zimmerman (1995) coupled the wellbore simulator WFSA and the reservoir simulator TOUGH to model geothermal brine in wells and reservoirs. Bhat et al. (2005) utilized HOLA and TOUGH2 to couple wellbores and reservoir heat and fluid flow. Recently, Gudmundsdottir et al. (2012) designed a 1D steady-state wellbore model, FloWell, which will be, according to the authors, coupled to the reservoir model TOUGH2.

1.4 Thesis objectives and work

The main objectives of this thesis are:

- To investigate the variation of the formation fluid density and viscosity with temperature, typically existing in hydrothermal conditions.
- To investigate thermal dispersion due to heat flow in a porous domain.
- To establish a discretization technique that covers all important features of the hydrothermal system geometry and physical processes, and, at the same time, is computationally efficient such that it can be run on a normal PC (500 MHz, 4GB RAM).
- Formulating a prototype model for a preliminary estimation of the reservoir lifetime by knowing its porosity and initial temperature for different design parameters, namely, discharge, well spacing and injection temperature.

To achieve these objectives, extensive experimental-numerical work has been conducted. Chapters 3 and 4 give a detailed description of the experimental work and Chapter 5 gives a detailed description of the numerical work. Here an overview is given.

1.4.1 Experimental study

To obtain a highly productive low-enthalpy geothermal system, the chosen reservoir should maintain a desired temperature range and a sufficient flow rate with minimum heat loss to adjacent formations. Design of such a system requires a deep understanding of heat and mass transfer inside the wellbores and the geothermal reservoir, plus proper knowledge of the reservoir geometrical and hydrothermal properties and their effects on heat transport and production, and hence on the system lifetime.

To study the hydrothermal fluid properties and their effect and significance on a system's lifetime, an experimental set-up has been designed. The set-up consists of a plexiglas box filled with three layers of clay, sand, and clay saturated with de-aired water. In this set-up, heat flow in a fully saturated porous domain was studied. The effects of fluid density, viscosity and thermal dispersion on the breakthrough curves under low-enthalpy geothermal conditions were examined. For a better understanding of these parameters, a series of experiments has been conducted for hot or cold injection, different discharge rates and different transport directions (horizontal, vertical-upward, vertical-downward). The objectives of these experiments are:

- To inspect the density and viscosity and hence hydraulic conductivity effect of heat transport under low-enthalpy geothermal conditions.
- To validate and fine tune the numerical tool.
- To study the thermal dispersion under experimental conditions.

All experiments are modeled numerically. A series of backcalculation studies comparing the numerical results to the experimental results has been conducted to quantify the magnitude of the thermal dispersion. As a result, a constitutive model describing the thermal dispersion in terms of fluid density, viscosity and pore geometry, taking into consideration different injection scenarios, has been developed.

1.4.2 Numerical study

To study heat transfer in a real scale hydrothermal system, a numerical study has been conducted. The aim was to study heat and mass transfer in hydrothermal low-enthalpy geothermal systems constituting reservoirs, wellbores and surrounding soil formations. Different reservoir geometries and hydrothermal properties have been examined and their effects quantified.

Systems of this kind involve heat conduction and convection occurring in complicated and highly disproportionate geometry. In developing numerical tools for geothermal systems, important efforts are devoted to tackling the discretization of two main issues: geometry and heat convection. Deep geothermal systems consist of very slender wellbores embedded in a vast soil mass. This geometrical peculiarity exerts enormous computational burden, as a combination of very fine elements (cells) and coarse elements (cells) is normally needed to discretize the physical domain. For three-dimensional systems, this normally requires hundreds of thousands to millions of elements, making the CPU time unrealistic for engineering practice. This problem gets even more complicated in the presence of convection and groundwater flow. The governing equations of cases with relatively high Peclet numbers behave like hyperbolic functions, which require fine meshes (grids) and proper upwind schemes.

To tackle this problem, a combination of 1D, 2D and 3D numerical geometries are coupled. The wellbore geometries are modeled using 1D elements, but the physical processes of heat conduction and convection in all involved components and their thermal interactions are taken into consideration in a pseudo 3D modeling technique. The reservoir is modelled as a 3D geometry and the surrounding soil formations as a 2D geometry. The produced numerical model is computationally efficient due to the enormous reduction

in the number of the required finite elements. As a result of the computational efficiency and accuracy, the proposed model provides the means for more insight into heat flow in deep low-enthalpy hydrothermal systems.

1.4.3 A prototype design model

In order to assess the effects of the reservoir conditions on the lifetime of a low-enthalpy geothermal system various parametric analyses have been performed. Special attention has been given to:

- Reservoir characteristics; e.g. porosity, reservoir inclination, geothermal fluid salinity
- Initial temperature of the reservoir
- Injection temperature and periodic injection scenario
- Injection/production discharge rate
- Thermal interaction in wellbores
- Friction in pipelines and pipe materials
- Well spacing at the surface and at the reservoir level

This is to provide criteria for engineers to improve hydrothermal system optimization which requires less investment, better economy and more efficiency.

As a result of this study, a prototype model has been developed that accounts for all studied significant factors affecting the lifetime of hydrothermal systems. The proposed model is formulated based on a numerical example resembling a base case for a low-enthalpy geothermal system. The model predicts, empirically, the lifetime of a hydrothermal system as a function of reservoir porosity, discharge rate, well spacing, average initial temperature of the reservoir, and injection temperature. The integration of these investigations can provide a preliminary estimation of the lifetime of a low-enthalpy hydrothermal system that can be utilized before conducting a detailed analysis.

1.5 Thesis outline

The thesis consist of 7 chapters, starting with the current chapter as the Introduction.

Chapter 2: The objective of this chapter is to calibrate the finite element package COMSOL Multiphysics, which has been used for the numerical modeling in this thesis, by means of analytical solutions. The calibration is

carried out by comparing the analytical solution for heat flow in a porous medium with that of the numerical model in order to qualitatively isolate the numerical dispersion from the physical thermal dispersion.

Chapter 3: In this chapter, heat flow in a fully saturated porous domain subjected to cold and hot injection is experimentally examined. The effects of fluid density and viscosity on the breakthrough curves under low-enthalpy geothermal system conditions are studied. For this, a series of laboratory experiments and finite element analyses were carried out. Special attention was given to the variation of density, viscosity and thermal dispersion under different injection scenarios.

Chapter 4: In this chapter, a backcalculation study comparing the numerical results to the experimental results is conducted to examine the effect of thermal dispersion, and to develop a constitutive model describing thermal dispersion in terms of fluid density, viscosity and pore geometry, taking into consideration different injection scenarios.

Chapter 5: In this chapter, a computationally efficient finite element model for transient heat and fluid flow in a deep low-enthalpy geothermal system is formulated. Emphasis is placed on the coupling between the involved wellbores and the soil mass, represented by a geothermal reservoir and a surrounding soil mass. Two main aspects have contributed to the computational efficiency and accuracy: the wellbore model, and the 1D-2D numerical geometry coupling.

Chapter 6: In this chapter, a prototype design model for low-enthalpy hydrothermal systems is introduced. The model is developed based on the findings presented in the previous chapters and an extensive parametric analysis is carried out based on typical physical and human controlled parameters. The model predicts, empirically, the lifetime of a hydrothermal system as a function of reservoir porosity, discharge rate, well spacing, average initial temperature of the reservoir, and injection temperature. The results of this study can provide geothermal engineers with a preliminary conjecture about the lifetime of a low-enthalpy hydrothermal system.

Chapter 7: In this chapter the conclusions of the thesis are summarized. Recommendations for future research are also included.

Chapter 2

Analytical solution of heat flow in porous media

This chapter addresses one-dimensional analytical solutions for heat flow in porous media. The solutions are made applicable to low enthalpy geothermal systems, where conduction-convection heat flow occurs together with heat loss. The objective of this chapter is to study the significance of heat transfer mechanisms in low-enthalpy geothermal systems and form the basis for the experimental and numerical studies that have been conducted in this research work. The analytical solutions are utilized to calibrate the finite element package COMSOL Multiphysics, which has been used for numerical modeling in this thesis. They are also utilized to highlight the significance of some thermal parameters involved in hydrothermal systems.

This chapter is based on two conference papers, “An extension of Lauwerier’s solution for heat flow in saturated porous media” (Saeid and Barends, 2009) and “Physical aspects of heat transport in porous media” (Barends and Saeid, 2010).

2.1 Introduction

Analytical solutions of physical problems, such as heat conduction-convection in a porous medium domain, are limited and normally utilized to give an

overview of the behavior of a simple geometry subjected to a relatively simple boundary condition. Numerical solutions, on the other hand, are versatile and normally utilized to simulate complicated geometry, processes and boundary conditions. This thesis deals with intricate processes occurring for rather complicated geometry and boundary conditions. It involves solving non-linear heat flow problems occurring in a vast and highly disproportionate geometry. This inevitably necessitates the use of numerical tools to solve the problem. However, the numerical tools are in most cases mesh-dependent, which might give rise to numerical errors unless accurate mesh sizes and time steps are utilized. To understand and quantify these errors, it is useful to compare the numerical results with those obtained from analytical solutions of some applicable geometry and boundary conditions. By this, it is possible to calibrate the numerical tool and design an accurate finite element mesh applicable to the geometry and range of physical processes involved in the study.

Several analytical and semi-analytical solutions based on the Laplace transform and Fourier transform have been introduced in literature. Ogata and Banks (1961), Sauty et al. (1980) and Van Genuchten (1981) provided an analytical solution to advection-diffusion in an insulated medium. Lauwerier (1955) introduced an analytical solution for convective heat transport in a porous medium adjacent to a conductive domain. Barends (2010) extended Lauwerier's solution by including conduction and convection in the porous domain. Heat bleeding (loss/gain) to adjacent layers is also included in the Barends model. Al-Khoury (2012) introduced a semi-analytical solution for transient conductive-convective heat flow in an axial symmetric medium using the Fourier transform. In this chapter, the first three solutions will be highlighted as they are relevant to the thermal transport phenomena occurring in low-enthalpy geothermal systems. In particular, Ogata and Banks' model is utilized for the calibration of the numerical tool, and Barends' model is utilized to study the effects of some of the involved thermal parameters on heat flow in geothermal reservoirs subjected to hydrothermal conditions.

2.2 Analytical solutions of 1D heat transfer equations

In this section, three solutions describing heat flow in three different homogeneous domains are presented: 1) an insulated conductive-convective domain, 2) a convective domain adjacent to a conductive domain, and 3) a conductive-convective domain adjacent to a conductive domain.

These solutions will be applied to an example describing heat flow in a homogeneous porous medium domain of height H and initial temperature T_0, bounded at the top by an impermeable layer with an initial temperature of $T_0'=T_0$ (Figure 2-1 to 2-3). At time t=0, water with a temperature of $T_i < T_0$ is injected from the left boundary at a constant flow rate of v. In this example, the lower boundary of the reservoir is sealed for water and heat, and the upper boundary is sealed for water but it can conduct heat (thermal bleeding). The properties of the porous medium and the impermeable layers are given in Table 2-1.

Table 2-1. Properties of the porous medium and the adjacent layer

Symbol	Value	Unit	Name
ϕ	0.25	[-]	Porosity
ϕ_t	0.05	[-]	Porosity of top layer
K	2.8E-13	[m^2]	Intrinsic permeability
k_t	1E-18	[m^2]	Intrinsic permeability of top layer
ρ_f	1200	[kg/m^3]	Fluid density
ρ_s	2800	[kg/m^3]	Solid density
ρ_t	3000	[kg/m^3]	Top layer density
c_f	4184	[J/m^3K]	Fluid heat capacity
c_s	830	[J/m^3K]	Solid heat capacity
c_t	840	[J/m^3K]	Top layer heat capacity
λ_s	1.7	[W/(m.K)]	Thermal conductivity of rock
λ_f	0.6	[W/(m.K)]	Thermal conductivity of fluid
λ_t	2.6	[W/(m.K)]	Thermal conductivity of top layer
H	15	[m]	Porous medium height
T_0	80	[^oC]	Initial temperature
T_i	30	[^oC]	Injected temperature
T_t	80	[^oC]	Initial temperature of top layer
V	1E-6	[m/s]	Velocity

2.2.1 Insulated domain

Heat conduction-convection flow in an insulated homogeneous isotropic 1D domain (Figure 2-1-left) can be described as

$$\frac{\partial T}{\partial t} + v\frac{\partial T}{\partial x} - D\frac{\partial^2 T}{\partial x^2} = 0 \qquad (2.1)$$

in which, T is the temperature [°C], D is the thermal diffusivity [m^2/s] and v is the velocity [m/s], expressed, for a two-phase domain constituting a solid phase s and a fluid phase f, as

$$D = \frac{\lambda}{\rho c} \quad , \quad \lambda = \phi\lambda_f + (1-\phi)\lambda_s$$
$$v = \frac{\rho_f c_f}{\rho c} q \ , \quad \rho c = \phi\rho_f c_f + (1-\phi)\rho_s c_s \tag{2.2}$$

where ϕ is the porosity, ρ [kg/m^3] is the mass density, c [J/kg.K] is the specific heat capacity, λ [W/m.K] is the thermal conductivity tensor, and q [m/s] is the Darcy velocity.

The analytical solution of this equation has been derived by, among others, Ogata and Banks (1961). They provided a general solution to the advection-diffusion of mass in an insulated homogeneous porous medium. In terms of heat transport, for a Dirichlet boundary condition and a constant initial condition:

$$T = T_0 \ \rightarrow \qquad t = 0 \quad , \quad x \geq 0$$
$$T = T_i \ \rightarrow \qquad t > 0 \quad , \quad x = 0 \ \ (\text{at the injection}) \tag{2.3}$$

their solution can be expressed as

$$T = \frac{T_i}{2}\left[\operatorname{erfc}\left(\frac{x - vt}{2\sqrt{Dt}}\right) + \exp\left(\frac{vx}{D}\right)\operatorname{erfc}\left(\frac{x + vt}{2\sqrt{Dt}}\right)\right] \tag{2.4}$$

where T_i and T_0 are the injected and initial temperatures. Figure 2-1-left shows a schematic figure of Ogata and Banks domain and assumption where only heat convection and conduction inside the reservoir are considered. Figure 2-1-right shows the analytical temperature distribution along the length of the reservoir after around 1.5 years for two different cases. Case A describes heat flow due to convection only, where $D \rightarrow 0$. In this case the thermal front is rather sharp. Case B describes heat flow due to convection-conduction, where the thermal front is somewhat diffuse. Hence, the difference between Cases A and B is due to conduction in this example.

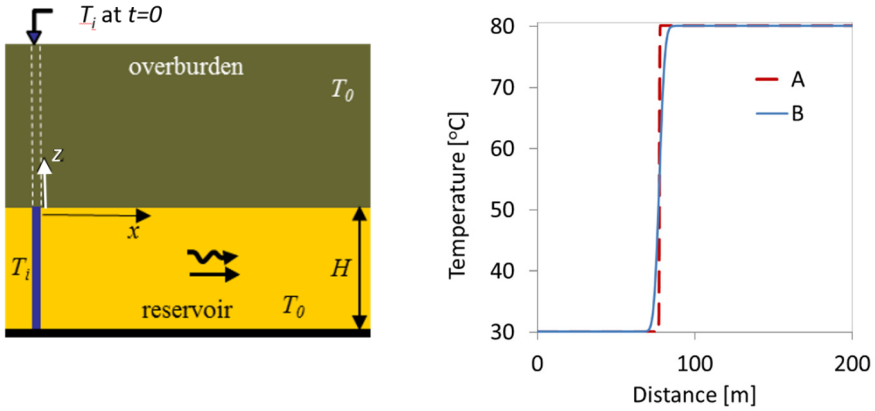

Figure 2-1. Left; schematic description of Ogata and Banks (1961) problem; Right: comparing pure convection (A) and convection-conduction (B) phenomena.

2.2.2 Convective domain adjacent to a conductive domain

Lauwerier (1955) solved Eq.(2.1) for heat flow in a predominantly convective porous domain attached to a conductive layer. Figure 2-2-left shows a schematic representation of Lauwerier's domain, where the convective domain represents a porous reservoir and the adjacent layer represents an impermeable overburden. Heat flow in such a system can be described as

$$\begin{aligned} &\frac{\partial T}{\partial t} + v\frac{\partial T}{\partial x} = 0 && x \geq 0\ ,\ t \geq 0 \\ &\frac{\partial T'}{\partial t} - D'\frac{\partial^2 T'}{\partial z^2} = 0 && z \geq 0\ ,\ t \geq 0 \end{aligned} \qquad (2.5)$$

in which T and T' represent the temperature in the reservoir and the adjacent overburden layer. The initial and boundary conditions are:

$$\begin{aligned} &T = T' = T_0 && t = 0,\ x \geq 0\ ,\ z \geq 0 \\ &T = T_i && t > 0,\ x = 0\ (\text{at the injection}) \\ &T = T' && z = 0\ \ (\text{at the interface}) \\ &\frac{d^2 T'}{dz^2} = 0 && t > 0,\ z = 0 \end{aligned} \qquad (2.6)$$

The solution of these coupled equations is:

$$T = T_0 \operatorname{erfc}\left[\frac{\xi}{2\sqrt{\theta(\tau-\xi)}}\right] - U(\tau-\xi) \tag{2.7}$$

in which

$$\xi = \frac{x\lambda'}{h^2\rho_f c_f q} \quad , \quad \tau = \frac{\lambda' t}{h^2 \rho c} \quad , \quad \theta = \frac{\rho c}{\rho_f c_f}$$
$$U(\xi) = \begin{cases} 0 & \tau-\xi<0 \\ 1 & \tau-\xi>0 \end{cases} \tag{2.8}$$

The essential assumptions of Lauwerier (1955) are: 1) the temperature variation in the reservoir is only horizontal, assuming a uniform heat flow over the height, and 2) the conduction heat flow in the reservoir is negligible. Figure 2-2-right compares three cases: A, B and C. Cases A and B are identical to those given in section 2.2.1. Case C describes heat flow in the reservoir, where convection is the only mechanisim of heat transfer in the reservoir with heat gain/loss to the adjacent layer. The difference between Cases A and C is due to heat conduction to the adjacent layer, known as bleeding.

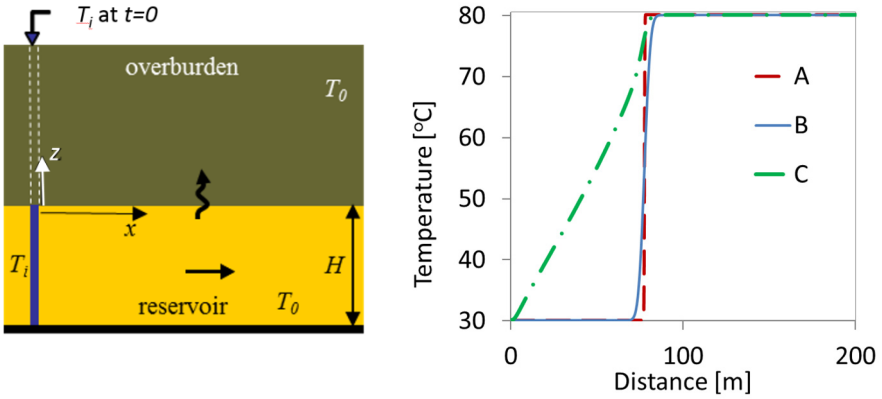

Figure 2-2. Left: schematic description of Lauwerier's (1955) problem; Right: comparing pure convection (A) and convection-conduction (B) and convection-bleeding (C) phenomena.

2.2.3 Conductive-convective domain adjacent to a conductive domain

Barends (2010) extended Lauwerier's solution to account for conduction-convection in the reservoir and conduction in the adjacent layer. Figure 2-3-

left shows a schematic representation of Barends' domain. Heat flow in such a system can be described as

$$\frac{\partial T}{\partial t}+v\frac{\partial T}{\partial x}-D\frac{\partial^2 T}{\partial x^2}=0$$
$$\frac{\partial T'}{\partial t}-D'\frac{\partial^2 T'}{\partial z^2}=0 \qquad (2.9)$$

The initial and boundary conditions are the same as those in Eq.(2.6). Barends solved this problem using the Laplace transform, as

$$T-T_0=\frac{2(T_1-T_0)}{\sqrt{\pi}}e^{\frac{xv}{2D}}\int_{\frac{x}{2\sqrt{Dt}}}^{\infty}e^{-\delta^2-(\frac{xv}{4D\delta})^2}\operatorname{erfc}[(\frac{x^2h'\sqrt{D'}}{8DH\delta^2}+\frac{z}{2\sqrt{D'}})(t-\frac{x^2}{4D\delta^2})^{-0.5}]d\delta \qquad (2.10)$$

where T_0 is the initial temperature, and

$$D'=\frac{\lambda'}{\rho'c'},\quad \delta=\frac{DD'h'}{(vH)^2},\quad h'=\frac{\rho'c'}{\rho c} \qquad (2.11)$$

where D' [m^2/s] is the thermal diffusivity in the adjacent layer and δ is the Lauwerier extension parameter (Barends, 2010).

Figure 2-3-right compares pure convection (case A), convection-conduction (case B), convection-bleeding (case C), and convection-conduction-bleeding (case D). Cases A, B and C are those given by Ogata and Banks (1961) and Lauwerier (1955). Case D describes the solution given by Barends (2010). The difference between Cases B and D describes the magnitude of bleeding in this example. The small difference between Cases C and D highlights the thermal conduction effect inside the reservoir.

Eq.(2.10) can also be utilized for cases exhibiting thermal dispersion. This can be done simply by replacing D by

$$D=\frac{\lambda}{\rho c}+D_{dis} \qquad (2.12)$$

where D_{dis} represents the thermal dispersion. A detailed explanation of thermal dispersion is given in chapter 4, section 4.2.1.4.

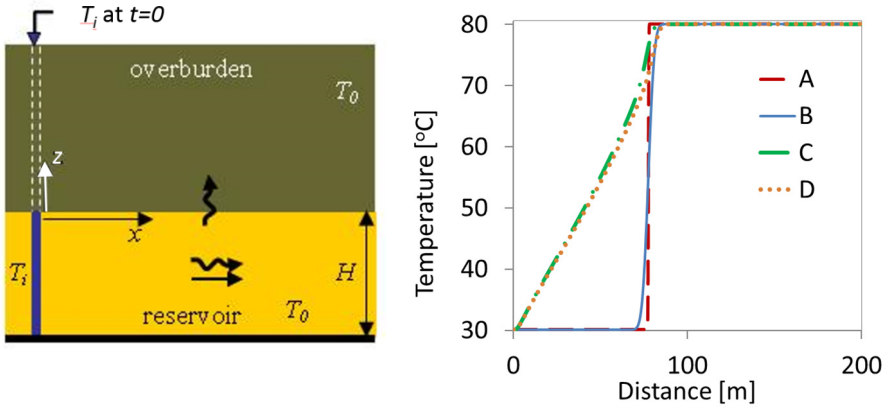

Figure 2-3. Left: schematic description of Barends' (2010) problem; Right: comparing pure convection (A), convection-conduction (B) , convection-bleeding (C), and convection-conduction bleeding(D) phenomena.

Thermal bleeding from a geothermal reservoir to its adjacent layers is an important issue in the design of a hydrothermal system. Thermal bleeding refers to the amount of heat that leaks to or from an adjacent layer which transfers heat via conduction. It is utilized to identify the significance of heat loss/gain from a geothermal reservoir to/from its neighboring layers. Barends (2010) introduced the bleeding number relating heat loss/gain to the thickness of the reservoir, flow velocity, heat capacity ratio between the resrvoir and the adjacent layer, thermal diffusivity of the adjacent layer and the convective length, as

$$Bl = \frac{2h'L}{\sqrt{\pi}H}\sqrt{\frac{D'}{vL}} \qquad (2.13)$$

in which *h'* is the heat capacity ratio, defined as $(\rho c)'/\rho c$, *L* is the characteristic length of the reservoir, *H* is the thickness of the reservoir, *D'* is the thermal diffusivity of the overburden and *v* is the velocity.

To study the effect of the thermal diffusivity of the adjacent layer on the bleeding number, a couple of scenarios have been assumed. In these scenarios, different ratios of *D'/D* have been considered. Each scenario has been modeled numerically for two different velocities, v_0 and $10\ v_0$, to identify the effect of fluid velosity on the thermal bleeding.

Figure 2-4, shows the effect of the bleeding number "*Bl*" with respect to the variation of *D'/D*. As the thermal diffusivity of the adjacent layer increases, the

bleeding number increases and more heat transfers between the reservoir and the overburden layer. Comparing Figure 2-4, right and left, shows that as the velocity increases, the bleeding effect decreases. The dominance of convection in the reservoir makes the conduction and the bleeding effects less important.

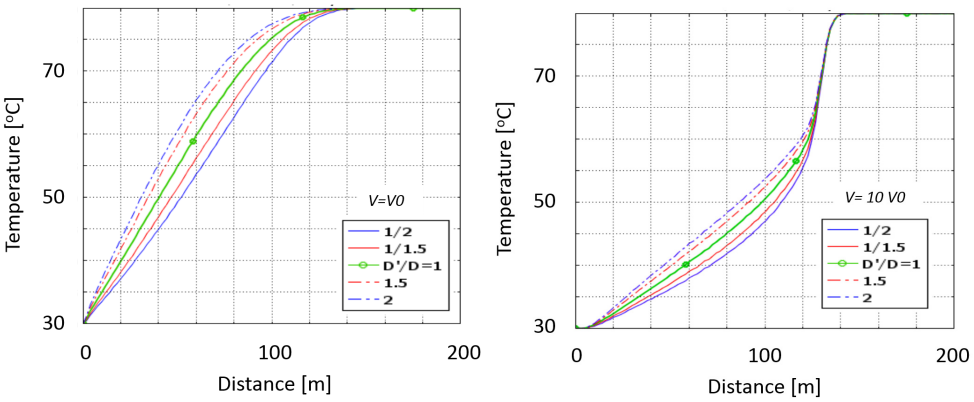

Figure 2-4. Bleeding effect with respect to the variation of *D'/D*, for small and large velocities

2.3 Calibrating the numerical tool

This thesis involves solving a non-linear heat flow problem occurring in a larg and highly disproportionate geometry. This inevitably necessitates the use of numerical tools to solve the problem. However, the numerical solution to such a problem can be mesh-dependent, necessitating the design of accurate mesh sizes and time steps. To design an accurate finite element mesh applicable to the geometry and the range of physical processes involved in the study, the numerical tool needs to be calibrated against analytical solutions for some applicable geometry and boundary conditions.

The finite element package, COMSOL Multiphysics, has been utilized in this thesis for the numerical calculations. It has been calibrated and fine-tuned based on a comparison between its numerical results and the analytical solution given by Ogatta and Banks (1961) for heat flow in a one-dimensional homogeneous porous medium Eq.(2.4)). The example explained in section 2.2 has been used for the calibration purpose.

Two parameters have been examined: mesh size and time step size. The criterion is to obtain a numerical result that exhibits no numerical dispersion.

In COMSOL the time step size is determined automatically, depending on the element size and the type of analysis. The user can specify a relative and absolute tolerance, indicating the convergence error. Therefore, the element size and relative and absolute tolerance have here been varied in order to get the best match with the analytical solution.

A step-by-step reduction is applied to the element size and "absolute tolerance", a measure of error used in COMSOL for testing convergence (COMSOL, 2011), until the numerical results perfectly match the analytical results. Table 2-2 shows four combinations of element sizes and absolute tolerance. Figure 2-5 compares the computed results of these four cases against the analytical solution. It can be readily seen that Case IV, with the finest element size and tolerance gave the best match.

Table 2-2. Calibration parameters

Numerical solution	**I**	**II**	**III**	**IV**
Element size [m]	15	10	5	1
Absolute tolerance [-]	1E-3	1E-4	1E-5	1E-6

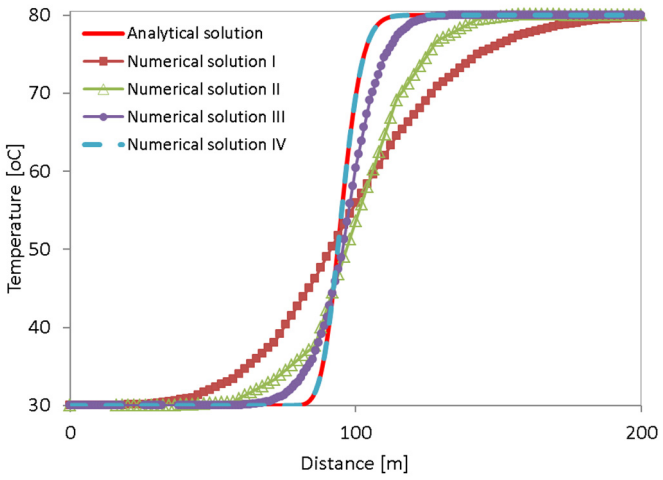

Figure 2-5. Comparison between analytical and numerical solutions

Following this, in this thesis, the absolute tolerance is made 1E-6. The element size of 1 [m] is made as a reference to design the mesh sizes of this example.

However, for the up-scaled domain that will be treated in the forthcoming chapters, depending on the problem and geometry, the element size is chosen based on a proper mesh analysis. The Peclet number is utilized as a criterion for this purpose.

In convective-dominant problems, the element Peclet number must be accurate in order not have spurious oscillations. The Peclet number is a dimensionless number relating the fluid velocity and the element size to the thermal properties. It is defined as the ratio of thermal energy convected by the fluid to the thermal energy conducted within the fluid:

$$\mathrm{Pe} = \frac{vL}{D} = \frac{vL}{\lambda/\rho c} \tag{2.14}$$

where D is the thermal diffusivity of the medium, v is the velocity, L is the characteristic length of the element, ρ the density, and c the heat capacity.

To study this parameter, a parametric analysis is conducted for different Peclet numbers. The example given in section 2.2 has been modeled as a 2D domain in COMSOL. The different scenarios given in Table 2-3 have been studied. The velocity and hence the Pe number of each scenario is 10 times higher than its previous scenario.

Table 2-3. Different scenarios explaining different Pe numbers

Scenario	**I**	**II**	**III**	**IV**	**V**
v	0.1 v_0	v_0	10 v_0	100 v_0	1000 v_0
Pe	0.1 Pe_0	Pe_0	10 Pe_0	100 Pe_0	1000 Pe_0

Figure 2-6 shows the temperature distribution along the middle line of the reservoir at about half the lifetime of each scenario. This figure shows that, as the Peclet number decreases, the heat front becomes diffusive. In contrast, as the Peclet number increases, the heat front becomes sharp. With the increase of the Peclet number, the occurrence of numerical oscillations is more likely, as indicated for Case V in Figure 2-6 . In this case, small time steps and small grid sizes are needed to avoid this.

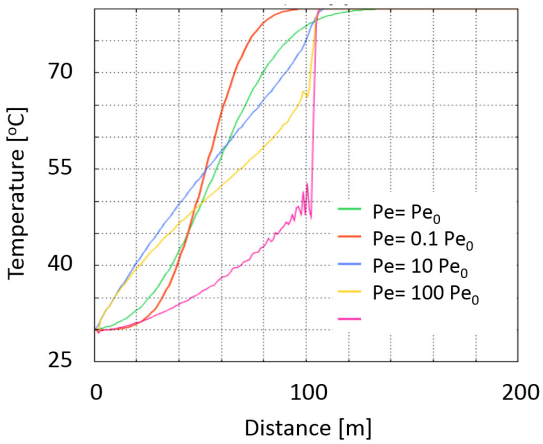

Figure 2-6. Temperature profile along the middle line of the reservoir for different Peclet numbers.

2.4 Parametric analysis

The analytical solutions are particularly useful for studying the significance of the involved parameters in determining the behaviour of the model under specific initial and boundary conditions. In this section, the significance of some of the reservoir hydrothermal parameters on heat flow inside the reservoir has been studied. Eq. (2.10) is utilised for this purpose.

The effects of the injected fluid velocity, *v*; thermal diffusivity of the reservoir, *D*; thermal diffusivity of the overburden, *D'*; and thickness of the reservoir, *H*, are studied. To signify the effects of these parameters, their values have been varied by a factor of 1, 2, 5 and 10. Note that some of the values may not be realistic, but their effects have been shown to demonstrate the total trend of variations. Figure 2-7 shows the results of these calculations. The example given in section 2.2 is utilized as the base case. It has been shown by $1v_0$, $1\ H_0$, $1D'_0$, and $1D_0$ in following figure (Figure 2-7).

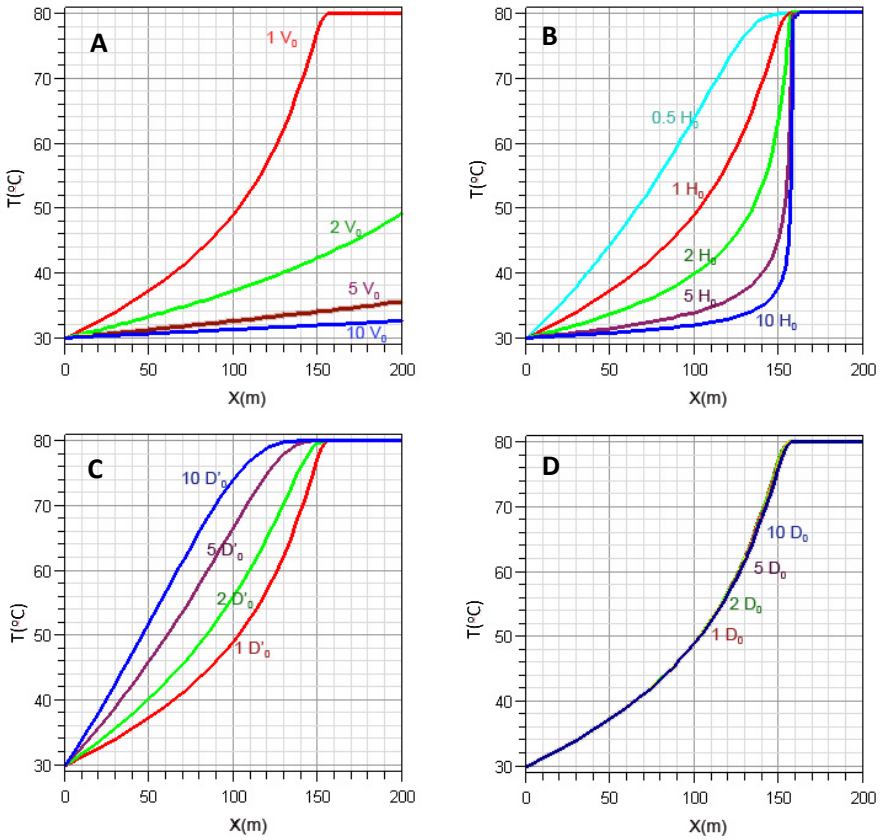

Figure 2-7. Thermal front dependency on v,H,D',D. A: v/v_0=1, 2, 5, 10; v_0=1E-7[m/s] , B: H/H_0=0.5, 1, 2, 5, 10; H_0=15 m , C: D'/D'_0=1, 2, 5, 10; D'_0= 8.9E-7 , D: D/D_0=1, 2, 5, 10, D_0= 8.9E-7

Figure 2-7-A shows the effect of the fluid velocity on the temperature distribution. It shows that at a specific time, under same initial and boundary conditions, geothermal fluid with higher velocity shows less bleeding (heat gain/loss) comparing to the similar fluid with lower velocity. Figure 2-7-B shows that the thickness of the reservoir also has a significant effect on the amount of heat transfer to the adjacent layer. The thicker the reservoir, the less the heat loss/gain.

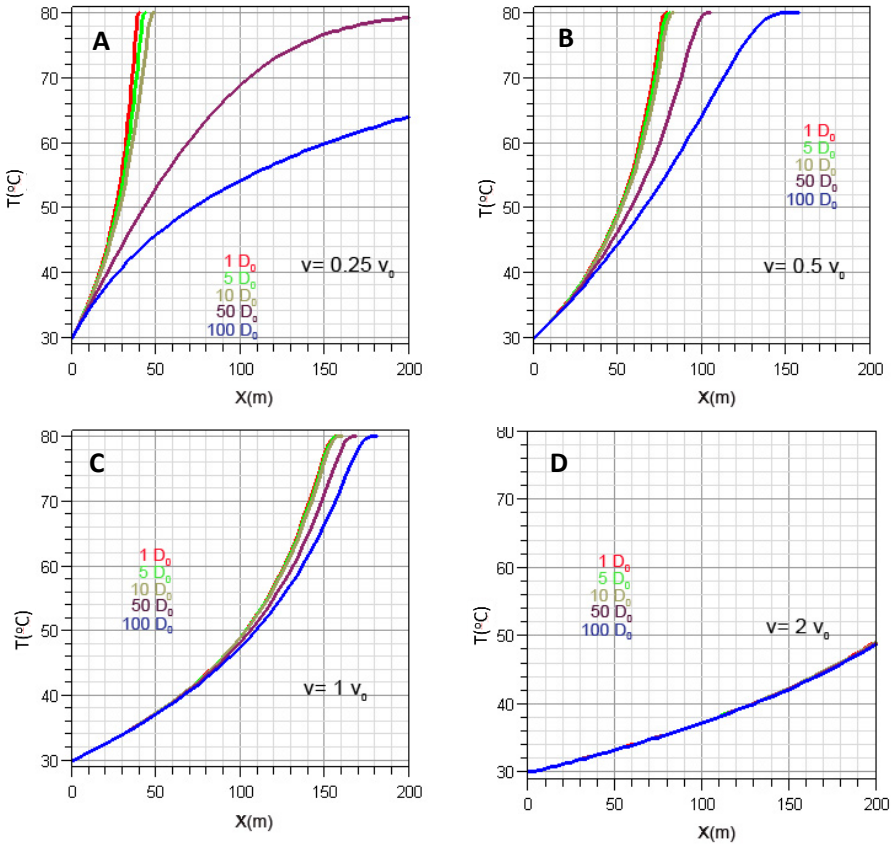

Figure 2-8. Effect of conductivity of the aquifer on heat transport *D/D0*=1, 5, 10, 50, 100. Each graph shows the effect of thermal diffusivity (*D*) on bleeding, for different velocities

Figure 2-7-C shows that the variation of the thermal diffusivity of the adjacent layer has a direct effect on heat gain/loss in the reservoir. As *D'* increases, the tendency for thermal dissipation increases. Therefore for such a case (cold injection), a larger *D'* in the adjacent layer causes more heat to transfer from the adjacent layer to the reservoir, and consequently the reservoir temperature cooling down occurs at a slower pace. In reality, the magnitude of *D'* cannot reach 5 or 10 times D'_0 and therefore its effect would not be very significant. Figure 2-7-D shows that the thermal diffusivity of the reservoir does not play a major role in this example, where the discharge is large. Therefore, the effect of the thermal diffusivity of the reservoir (*D*) was examined for different flow rates. Results are demonstrated in Figure 2-8 A to D. This figure shows that the thermal diffusivity of the reservoir does not play

an important role when the fluid flow rate is high (Figure 2-8 D). It becomes more important when the fluid flow is low or relatively low (Figure 2-8 A, B, C). Comparing Figure 2-8 A to D shows that, when the fluid flow rate is high and the heat transfers by convection rather than conduction, the thermal diffusivity becomes less dominant, and even vanishes.

2.5 Conclusion

In this chapter, the finite element package COMSOL, utilized in this thesis, has been calibrated and fine-tuned based on a comparison between its numerical results and an analytical solution given by Ogata and Banks (1961) for heat flow in a homogeneous porous medium. The calibration is meant to isolate numerical errors that might arise due to an inaccurate choice of the element size, element type or time step. The fine-tuning parameters will be utilized in the rest of this thesis for the numerical modelling of hydrothermal systems.

Additionally, analytical solutions for different combinations of layer characteristics are presented to study the significance of heat loss or gain between the layers. The solutions were made applicable to low enthalpy geothermal systems, where conduction-convection heat flow occurs together with heat loss. The effect of different hydrothermal parameters, of the reservoir and its adjacent layer, on heat transfer inside the reservoir and on the heat loss (bleeding) has been studied in the form of a parametric analysis. The parametric analysis indicates that the thickness of the reservoir and the fluid velocity have the most significant effect on the amount of heat loss/gain to the adjacent layer.

Chapter 3

Experimental study

This chapter illustrates the results of an intensive experimental programme on heat flow in a fully saturated porous domain. Temperature and flow rate ranges comparable to those existing in a typical deep low-enthalpy hydrothermal system are studied. Two main issues are examined: the effect of fluid density and viscosity on heat flow, and the significance and effect of thermal dispersion. Laboratory experiments on a fully saturated sand layer surrounded by two impermeable clay layers, subjected to different flow rates under cold and hot injection scenarios, are conducted.

This chapter is based on the paper “Experimental–numerical study of heat flow in deep low-enthalpy geothermal conditions", published in the Renewable Energy journal (Saeid et al., 2014).

3.1 Introduction

Understanding heat and fluid flow in geological formations is central to a number of disciplines, including renewable energy (Zalba et al., 2003), hydrogeology (Lighty et al., 1990), reservoir engineering (Van Poollen, 1980), geotechnical engineering (Nixon, 1975), and radioactive waste disposal site investigations (Pollock, 1986). Heat transfer in porous media involves two main mechanisms: convection (advection) and conduction (diffusion).

However, due to the inherent heterogeneity of porous media, thermal dispersion can also be an important heat flow mechanism.

During heat flow in a geothermal aquifer, formation fluid density and viscosity vary with temperature variation. With increasing temperature, for instance by hot injection, the fluid viscosity and density decrease (Lide and David, 1990). Injection of a fluid with a certain temperature in shallow geothermal systems (hot and cold injection in aquifer thermal energy storage, ATES) or deep geothermal systems (cold injection in district heating systems) inevitably changes the reservoir temperature. This change affects the reservoir hydraulic conductivity, which is an important property affecting the system performance. It is therefore important to study the significance of these effects and their influence on the reservoir lifetime.

The dependency of density and viscosity on temperature (and also concentration) is an interesting macroscopic physical phenomenon and extensively discussed by Diersch and Kolditz (2002), Elbashbeshy and Bazid (2000), and Adams and Bachu (2002) among others. This dependency, however, is often ignored in studying heat flow and transport problems in low-enthalpy geothermal systems (Simmons, 2005). Fossoul et al, (2011), by comparing two modeling scenarios, a model with constant fluid properties and one with variable density and viscosity, showed that these effects can be neglected in analyzing heat flow in shallow low-enthalpy geothermal systems. However, Simmons (2005) stated that this dependency is important and should be considered. In this chapter special attention is given to the variation of density and viscosity with temperature via laboratory experimental work, and to their effects on low-enthalpy geothermal reservoir lifetime.

3.2 Experimental study

A series of laboratory experimental investigations has been carried out to study the effect of density and viscosity variation on heat flow in a typical porous domain, for a typical temperature range existing in low-enthalpy geothermal systems. Also, thermal dispersion due to fluid flow and heterogeneity of the domain is studied.

3.2.1 Experimental set-up

The experimental set-up consists of a box, 50 [cm] × 15 [cm] × 25 [cm], made of plexiglas sheets, 1 [cm] thick (see Figure 3-1). The thermal properties of the plexiglas are given in Table 3-1. The set-up is composed of three parts: two

buffer zones (inlet and outlet) at the sides of the box and a sample container in between. Two membranes, 33.7 [cm] apart, separate the buffer zones from the sample. The sample consists of a fully saturated sand layer surrounded by two impermeable clay layers.

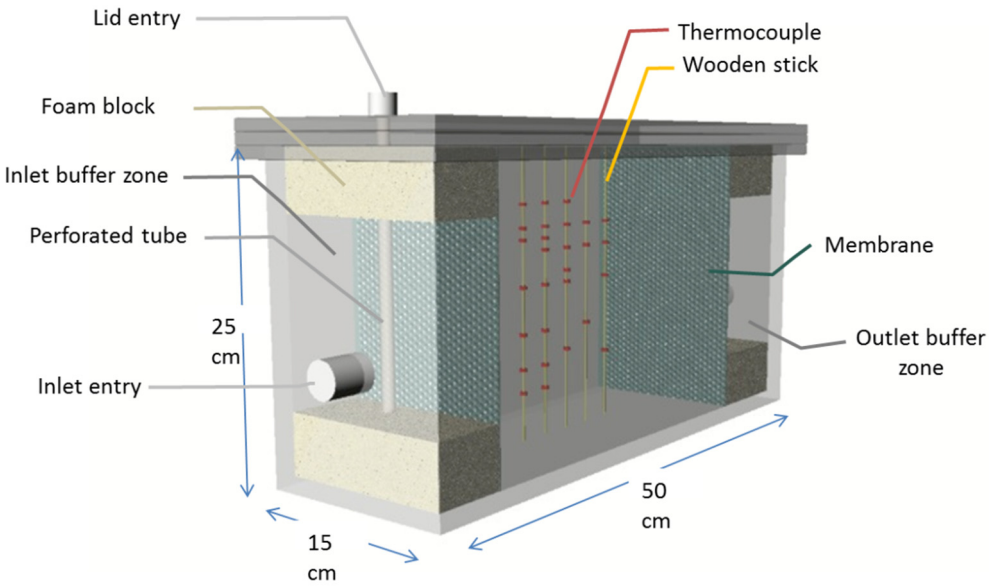

Figure 3-1. Scheme of test box

The test set-up is provided with cold and hot water circuits, consisting of a thermal basin, a pump, and constant-level inflow and outflow tanks (see Figure 3-2). The thermal basin supplies the system with a continuous fixed temperature (T_i), and the pump maintains a constant total head in the inflow tank. The inflow and outflow tanks control the flow rate inside the box by varying the height of the outflow tank. A flow meter, mounted before the inlet entry, and a discharge weight measurement at the outlet were utilized to measure the flow rate. Thirty thermocouples, mounted on 6 wooden sticks, 2 [mm] in diameter, arranged in 6 series, A to F (Figure 3-3 and Figure 3-4) were utilized to measure the temperature distribution in the sand and clay layers (Figure 3-1). The thermocouples were mounted on wooden sticks (a non-conductive material) to eliminate any possible displacement (relocation) during the tests (Figure 3-3). To avoid the likely occurrence of electrical

conductivity between the thermocouples, they were coated by a thin layer of lacquer before placing in the box. Two extra thermocouples were also placed in the inlet and outlet buffer zones to control the injected and output temperatures.

The box was insulated from all sides, except from the top, by hard foam sheets (45 [mm] thick) of low thermal conductivity: 0.026 [W/(m.K)]. The top side, where the box lid is located, was insulated by a thick tissue with low thermal conductivity. Hence, the heat loss in the test set-up can be considered negligible. All tubes carrying water between the thermal basin, the pump, the input tank and the box were insulated, so that heat loss through the pipes was kept small.

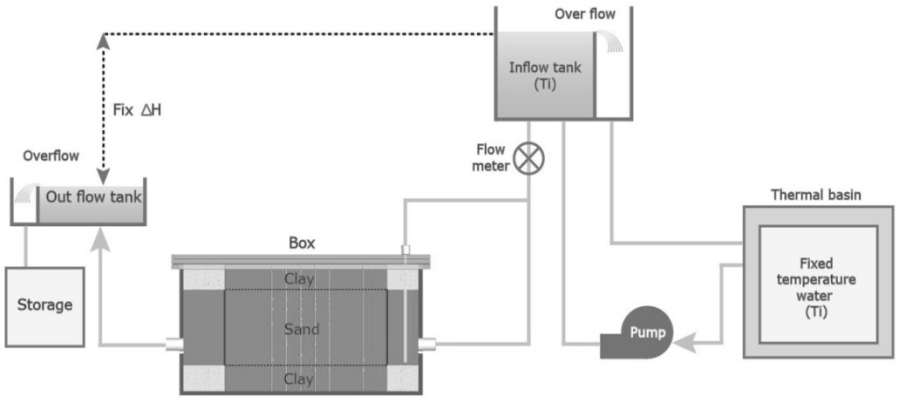

Figure 3-2. Scheme of test set-up

Figure 3-3. A series of thermocouples mounted on a wooden stick

Table 3-1. Material properties

Parameters	Symbol	Dimension	Value
Plexiglass			
Density *	ρ_p	kg/m^3	1190
Thermal conductivity *	λ_p	W/(m.K)	0.21
Heat capacity *	c_p	J/(kg.K)	1500
Baskarp sand			
Density grains **	ρ_s	kg/m^3	2647
D_{10} **		µm	90
D_{50} **		µm	130
D_{90} **		µm	200
Min. porosity **	ϕ_{min}	%	34
Max. porosity **	ϕ_{max}	%	46.9
Hydraulic conductivity	K	m/s	6.5×10^{-5}
Thermal conductivity **	λ_s	W/(m.K)	2.65
Heat capacity *	c_s	J/(kg.K)	830
K147 clay			
Density ***	ρ_t	kg/m^3	1750
Thermal conductivity	λ_t	W/(m.K)	2.0
Heat capacity ***	c_t	J/(kg.K)	2000

* from literature (Lide and David, 1990 (version 2010))

** measured in lab

*** from the provider (SIBELCO)

The sample consists of a Baskarp sand layer, 15 [cm] thick, laid between two Fingering K147, SIBELCO-Germany (mainly kaolinite) clay layers, 5 [cm] thick for each. The sand represents a confined aquifer, and the clay layers represent impermeable cap layers, (Figure 3-5). The physical properties of the sand and the clay are given in Table 3-1, and the chemical components of the clay are given in Table 3-2. The Baskarp sand grain size distribution is shown in Figure 3-6, where it can be seen that the distribution curve is quite steep, indicating that the grain sizes are essentially uniform. Special attention was

made during the preparation of the test set-up for making a homogeneous sand package. The packing method is explained in section 3.2.3.

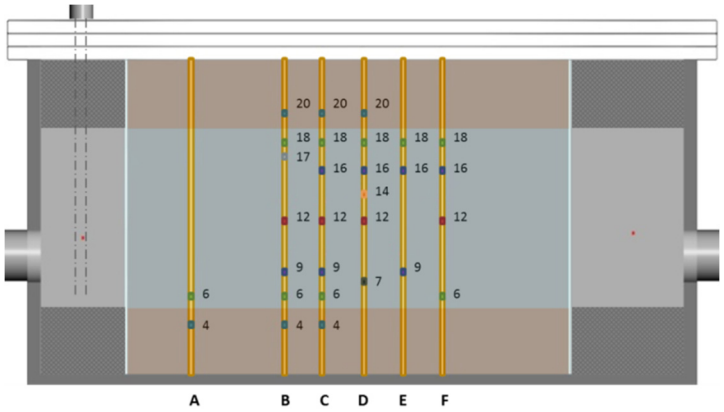

Figure 3-4. Thermocouple locations and labels

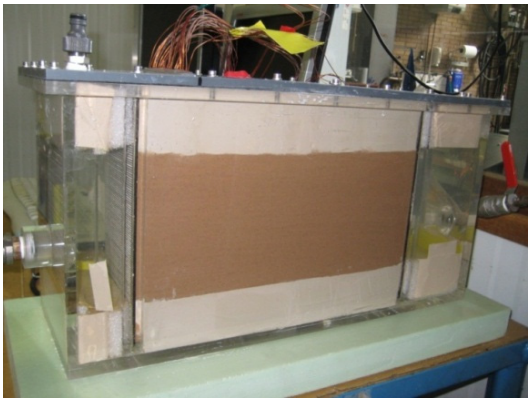

Figure 3-5. Picture of the box after filling sand and clay layers

The hydraulic conductivity and intrinsic permeability of the sand for different porosities were measured by using constant head method in advance at room temperature, and utilized for verification of the measured intrinsic permeability inside the test set-up, Figure 3-7. The measured sand porosity inside the test set-up was 36%, and hence, the intrinsic permeability was 5.2 $\times 10^{-12}$ [m^2].

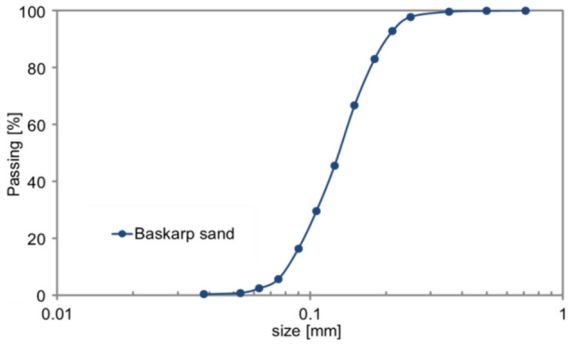

Figure 3-6. Grain size distribution of Baskarp sand

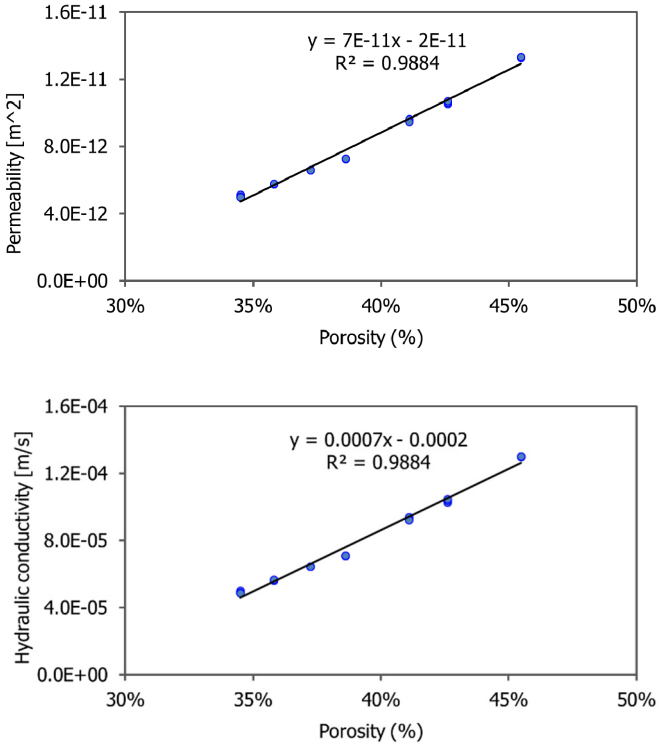

Figure 3-7. Permeability and hydraulic conductivity versus porosity of Baskarp sand

Table 3-2. Chemical components of K147 clay

Sio_2	Tio_2	Al_2O_3	Fe_2O_3	CaO	MgO	K_2O	Na_2O
74.7%	1.10%	15.5%	0.80%	5.50%	0.40%	1.80%	0.20%

3.2.2 Fluid

The box was saturated with fixed temperature (T_0) de-aired water. During the tests, water at a fixed temperature (T_i) is injected into the compacted sand package (T_0). Tests are performed with hot injection into the cold box and then repeated with cold injection into the heated box. To be able to ignore the effect of gravity, vertical tests have also been carried out.

Water properties change with temperature; sometimes significantly and sometimes not. Noting the temperature variation range in these test series (20-70 [^{o}C]), the variation of some water properties with temperature are shown in Table 3-3 and Figure 3-8-A and B, based on literature (Lide and David, 1990 (version 2010)).

Table 3-3. Water thermal properties at 0.1 MPa (1 bar) (Lide and David, 1990)

Temperature (at P=0.1 MPa)	Density	Viscosity	Thermal conductivity	Heat capacity
T	ρ	μ	λ	Cp
°C	kg/m^3	Pa.s	W/(m.K)	J/(kg.K)
0.01	999.84	0.00179	0.56109	4219.4
10	999.7	0.00131	0.58005	4195.2
20	998.21	0.00100	0.59846	4184.1
25	997.05	0.00089	0.60719	4181.3
30	995.65	0.00080	0.6155	4179.8
40	992.22	0.00065	0.63063	4179.4
50	988.03	0.00055	0.64359	4181.3
60	983.2	0.00047	0.65439	4185
70	977.76	0.00040	0.66313	4190.1
80	971.79	0.00035	0.67001	4196.8
90	965.31	0.00031	0.67527	4205.2
99.606	958.63	0.00028	0.67897	4215.2

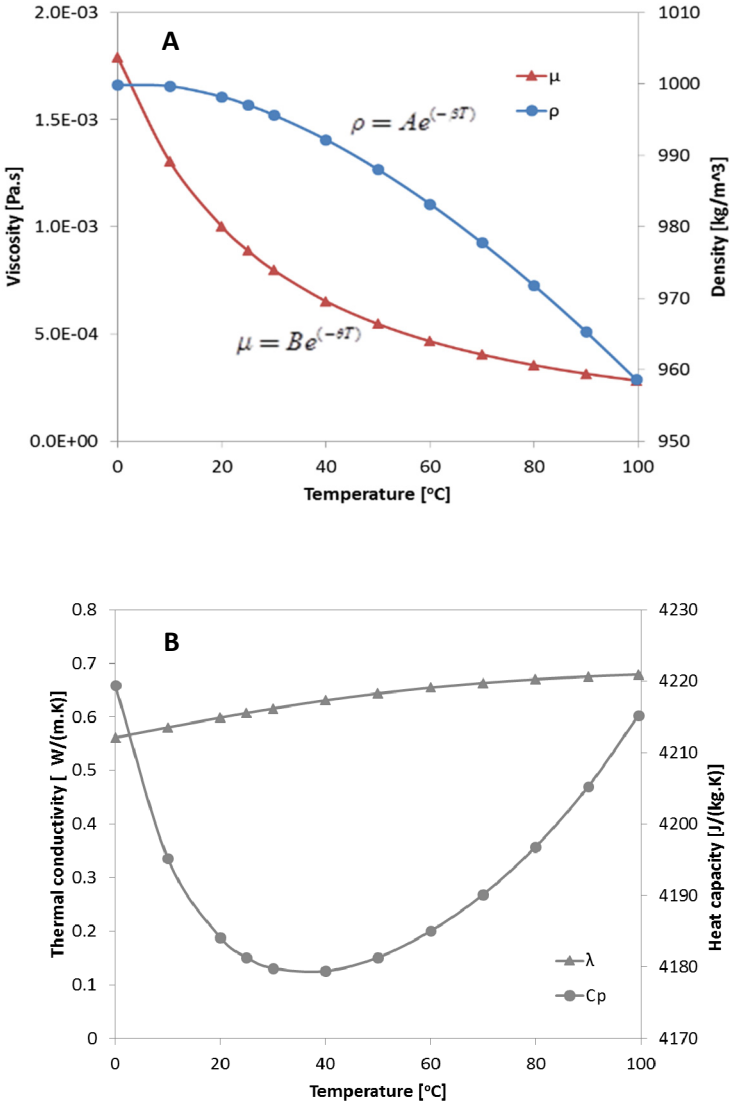

Figure 3-8. Water thermal properties vs. temperature. A: Water dynamic viscosity & density vs temperature, B: Water heat capacity & thermal conductivity vs temperature

3.2.3 Packing method

The best way of creating a homogeneous compact package is to fill the box in the vertical position (parallel to flow direction), and then turn it to horizontal direction (Van der Poel and Schenkeveld, 1998). Because of the geometry of the adopted set-up, it was not possible to use this conventional packing method. Moreover, the expansion and contraction of the box during heat transfer tests causes an extra problem. To overcome both problems it was decided to use two clay layers, one on the top and one on the bottom of the sand package. The clay layers help to keep the sand package homogeneous after repeated hot and cold displacement tests. Swelling and shrinking of the clay during the test will compensate for the expansion and contraction of the box which occurs during the hot or cold transfer tests. Therefore, the sand package remains homogeneous and no preferential flow path occurs in it.

To avoid air intrusion the box was half filled with de-aired water, and then the clay layer blocks were placed in it neatly and slowly (Figure 3-9-A). Then the wooden sticks with thermocouples mounted on them (Figure 3-3) were pressed into the bottom clay layer, at the right distance from the filters, along the centerline of the box (Figure 3-9-A). Next, the sand package with a high relative density of 85% (porosity=36%) was prepared by scattering dry sand in the water filled box (on top of the first clay layer) and in the meantime tamping it on the top layer (Figure 3-9-B). The study of Van der Poel and Schenkeveld (1998) has verified this packing method for a very homogeneous sand package. Finally, the top clay blocks were placed on top of the sand package (Figure 3-9-C). It is important to keep the set-up fully saturated during the whole procedure. At the end, the box lid was placed carefully to cover and seal the box (Figure 3-9-D).

The homogeneity of the sand package was checked by using a colored tracer in an isothermal vertical test and infrared photos in a non-isothermal vertical test.

It is important to note that, besides Baskarp sand, another sand type has been used with courser grains. The test series with the coarse sand type was not very successful, especially for high discharge rates, where some heterogeneity (preferential flow path) occurred on the top part of the sand package. Therefore, the results have not been presented here.

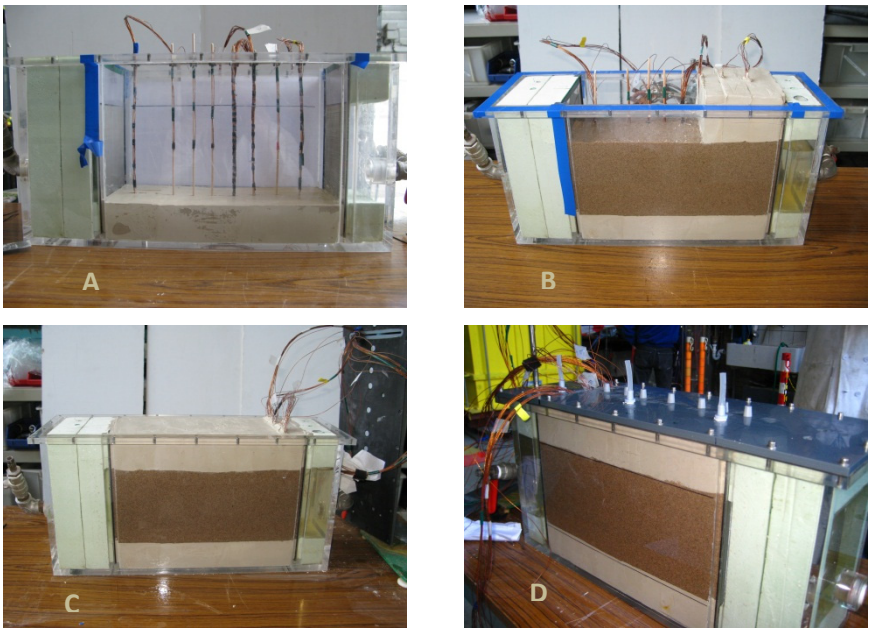

Figure 3-9. Packing procedure (A to D)

3.2.4 Experimental Procedure

Depending on the injected water temperature, two groups of experiments were categorized: hot injection and cold injection. In the first group, the sample was saturated with cold water, displaced by a flux of hot water. In the second group, the sample was saturated with hot water, displaced by a flux of cold water. Horizontal and vertical (by turning the box through 90 degrees) tests were conducted to study the effects of fluid density and viscosity on heat flow. Twenty-four experiments, with different combinations of hot and cold injection, horizontal and vertical, and 3 different injection velocities were carried out (see Table 3-4). To check the reproducibility, all tests, except the vertical tests with the lowest velocities (ΔH=20 cm), have been repeated 2 or 3 times.

The sand was saturated with de-aired water with an initial temperature, T_0. During the tests, water at a fixed temperature, T_i, was injected into the sand layer. The experiments were conducted with hot injection into a cold box, continued until the temperature in the box became uniform, followed by cold injection. All experiments were carried out at a constant room temperature of 20±1 [^{o}C]. In all tests, initial and injection temperatures have been kept at

around 20 [°C] (representing the cold condition) and around 60 [°C] (representing the hot condition).

The total head in the box during the tests was maintained by fixing the level of water inside the inflow and outflow tanks through an "overflow system" (see Figure 3-2). As mentioned above, the flow rate was measured by a flow meter at the inlet and a discharge weight measurement at the outlet, and the temperature distribution in the box was measured by a set of thermocouples (Figure 3-4). The temperature was measured every 10 seconds with ±0.5 [°C] accuracy.

To be sure that the temperature of the injected water is uniform at the inlet buffer zone, a perforated tube was placed at the inlet buffer zone (see Figure 3-2). In the horizontal experiments, the lid entry was utilized to inject the water, and the inlet entry was utilized to drain it. During the first 50-100 seconds, the injected water enters into the box through the perforated tube, while the outlet is kept closed. In this case, water with a high velocity circulates inside the inlet buffer zone and leaves without entering the sand package. After 50-100 seconds, a uniform temperature develops in the outlet buffer zone. After this, the inlet entry is closed and the outlet is opened, resulting in a uniform front flow from the inlet buffer zone toward the outlet buffer zone. The experimental results have shown that this procedure has resulted in effectively uniform flow, though an early slight heat conduction from the inlet buffer zone to the sand package cannot be ignored.

Table 3-4. Experiment description

Hot injection (hot water replacing cold water)						Cold injection (cold water replacing hot water)					
Horizontal			Vertical			Horizontal			Vertical		
ΔH=90 cm	ΔH=50 cm	ΔH=20 cm	ΔH=90 cm	ΔH=50 cm	ΔH=20 cm	ΔH=90 cm	ΔH=50 cm	ΔH=20 cm	ΔH=90 cm	ΔH=50 cm	ΔH=20 cm
$T_i/T_0>1$		$\rho_i/\rho_0<1$		$\mu_i/\mu_0<1$		$T_i/T_0<1$		$\rho_i/\rho_0>1$		$\mu_i/\mu_0>1$	

3.2.5 Infrared images of temperature profile

To obtain an overview of heat flow in a porous domain with initial and boundary conditions typically existing in deep low-enthalpy geothermal

systems, the temperature profile during the experiments was photographed using an infrared (IR) camera. Shots of the thermal front were taken from the exterior side of the box. The insulator, hard foam sheet, was removed for a few seconds during the IR shots. The IR images, though, are not comparable to the thermocouple measurements because Plexiglas is not transparent to infrared, and these images represent only the temperature field near the outer side of the Plexiglas.

Figure 3-10 shows the development of hot and cold fronts in a horizontal test set-up, ΔH = 90 [cm]. The horizontal lines in these figures indicate the boundary between the sand and the clay layers. The figure shows that the heat front for both cold and hot injection has an asymmetric profile, though it is less pronounced for the cold injection.

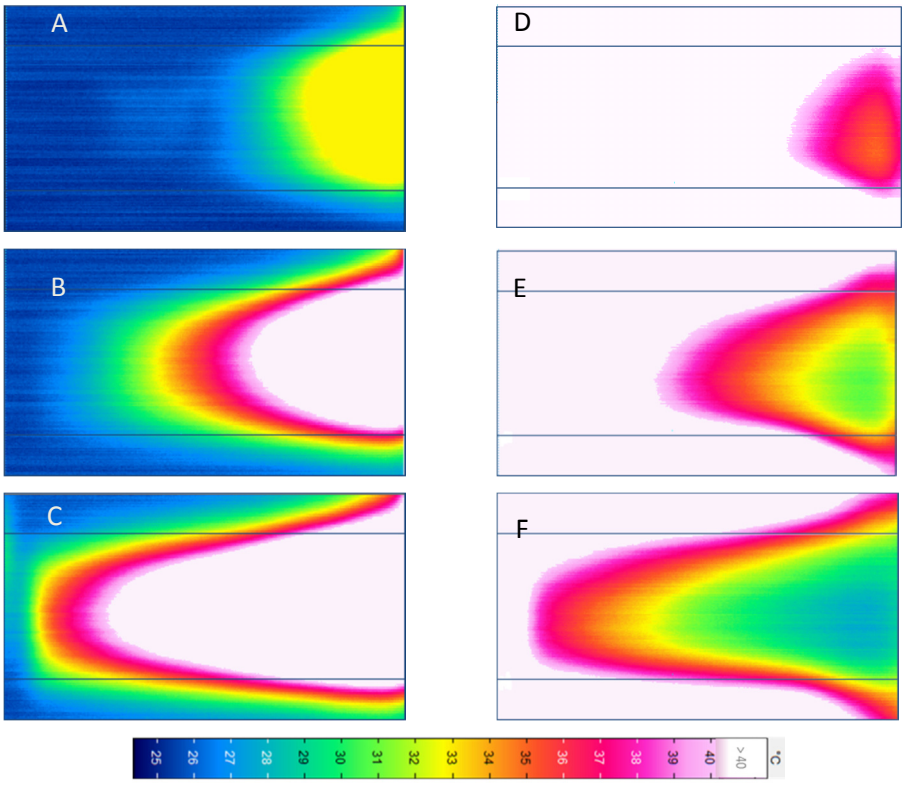

Figure 3-10. Infrared pictures of thermal front. A-C: hot injection (time = 600, 1500, 5000 s), D-F: Cold injection (time = 600, 1500, 5000 s)

The thermal front shape and position are dependent on the water velocity, which is, in both hot and cold injections, affected by the involved thermal and physical mechanisms: forced convection, natural convection (density effect), conduction, and viscosity effect. The position of the thermal front is mainly affected by the forced convection, and its shape is mainly affected by the natural convection and viscosity variations. Heat conduction in this test set-up has a considerable effect on heat loss/gain with the surrounding clay layers (bleeding) and a small effect on the front position.

During hot injection, the density and viscosity decrease (Figure 3-8-A) and, with the assumption of a constant intrinsic permeability (Greenberg et al., 1968), the hydraulic conductivity increases. A combination of these mechanisms gives rise to the generation of buoyancy forces that lift the lighter water upwards, creating a progressively higher velocity zone in the upper part of the sand package and a non-uniform flow field. Figure 3-11-left schematically explains these phenomena.

During cold injection, on the other hand, the injected water tends to move downwards, under its own weight, but, as the initial temperature in the existing water is higher than the injected one, a relatively higher hydraulic conductivity zone still exists on top, leading to an asymmetric front. However, the asymmetry of the heat front in the cold injection tests is less pronounced than that in the hot injection test (Figure 3-11-right).

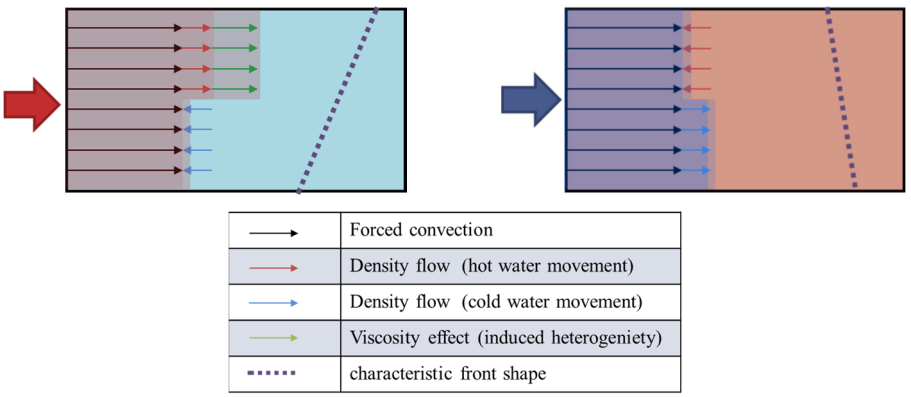

Figure 3-11. Schematic picture of phenomena which affect the heat front shape and position in hot injection (left) and cold injection (right) scenarios (the effect of bleeding has not been shown here).

3.2.6 Measured temperature profile

As mentioned earlier, 24 experiments were conducted and the temperature distribution inside the box was measured using 6 series of thermocouples, (Figure 3-4). Figure 3-12 shows the temperature profiles from the C-series thermocouples at different time intervals. This series is located 15 [cm] away from the injection inlet and consists of 7 thermocouples which placed symmetrically around vertical mid-point.

Initially, the effect of viscosity and density on the heat front shape and position is more pronounced, due to relatively higher temperature differences between the injected and the existing water. This effect is more pronounced in tests with higher head gradients (ΔH=90 [cm] and 50 [cm]), showing the significance of viscosity effects on heat flow in such a condition. This finding is important, indicating that the dependency of density and viscosity on temperature within the studied temperature range is important and should be considered in the design of low-enthalpy geothermal systems. In the following sub-sections, we analyze these effects in detail.

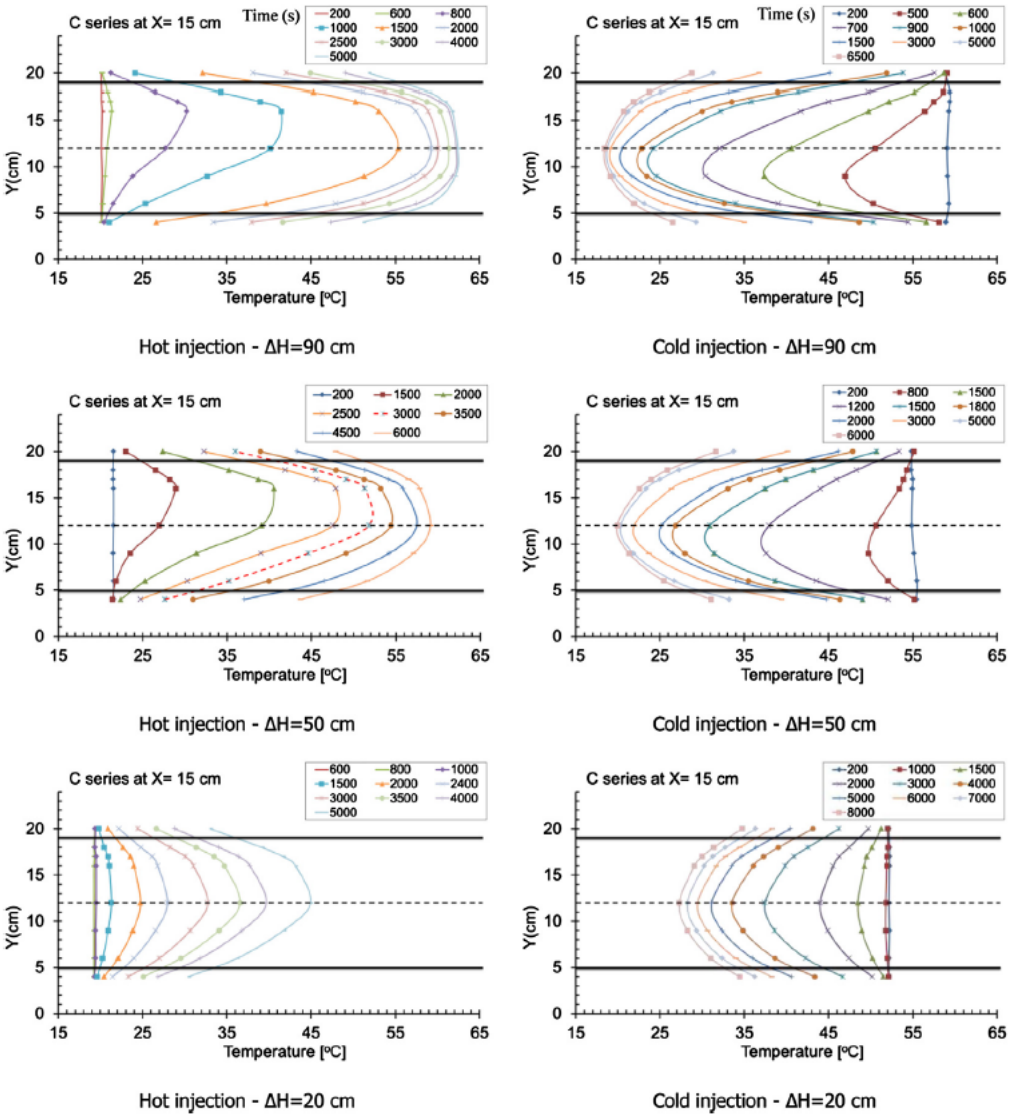

Figure 3-12. Temperature profiles in horizontal displacement tests at thermocouple series C with different total head gradients. Left: hot injection, Right: cold injection. Time in seconds is shown in the block legend in each picture

3.2.7 Viscosity effect

Fluid viscosity in a porous domain has a significant effect on the hydraulic conductivity. To study the effect of the studied temperature range on the hydraulic conductivity of the Baskarp sand, Darcy's experiment, by using constant head method, was conducted. Figure 3-13 shows some measured hydraulic conductivities of the sand as a function of temperature (dots). The figure also shows the calculated hydraulic conductivity as solid blue line (using Eq.(4.11)). Obviously, the measured hydraulic conductivities match the calculated ones.

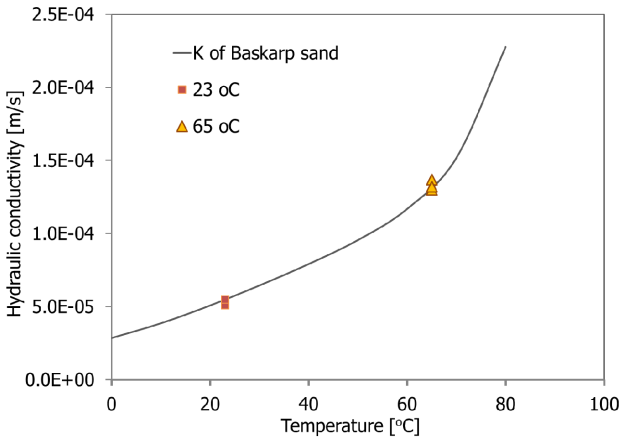

Figure 3-13. Variation of hydraulic conductivity with temperature in the test set-up (points are showing the measured hydraulic conductivity of Baskarp sand at different temperatures)

Figure 3-14 shows an example of the variation and distribution of the sand hydraulic conductivity during a horizontal hot injection test. This figure shows the temperature measurements obtained from all thermocouples in the porous medium of the test setup (see, Figure 3-4). Horizontal axis shows the horizontal location of the thermocouples from the inlet and vertical axis shows the calculated hydraulic conductivity. Vertical position of each thermocouple demonstrated by different color and symbol in this figure.

The figure clearly shows the increase of the hydraulic conductivity with time and location. The buoyancy effect of hot water is obvious in Figure 3-14-B, C, and D, where symmetric thermocouples do not show similar hydraulic conductivities. Figure 3-14-A shows a homogenous hydraulic conductivity profile, while others, due to the displacement of cold water by hot water.

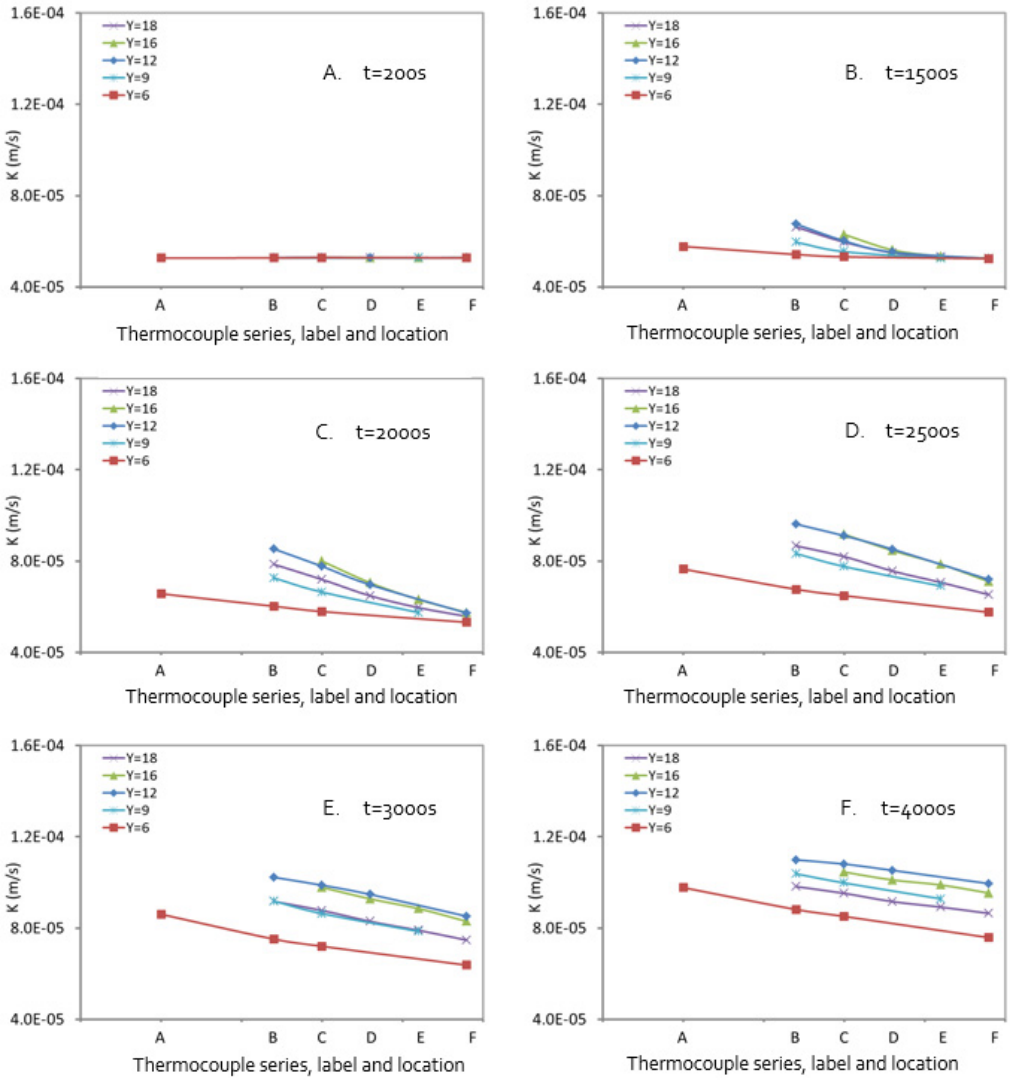

Figure 3-14. Hydraulic conductivity of Baskarp sand during a horizontal replacement of cold water by hot water at different time.

3.2.8 Density effects

To investigate the buoyancy effect, vertical and horizontal experiments were conducted. In the vertical set-up, the gravity effect on the heat front is symmetric, while in the horizontal set-up, it is asymmetric.

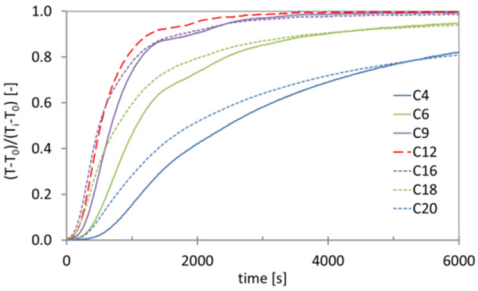

A: Horizontal flow – ΔH=90 cm, hot injection

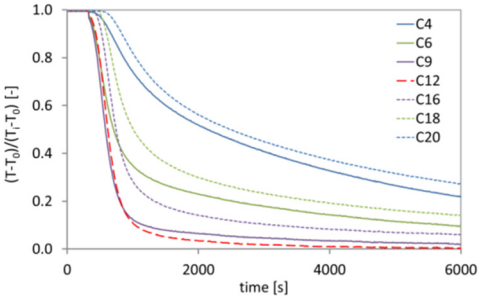

B: Horizontal flow – ΔH=90 cm, cold injection

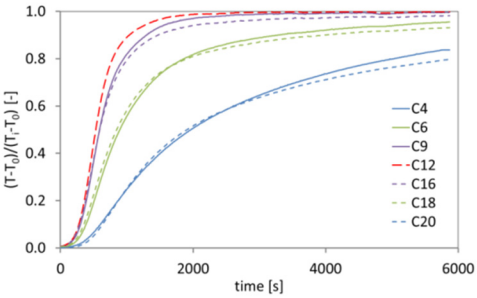

C: Vertical-downward flow – ΔH=90 cm , hot injection

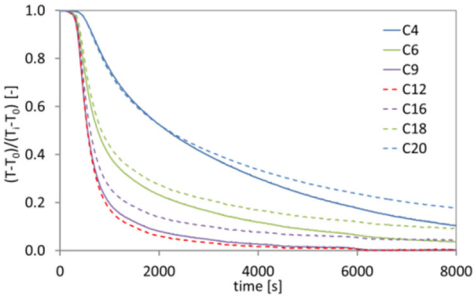

D: Vertical-downward flow – ΔH=90 cm , cold injection

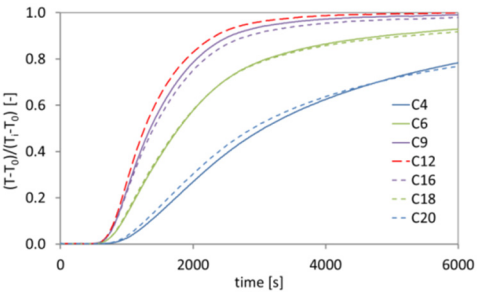

E: Vertical-upward flow – ΔH=90 cm , hot injection

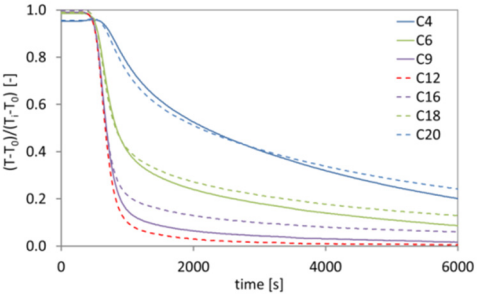

F: Vertical-upward flow – ΔH=90 cm , cold injection

Figure 3-15. Breakthrough curves for ΔH =90 cm tests, with different injection direction.

Temperature profiles and breakthrough curves for all experiments were constructed at all thermocouple locations. Figure 3-15 shows the temperature profiles at the C-series of thermocouples. C12 is in the middle of the sand layer and should exhibit the least heat loss/gain. In a hypothetical homogeneous

medium with no effects of density and viscosity variations, C9 and C16, C6 and C18, and C4 and C20 should exhibit equal temperatures. Figure 3-15-A and B show the breakthrough curves for horizontal experiments. As a result of the density effect, the thermocouples located in the top half of the box exhibit higher temperature than their symmetric counterparts in the bottom half of the box. With elapsing time, the temperature differences recorded at the symmetrically placed thermocouples in the two halves of the box become less and less significant.

Figure 3-15-C and D show the breakthrough curves for vertical-downward flow experiments, and Figure 3-15-E and F show the breakthrough curves for vertical-upward flow experiments. For the hot injection tests (C and E), in both the upward and downward flow tests, the breakthrough curves of the symmetrically placed thermocouples around the vertical midpoint (y=12.5 cm) exhibit a reasonable match. However, for the cold injection tests (D and F), the curves do not match. This might be attributed to the fact that, in the cold injection tests, the box was initially not uniformly heated. The difference at the beginning of the curves in Figure 3-15-F explains that there was indeed a non-uniform distribution of temperature in that test.

3.3 Conclusion

An experimental study has been conducted to analyze heat transport in a porous domain subjected to cold and hot injection scenarios. The experimental set-up and the initial conditions and boundary conditions are made similar to those that exist in a natural low-enthalpy geothermal system. Two main issues are examined: the effect of fluid density and viscosity on heat and fluid flow, and their significance.

The experimental set-up consists of a fully saturated sand layer surrounded by two impermeable clay layers, subjected to different fluid flow rates and injected temperatures. Vertical and horizontal test set-ups were utilized. Heat flow was measured using an Infrared camera and a series of thermocouples. Both types of measurements had shown that, in the horizontal experiments, the heat front was asymmetric; and, in the vertical experiments, it was symmetric.

The following chapter will quantify the effect of density, viscosity and thermal dispersion on heat flow based on the experimental results demonstrated in the current chapter.

Chapter 4

Numerical analysis and modelling

In this chapter, the experimental results illustrated in the previous chapter are analyzed using the finite element package COMSOL. An intensive finite element calculation has been carried out to simulate the test set-up and study the influence of variation of density and viscosity on the heat flow in deep low-enthalpy geothermal conditions. Also, a series of backcalculation studies comparing the numerical results to the experimental results has been conducted to quantify the magnitude of the thermal dispersion. A constitutive model describing the thermal dispersion in terms of fluid density, viscosity and pore geometry, taking into consideration different injection scenarios, has been developed.

This chapter is based on the paper “Experimental–numerical study of heat flow in deep low-enthalpy geothermal conditions", published in the Renewable Energy journal (Saeid et al., 2014).

4.1 Introduction

Of paramount importance to advancing our understanding of heat transfer in porous media is the study of thermal dispersion. Thermal dispersion in porous media takes place as the result of heat dispersal due to material heterogeneity, other than that which takes place due to heat conduction. The amount of thermal dispersion depends mainly on fluid flow velocity, and the

dispersion occurs along the flow direction (longitudinal dispersion) and perpendicular to the flow direction (transversal dispersion). Research efforts have led to the development of several approaches to evaluate thermal dispersion (Hsu and Cheng, 1990; Anderson, 2005; Molina-Giraldo et al., 2011). Conventionally, thermal dispersion is ignored due to the dominance of thermal conduction, in contrast to solute molecular diffusion (Bear and Cheng, 2010). Experimental results from Mori et al. (2005) showed that thermal dispersion effects were insignificant and independent of water fluxes ranging between 0.6×10^{-6} and 0.3×10^{-3} [m/s]. However, a study conducted by Hopmans et al. (2002), using heat pulse probe measurements, showed that ignoring thermal dispersivity, for thermal dispersion larger than thermal conductivity, leads to an inaccurate calculation of water flux density. Analogous to solute transport, the effect of thermal dispersion on heat transport is significant when the Peclet number, the ratio of conduction to convection, is relatively large (Rau et al., 2012). Metzger et al. (2004) introduced a dispersion model based on the thermal Peclet number.

Thermal dispersion is generally defined as a function of fluid velocity and grain size (Lu et al., 2009, Sauty et al., 1982, Nield and Bejan, 2006). Sauty et al. (1982) described the thermal dispersion as a linear function of velocity. Recently, Rau et al. (2012) suggested a dispersion model as a function of the square of the thermal front velocity. They also claimed that dispersivity coefficients are intrinsic properties of the porous media. The magnitude of thermal dispersivity is another issue of disagreement. Smith and Chapman (1983) assert that thermal dispersion has the same order of magnitude as solute dispersivities, while Ingebritsen and Sanford (1999) ignore it. Vandenbohede et al. (2009) suggested that thermal dispersivities are less scale-dependent and are small in comparison to solute dispersivity values.

In chapter 3, heat flow in a fully saturated porous domain subjected to cold and hot injection was studied, and the effects of fluid density and viscosity on breakthrough curves under low-enthalpy geothermal system conditions were examined. For this, a series of laboratory experiments was carried out. In this chapter, a backcalculation study comparing the numerical results to the experimental results has been conducted to examine the effect of thermal dispersion, and to develop a constitutive model describing thermal dispersion in terms of fluid density, viscosity and pore geometry, taking into consideration different injection scenarios.

4.2 Numerical study

A numerical study using the finite element method has been carried out to analyze the experimental results and quantify the effect of density, viscosity and thermal dispersion on heat flow in a porous domain subjected to typical low-enthalpy geothermal conditions. Backcalculation analysis has been carried out to formulate a thermal dispersion constitutive model capable of quantifying the amount of thermal dispersion. The model is a function of the fluid velocity, temperature, density, viscosity and grain geometry.

4.2.1 Governing equations

Heat flow in a saturated porous medium typically involves heat convection and conduction associated with thermal dispersion, occurring due to tortuosity at the pore scale. In this section, the governing equations for heat and fluid flow in a two-phase domain are given. Formulations describing thermal dispersion and fluid density and viscosity as functions of temperature are addressed.

4.2.1.1 *Heat flow*

In a rigid (non-deforming) fully saturated medium, the macroscopic energy balance equation for the solid phase (in the absence of fluid) can be described, using Fourier's law, as

$$\frac{\partial}{\partial t}[(1-\phi)\rho_s c_s T_s] - (1-\phi)\nabla\cdot(\boldsymbol{\lambda}_s \nabla T_s) = 0 \qquad (4.1)$$

and for the fluid phase, as

$$\frac{\partial}{\partial t}(\phi\rho_f c_f T_f) + \nabla\cdot(\rho_f c_f \mathbf{q} T_f) - \phi\nabla\cdot(\boldsymbol{\lambda}_f \nabla T_f) = 0 \qquad (4.2)$$

where T [^{O}C] is the temperature, ϕ is the porosity, ρ [kg/m^3] is the mass density, c [J/kg.K] is the specific heat capacity, $\boldsymbol{\lambda}$ [W/m.K] is the thermal conductivity tensor, and **q** [m/s] is the Darcy velocity. The subscription f refers to the pore fluid and s to the solid matrix.

Working at the macroscopic level, it is reasonable to assume that the phases of a geothermal system are locally in a state of thermal equilibrium. Setting $T_s = T_f = T$ and adding Eqs. (4.1) and (4.2), the energy balance equation for a saturated porous medium can then be described as

$$\frac{\partial}{\partial t}(\rho cT) + \nabla \cdot (\rho_f c_f \mathbf{q}T) - \nabla \cdot (\boldsymbol{\lambda} \nabla T) = 0 \tag{4.3}$$

where the thermal conductivity, $\boldsymbol{\lambda}$, may be delineated as

$$\boldsymbol{\lambda} = \boldsymbol{\lambda}_{eq} + \boldsymbol{\lambda}_{dis} \tag{4.4}$$

in which $\boldsymbol{\lambda}_{eq}$ is the equivalent thermal conductivity and $\boldsymbol{\lambda}_{dis}$ is the thermal dispersion. The latter will be discussed thoroughly in sub-section 4.2.1.4. The equivalent thermal conductivity, and also the volumetric heat capacity, can be described in terms of a local volume average, as

$$\begin{aligned} \boldsymbol{\lambda}_{eq} &= (1-\phi)\boldsymbol{\lambda}_s + \phi \boldsymbol{\lambda}_f \\ \rho c &= (1-\phi)\rho_s c_s + \phi \rho_f c_f \end{aligned} \tag{4.5}$$

Physically, in a two-phase domain, the velocity of the thermal field is slower than the velocity of the fluid field, defined normally by a retardation factor, R_d, which is related to the ratio between the solid volumetric heat capacity and that of the water. Replacing the Darcy velocity $\mathbf{q}$ by the pore fluid velocity, $\boldsymbol{v} = \mathbf{q}/\phi$, Eq. (4.3) can be re-written as

$$\frac{\partial T}{\partial t} = -R_d \boldsymbol{v} \cdot \nabla T + \mathbf{D} \nabla^2 T \tag{4.6}$$

where

$$R_d = \frac{\phi \rho_f c_f}{(1-\phi)\rho_s c_s + \phi \rho_f c_f} \tag{4.7}$$

is the retardation factor, and

$$\mathbf{D} = \frac{\boldsymbol{\lambda}}{\rho c} \tag{4.8}$$

is the thermal diffusivity [$m^2 s^{-1}$].

4.2.1.2 *Fluid flow*

Fluid flow in a saturated porous domain can be expressed as

$$\phi \frac{\partial \rho_f}{\partial t} + \nabla \cdot (\rho_f \mathbf{q}) = 0 \tag{4.9}$$

where **q** is the Darcy flow velocity, described as

$$\mathbf{q} = -\frac{\boldsymbol{\kappa}}{\mu}(\nabla P - \rho_f \mathbf{g} \nabla z) \tag{4.10}$$

in which $\boldsymbol{\kappa}$ is the intrinsic permeability tensor [m^2], μ [Pa.s] is the fluid dynamic viscosity, **g** [m/s^2] is the gravity vector, and *P* [Pa] is the hydraulic pressure. The intrinsic permeability is a property of the solid material, though, in practice, the hydraulic conductivity is usually defined as

$$\mathbf{K} = \boldsymbol{\kappa} \mathbf{g} \frac{\rho_f}{\mu} \tag{4.11}$$

which is a function of the intrinsic permeability and the fluid density and dynamic viscosity.

4.2.1.3 *Density and viscosity dependency on temperature*

In geothermal systems, the fluid density and viscosity may vary with temperature, pressure and concentration (Diersch and Kolditz , 2002), as

$$\rho_f = \rho_f(T, P, C) \tag{4.12}$$

The total differential of Eq. (4.12) yields (Elbashbeshy and Bazid, 2000)

$$\frac{1}{\rho_f}\partial \rho_f = \underbrace{\left(\frac{1}{\rho_f}\frac{\partial \rho_f}{\partial T}\right)}_{-\beta}\partial T + \underbrace{\left(\frac{1}{\rho_f}\frac{\partial \rho_f}{\partial P}\right)}_{\gamma}\partial P + \underbrace{\left(\frac{1}{\rho_f}\frac{\partial \rho_f}{\partial C}\right)}_{\alpha}\partial C \tag{4.13}$$

where the term *β* is the fluid thermal expansion, γ is its compressibility, and α is the volumetric solubility. Assuming *α*, *β* and *γ* are constants, integration of Eq. (4.13) leads to the equation of state of the fluid density, of the form:

$$\rho_f = \rho_{f_0}\, e^{-\beta(T-T_0)+\gamma(P-P_0)+\alpha(C-C_0)} \tag{4.14}$$

in which ρ_{f0} is the initial density of the fluid at an initial temperature, T_0 , an initial pressure, P_0 , and an initial concentration, C_0.

This equation can be approximated linearly as

$$\rho_f = \rho_{f_0}(1-\beta(T-T_0)+\gamma(P-P_0)+\alpha(C-C_0)) \tag{4.15}$$

Considering the adopted test set-up and the involved initial and boundary conditions, the density and viscosity variations with pressure are negligible. Also, in this test set-up, water was utilized as an advective medium, and thus the effect of the concentration on density and viscosity can be ignored. Accordingly, the water density may be described as

$$\rho_f = \rho_{f_0} e^{-\beta(T-T_0)} \tag{4.16}$$

The water viscosity can be treated in the same way, yielding

$$\mu = \mu_{f_0} e^{-\theta(T-T_0)} \tag{4.17}$$

4.2.1.4 ***Thermal dispersion***

Thermal dispersion mainly occurs due to variations in fluid flow paths and velocity at pore spaces in heterogeneous domains (Molina-Giraldo et al., 2011). Thermal convection and conduction interactively give rise to thermal dispersion along the flow direction (longitudinal dispersion) as well as perpendicular to the flow direction (transversal dispersion). As thermal dispersion is associated with heat flow in heterogeneous domains, its quantification and determination may be rather complicated. Several experimental investigations have been presented to discuss this issue, but so far no consensus has been reached on a specific model, neither on the type of model. There have been lots of discussions about the similarity between solute dispersion and thermal dispersion. However, due to the dominance of thermal diffusion (**D** in Eq.(4.6)) in heat transfer, compared to solute diffusion, thermal dispersion has been ignored, see for example Woodbury and Smith, (1985). However, in many other studies, the thermal dispersion has been considered important.

Several models describing thermal dispersion have been introduced. In most of them, thermal dispersion is assumed to be a function of fluid velocity and grain size (Lu et al., 2009, Sauty et al., 1982). Molina-Giraldo et al. (2011)

showed that, for Darcy velocities greater than 10^{-8} [m/s], thermal dispersion is scale dependent: higher at larger scales (formation levels) and smaller at smaller scales (experimental set-up levels). They stated that thermal dispersion is negligible for fine sands, clays, and silts with $q < 10^{-8}$ [m/s]. In contrast, Mori et al. (2005) showed that thermal dispersion is independent of water fluxes ranging between 6×10^{-5} and 3.2×10^{-6} [m/s]. Hidalgo et al. (2009) asserted that the effect of heterogeneity in hydraulic conductivity on heat flow, in a small scale convection, can cause thermal dispersion.

Despite the uncertainty and contradiction in defining and quantifying the causes of thermal dispersion, several empirical formulae have been proposed. They mostly quantify the thermal dispersion coefficient in terms of Darcy fluid velocity. For example, Sauty et al. (1982) introduced a linear relationship of the form

$$\begin{aligned} \boldsymbol{\lambda} &= \boldsymbol{\lambda}_{eq} + \boldsymbol{\lambda}_{dis} \\ \boldsymbol{\lambda}_{dis} &= \boldsymbol{\alpha}\rho_f c_f \mathbf{q} \end{aligned} \tag{4.18}$$

in which α is a thermal dispersion coefficient.

Lu et al. (2009) stated that, in saturated soils, the pore water velocity and soil texture (size, shape, and tortuosity of the soil pores) are two major factors determining the magnitude of thermal dispersion. They measured the dispersivity in three different sand types, for various flow rates, and showed that thermal dispersion can be described by a power function of the form

$$\lambda_{dis} = kJ_w^{0.9} \tag{4.19}$$

where k is a fitting parameter related to soil texture, and J_w is the water flux [ms^{-1}].

Rau et al. (2012) , showed experimentally that thermal dispersion, within natural groundwater flow velocities, can be approximated in terms of a thermal dispersivity coefficient and the square of the thermal front velocity, as

$$D = \frac{\lambda_0}{\rho c} + \beta_{l,t}\left(\frac{\rho_w c_w}{\rho c} q\right)^2 \tag{4.20}$$

where $\beta_l \approx 1.478$ and $\beta_t \approx 0.4$ are longitudinal and transversal thermal dispersion coefficients, respectively, and λ_0 is the bulk thermal conductivity, calculated as

$$\lambda_0 = \lambda_w^{\phi} \lambda_s^{(1-\phi)} \tag{4.21}$$

4.2.2 Numerical modeling of test set-up

In Section 3.2.6, despite the small scale geometry the experimental results show that, in a typical temperature range of a low-enthalpy hydrothermal system, heat flow is non-uniform. This is attributed to the dependency of the fluid density and viscosity on temperature. Also, and due to the micro heterogeneity of the sand package, it is likely that thermal dispersion is significant. To investigate these issues and study their effects at the reservoir level (up-scaled level), finite element analysis was conducted.

4.2.2.1 *Finite element model*

The finite element package COMSOL (2011), has been utilized as a framework for modeling the experimental test set-up. Heat flow in the sand and clay layers is described by Eq. (4.3); however, for the clay layers, **q** is set equal to zero. The fluid flow in the sand layer is described by Eq. (4.10) and the dependency of density and viscosity on temperature is described by Eqs. (4.16) and (4.17), respectively. Due to the dependency of density and viscosity on temperature, the problem is non-linear.

The physical model was discretized in two-dimensions, describing a sand layer (0.337 [m] $\times$ 0.15 [m]), and two clay layers (0.337 [m] $\times$ 0.05 [m]). 2D triangular elements (three nodes per element) were utilized. To investigate the possible occurrence of thermal dispersion, the numerical dispersion was reduced by utilizing a relatively fine mesh with a maximum element size of 1[mm] for the sand layer (Figure 4-1). In total, 137145 elements were utilized.

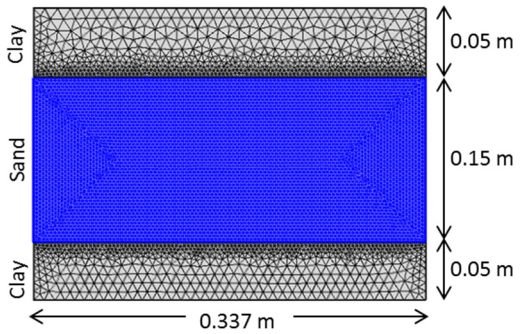

Figure 4-1. FEM mesh

4.2.2.2 *Initial and boundary conditions*

The initial temperature in the sand and clay layers, at t=0, is

$$T(x,y,0) = T_0 \tag{4.22}$$

At the entry boundary of the sand layer, the injection temperature is constant and equal to the measured temperature inside the inlet buffer zone, such that

$$T(x_{in},y_{in},t) = T_i \tag{4.23}$$

At the clay layer boundaries (insolated boundaries), the boundary conditions are described as

$$-\mathrm{n}.(\lambda_{eq}\nabla T) = 0 \tag{4.24}$$

where n is the normal vector to the surface. The injected water pressure at the entry boundary of the sand layer is

$$P(x_{in},y) = P_{in} = \rho(T_i)g(h_{in} - y) \tag{4.25}$$

where $\rho(T_i)$ is the density of the injected water, which is, for a specific test, constant; h_{in} is the height of the inflow tank, 2 [m]; and y is the height of the measured point at the entry boundary, see Figure 3-2.

The output pressure boundary for the sand layer is

$$P(x_{out},y) = P_{out} = \rho(T_{out})g(h_{out} - y) \tag{4.26}$$

where $\rho(T_{out})$ is the density of the output water, varying in time; h_{out} is the height of the outflow tank, constant in a specific test, but varying for different tests; and y is the height of the measured point at the outlet boundary.

Thermal and hydraulic parameters of the model are listed in Table 4-1. The initial values for water density and viscosity were calculated based on Lide and David (1990). Thermal conductivity, porosity and intrinsic permeability of the sand layer were measured experimentally; see Figure 3-7 for porosity and permeability.

Table 4-1. Thermal and hydraulic parameters of the porous medium and two adjacent layers used in COMSOL simulation

Parameter	Value	Unit	Description
β	8e-4	[1/K]	Thermal expansion coefficient of the fluid
ϕ	0.36	[-]	Porosity
ρ_s	2650	[kg/m^3]	Baskarp sand density
c_s	2000	[J/kg.K]	Baskarp sand heat capacity
λ_s	2.5	[W/m.K]	Baskarp sand thermal conductivity
k_B	5.22e-12	[m^2]	Porous medium (Baskarp sand) permeability
ϕ_t	0.05	[-]	Clay porosity
k_t	1e-18	[m^2]	Clay permeability
ρ_t	1750	[kg/m^3]	Clay density
λ_t	2	[W/m.K]	Clay thermal conductivity
c_t	2000	[J/kg.K]	Clay heat capacity
d_{50B}	130 e-6	[m]	Sand grain diameter
g	9.81	[m/s^2]	Gravity

4.2.2.3 *Numerical results*

All experiments, horizontal and vertical, have been simulated and the numerical results compared to the experimental results. Initially, thermal dispersion was not considered, and hence the total thermal conductivity, $\boldsymbol{\lambda}$ in Eq.(4.3), is assumed to be equal to the equivalent thermal conductivity. Figure 4-2 shows the numerical breakthrough curves of a number of experiments at point C12 (see Figure 3-4), with ΔH = 90 cm, together with the associated experimental results. Figure 4-2-A and B show the results of the horizontal experiments, and Figure 4-2-C and D show the results of the vertical ones. The figures reveal that the numerical results exhibit sharper thermal fronts than the corresponding experimental results. An extensive mesh convergence and optimization study was conducted to reduce the possible occurrence of numerical dispersion due to mesh dependency. Having done this, it is evident that the difference between the numerical results and the experimental results are mainly physical, most likely due to neglecting thermal dispersion in the simulations.

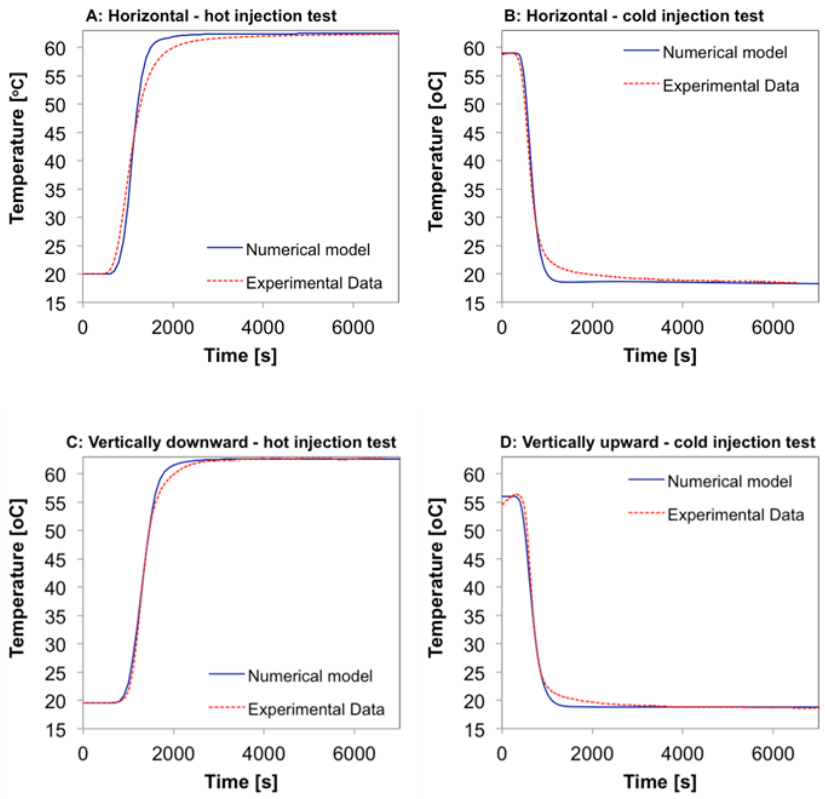

Figure 4-2. Experimental breakthrough curves vs. numerical results

Figure 4-3 highlights the difference between the normalized breakthrough curves of the experimental and numerical results for the different scenarios. The breakthrough time, which is mainly controlled by both the retardation factor and hydraulic conductivity, of the numerical and experimental results shows good agreement. But, the tail of the experimental breakthrough curves (Figure 4-3), which is controlled by the thermal conductivity, is longer than that of the numerical breakthrough curves. This difference is more significant for the horizontal test cases. The long tail of the breakthrough curves obtained from laboratory experiments are attributed to thermal dispersion.

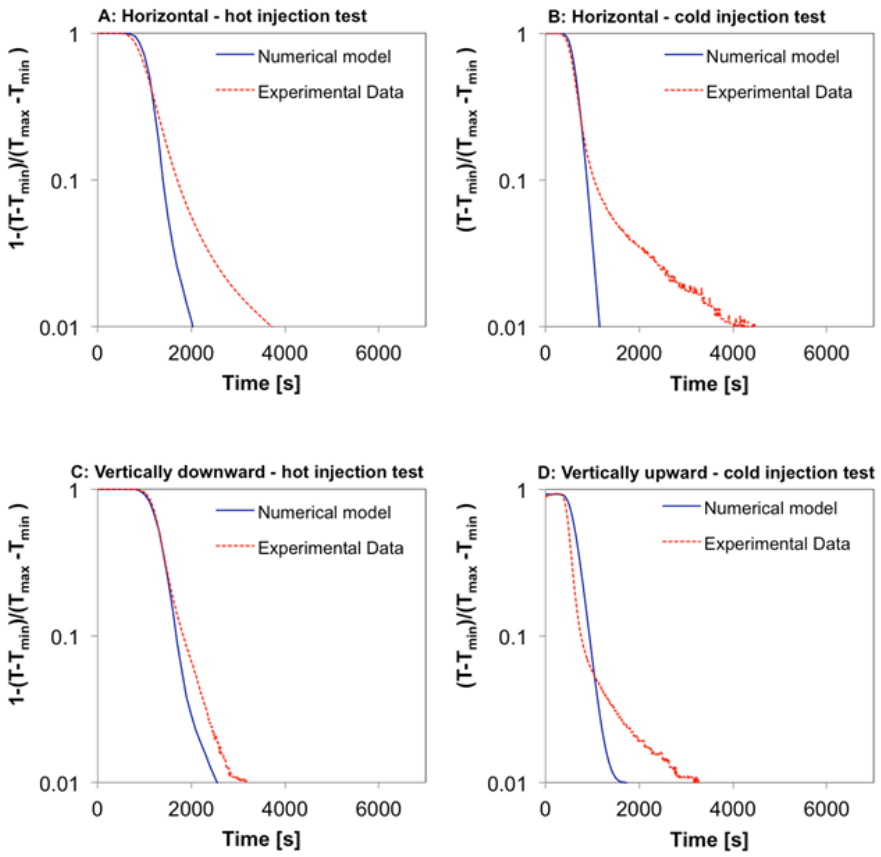

Figure 4-3. Normalized breakthrough curves of experimental and numerical results, revealing the inadequacy of the model without dispersion for different scenarios.

4.2.3 Backcalculation of thermal dispersion

A backcalculation procedure was conducted to quantify the amount of thermal dispersion induced during the test. An iterative procedure comparing the experimental results to the numerical results, while modifying the value of the thermal dispersion, was conducted. As the difference between the experimental results and the numerical results was relatively small, minimization of the error was conducted manually.

Via backcalculation procedure, a dispersion model describing λ_{dis} based on Smith and Chapman (1983), which is an extension of the Bear and Cheng model (2010) for solute dispersion, has been implemented in COMSOL. This

model is physically sound, and suitable for two- and three-dimensional flow, and the involved parameters are experimentally determinable. The basic dispersion model given by Smith and Chapman (1983) is:

$$\lambda_{dis,xx} = \frac{\rho_f c_f}{v}(\alpha_L v_x^2 + \alpha_T v_y^2)$$
$$\lambda_{dis,yy} = \frac{\rho_f c_f}{v}(\alpha_T v_x^2 + \alpha_L v_y^2) \qquad (4.27)$$
$$\lambda_{dis,xy} = \lambda_{dis,yx} = V\rho_f c_f \left((\alpha_L - \alpha_T)\frac{v_x v_y}{v^2} \right)$$

in which v_x and v_y are the velocity components in the *x* and *y* directions, and $v = \sqrt{v_x^2 + v_y^2}$. α_L is defined as the length that characterizes the microscopic configuration in a representative elementary volume (REV) (Bear and Cheng, 2010). Thus for a fully saturated porous medium, α_L should be the same order of magnitude as the size of a typical pore, and α_T is of the order of 8 to 24 times smaller than α_L (Bear and Cheng, 2010).

Eq. (4.27) was implemented in COMSOL and several analyses were conducted by varying α_L and α_T until a best match between the numerical results and experimental results was obtained. Figure 4-4 shows the back-calculated longitudinal and transversal dispersions, $\lambda_{dis,xx}$, and $\lambda_{dis,yy}$ respectively.

It is important to mention that the average water velocity is calculated at each measurement point in time. The average velocity is not the same, even for tests with similar ΔH: tests with similar ΔH but different $\Delta T=(T_i-T_0)$, show different average velocities (Figure 4-5).

Studying these figures, for a temperature range between 20 [°C] and 60 [°C] and Darcy velocity range between 7×10^{-6}[m/s] and 1.1×10^{-4} [m/s], the following can be deduced:

1. Thermal dispersion in horizontal tests is larger than in vertical tests. Usually, only vertical test set-ups are utilized and this might explain why, within the Darcy velocity range of this test set-up, little or negligible thermal dispersion is observed in many experimental investigations in literature (see for example Rau et al., 2012).
2. Thermal dispersion, for both hot and cold injection, increases with increasing ΔH, and hence with fluid velocity. This observation is in

agreement with that of Rau et al. (2012) and Lu et al. (2009) for hot injection.

3. In horizontal tests, thermal dispersion in hot injection cases is more pronounced than in cold injection cases. To the best knowledge of the author, this is rarely treated in the literature. This observation can be useful for the design of low-enthalpy geothermal reservoirs, mainly in deciding whether to include thermal dispersion or not. In Section 4.3, this issue is discussed.
4. In horizontal tests, thermal dispersion is anisotropic and depends on the injection temperature. For hot injection the longitudinal dispersion is dominant, and for cold injection the transversal dispersion is dominant.

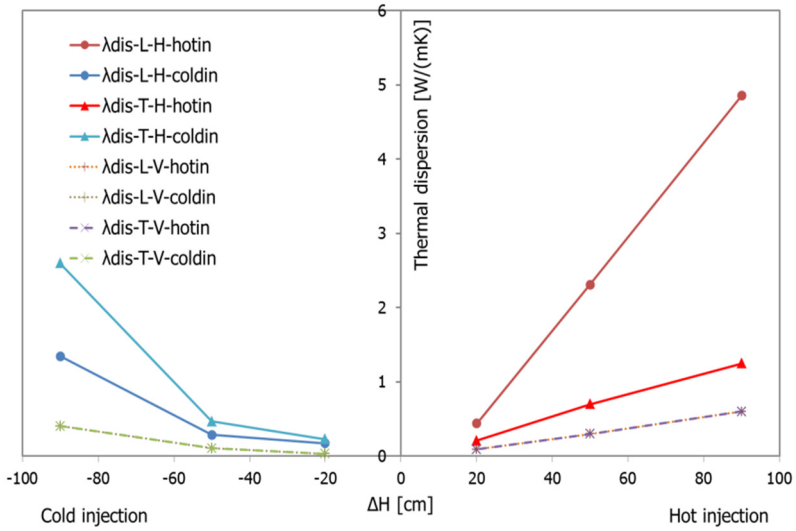

Figure 4-4. Backcalculated thermal dispersion. L: longitudinal, T: transversal, H: horizontal test, and V: vertical test

α_L and α_T are introduced as constants for a specific porous medium (Bear and Cheng, 2010). However, the horizontal experiments results (Figure 4-4) which obtained by using Eq.(4.27) does not show constant α_L and α_T. Therefore, in this work a coefficient related to the fluid viscosity was added to Eq.(4.27) to keep α_L and α_T constant. This will be explained in the next section. On the other hand, thermal dispersion obtained from vertical tests, Figure 4-4, has led, for the range of test velocities considered, to constant α_L and α_T.

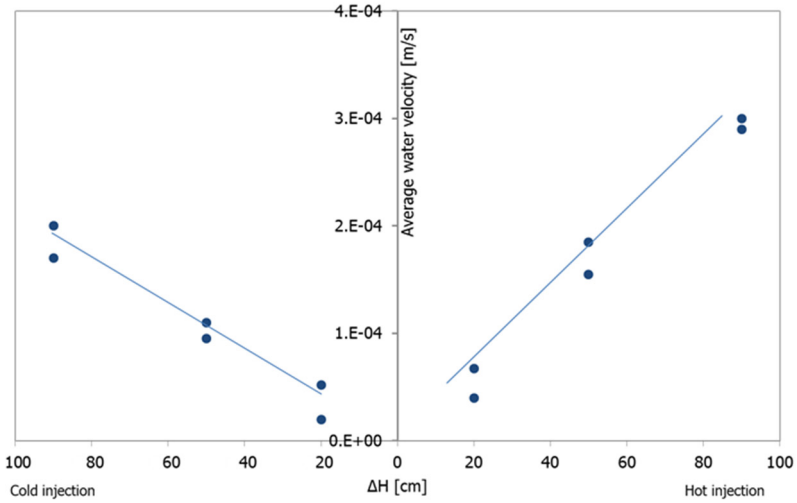

Figure 4-5. Average water velocity for different *ΔH*

4.2.4 Thermal dispersion model

Having quantified the amount of thermal dispersion and α_L and α_T for different fluid velocity and viscosity, a thermal dispersion model suitable for low-enthalpy hydrothermal conditions is developed. The model is derived based on the Bear and Cheng (2009) model for solute dispersion and the Smith and Chapman (1983) model for thermal dispersion, but modified to include density and viscosity effects, and also the opposite nature of longitudinal and transversal thermal dispersion in hot and cold injection conditions, see Figure 4-4. It is proposed that:

$$\lambda_{dis,xx} = \frac{\rho_f c_f}{v}(A_L v_x^2 + A_T v_y^2)$$

$$\lambda_{dis,yy} = \frac{\rho_f c_f}{v}(A_T v_x^2 + A_L v_y^2) \tag{4.28}$$

$$\lambda_{dis,xy} = \lambda_{dis,yx} = \rho_f c_f v\left((A_L - A_T)\frac{v_x v_y}{v^2}\right)$$

where A_L and A_T are the thermal dispersion coefficients in the longitudinal and transversal directions, respectively, and v_x and v_y are the Darcy velocities in

the *x* and *y*-directions. In the Bear and Cheng model, the constants, α_L and α_T, represent characteristic lengths, namely the pore size. Here, A_L and A_T are functions of the fluid viscosity and temperature, such that

$$A_L = M_L e^{+\theta T}$$
$$A_T = M_T e^{-\theta T} \tag{4.29}$$

in which M_L and M_T are

$$M_L = \frac{\mu_0}{B}\alpha_L$$
$$M_T = \frac{B}{\mu_0}\alpha_T \tag{4.30}$$

where B is the fluid viscosity at T = 0 [°C] and θ [1/°C] is a fluid parameter describing the shape of the μ-T curve (see Figure 3-8-A), α_L and α_T are material constants and μ_0 is the initial fluid viscosity. The reciprocating form in Eq.(4.30) is present because the experimental results have shown that, in hot injection, the longitudinal thermal dispersion is dominant, while in cold injection, the transversal thermal dispersion is dominant. Figure 4-4 shows this reciprocating nature of the thermal dispersion coefficients during hot and cold injection**.**

The thermal dispersion model, Eqs. (4.28)-(4.30), was implemented in COMSOL, and all experiments have been simulated once again to study the capability of this model and to quantify the effect of thermal dispersion on the heat flow. Backcalculations were conducted again using these equations, giving $\alpha_L \approx 0.003$ m and $\alpha_T \approx 0.001$ m. For comparison, the dispersion model, Eq.(4.20), introduced by Rau et al. (2012) was also implemented in COMSOL.

Figure 4-6 shows a comparison between the breakthrough curves obtained from three numerical analyses at point C12 (see Figure 3-4), together with the experimental results for horizontal hot injection (Figure 4-6-A) and cold injection (Figure 4-6-B). The numerical analyses were carried out first, without dispersion second, with the proposed dispersion model, and third, with the Rau model.

As expected, the curve with no thermal dispersion exhibits the highest mismatch. Rau's model exhibits a better match to both the hot and cold injection tests(Figure 4-6-C & D), but performs better for hot injection

(Figure 4-6-C). The proposed model exhibits the best fit to both hot and cold injection tests.

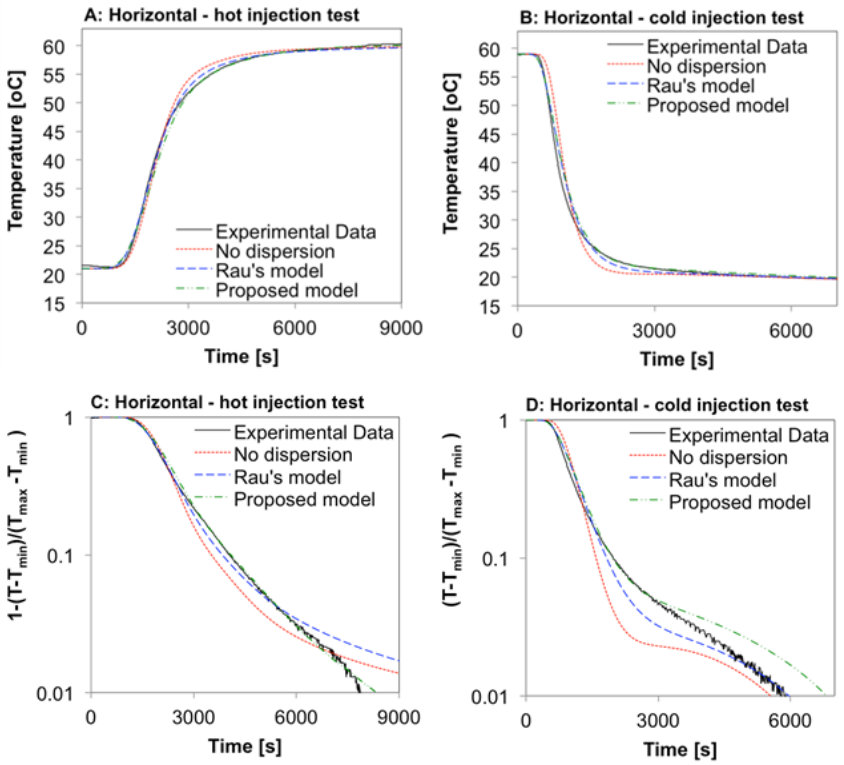

Figure 4-6. Experimental breakthrough curves vs. numerical results of no dispersion model and those obtained from Rau et al.'s (2012) model and the proposed model.

Results obtained from the horizontal and vertical tests are in agreement with Mori et al. (2005), who asserted that, for vertical hot injection tests, for a velocity range of 0.01-50 [m/day], thermal dispersion is small and almost constant, but for the horizontal hot injection tests, thermal dispersion is higher. The vertical hot injection test results are also in agreement with Rau et al. (2012), and exhibit, within the studied fluid velocity range, a relatively small thermal dispersion.

The normalized breakthrough curves for these cases are also shown in Figure 4-6 (C and D). For the hot injection test the proposed method reveals excellent agreement with the experimental results; better than two other models. The agreement for the cold injection is also good. Note that the uncertainty in controlling the heat loss during the cold injection was higher,

and that therefore the experimental breakthrough curve for the cold injection should have had a longer tail. The results of Rau et al.'s (2012) model show slightly larger differences than those obtained by the proposed model, but both are better than the results of the model with no dispersion.

4.3 An up-scaled model

In order to study the effect of dispersion and fluid density and viscosity variations on heat flow during hot and cold injection, for a simple low-enthalpy geothermal system, an up-scaled 2D (horizontal) model representing a porous medium of fully saturated sand, subjected to different flow rates and injection scenarios was simulated. Several finite element simulations were conducted. A physical system consisting of a soil mass (15 [m] × 8 [m]) with a doublet (10 [m] spacing) was simulated, Figure 4-7.

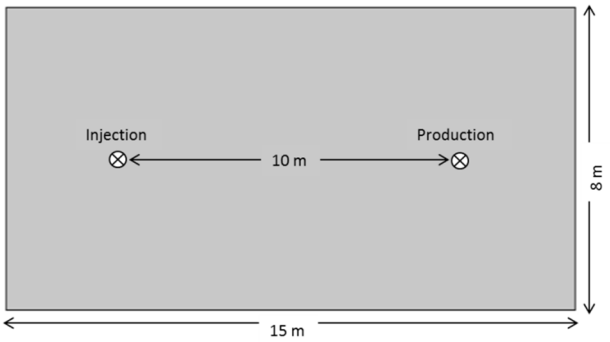

Figure 4-7. Up-scaled model with injection-production wells

The initial temperature in the domain is 20 [^{o}C] for hot injection and 60 [^{o}C] for cold injection, and the temperature difference between the injection and production water is kept at 40 [°C]. Other thermal and hydromechanical parameters are the same as in Table 4-1.

Density and viscosity effect

In this example the focus is placed on the effect of fluid density and viscosity on heat flow and their influence on the system lifetime.

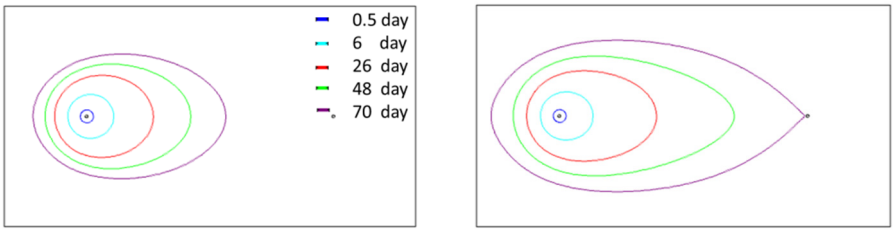

Figure 4-8. Contour lines of 50 °C for hot injection case. Left: density and viscosity are constant. Right: density and viscosity are functions of temperature

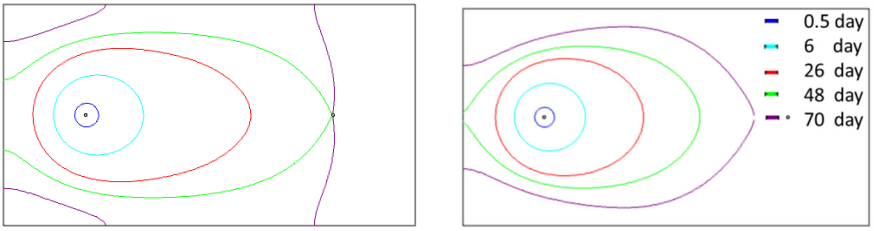

Figure 4-9. Contour lines of 30 °C for cold injection case. Left: density and viscosity are constant. Right: density and viscosity are functions of temperature

Figure 4-8 and Figure 4-9 show the computational results at different times. The figures on the left-hand side present the thermal front position for constant fluid density and viscosity, and the figures on the right-hand side present the thermal front position for temperature dependent density and viscosity (and hence hydraulic conductivity). Studying these figures, the following can be deduced:

Hot injection: The lifetime of the geothermal system will be overestimated if the density and viscosity variation with temperature are not considered.

Cold injection: The lifetime of the geothermal system will be underestimated if the density and viscosity variation with temperature are not considered. Due to the dependency of the hydraulic conductivity on fluid viscosity, cold water moves faster in hot media compared to hot water in cold media.

Figure 4-10 shows breakthrough curves for the above two mentioned cases. For hot injection, considering temperature dependent density and viscosity, the lifetime is 1.4 times less than that for constant density and viscosity. For cold injection, the opposite takes place, i.e. the lifetime for temperature dependent density and viscosity increases by about 1.7 times.

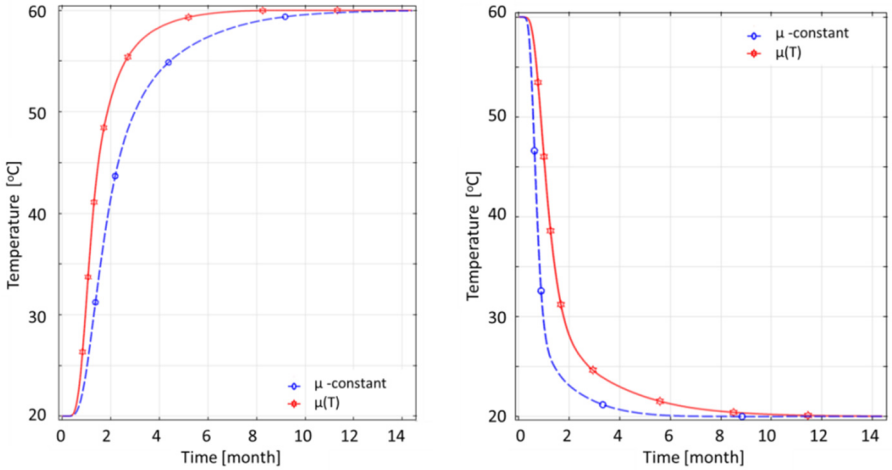

Figure 4-10. Breakthrough curves at the production well. Left: hot injection, Right: cold injection

Thermal dispersion effect

Here the focus is on the effect of thermal dispersion on heat flow and its influence on the geothermal system lifetime. The up-scaled geothermal system described above was simulated. Finite element calculations with different dispersion coefficients (α_L and α_T) were conducted; α_L between 0.003 m and 0.3 m, and α_T between 0.001 m and 0.1 m were simulated. Eq.(4.28) was utilized to describe the thermal dispersion in the system. The comparison between the computational results are made based on an average error defined as

$$\text{error} = \frac{\sum_{i=1}^{n} \frac{\left|T_{n(i)} - T_{d(i)}\right|}{T_{d(i)}}}{n} \tag{4.31}$$

in which $T_{n(i)}$ corresponds to the numerical results without dispersion, $T_{d(i)}$ corresponds to the numerical results with dispersion and n is the number of time steps. Figure 4-11 shows this error for cold and hot injection, for different Darcy velocities. The figure clearly shows that, with increasing dispersivity, a larger error occurs. This is in agreement with the work presented by Molina-Giraldo et al. (2011). Furthermore, for a higher Darcy velocity, a larger error is

realized. For the range of Darcy velocities usually existing in low-enthalpy geothermal systems (q >1×10^{-6} [m/s]), the effect of thermal dispersion is notable.

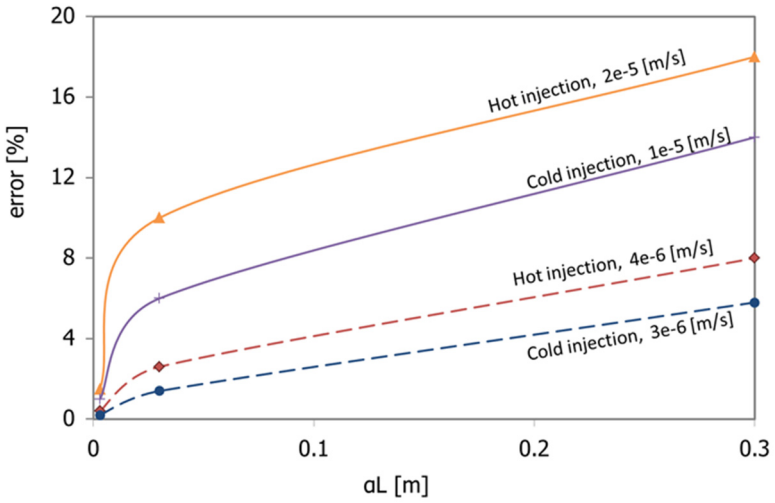

Figure 4-11. Error function, Eq. (4.31), vs. longitudinal thermal dispersion and Darcy velocity.

4.4 Conclusion

To quantify the effect of density, viscosity and thermal dispersion on heat flow, all experiments (explained in Chapter 3) have been simulated using the finite element package COMSOL. A backcalculation study comparing the numerical to the experimental results was conducted. The backcalculation results revealed that, within the range of the studied Darcy velocity (7×10^{-6} [m/s] - 1.1×10^{-4} [m/s]), thermal dispersion in the vertical tests was very small and increases linearly with fluid velocity; but thermal dispersion in the horizontal experiments was more significant and increases nonlinearly with fluid velocity. Furthermore, thermal dispersion in horizontal experiments exhibited different behavior in the hot scenario than in the cold injection scenario. In the horizontal hot injection scenario, the longitudinal dispersion was more significant than the transversal dispersion. On the contrary, in the horizontal cold injection scenario, the transversal thermal dispersion was more significant.

Based on the backcalculation results, a thermal dispersion constitutive model was developed. This model is a function of flow rate, density, viscosity and

pore geometry. It is capable of describing longitudinal and transversal thermal dispersion in a porous domain, taking into consideration the opposite behavior of thermal dispersion observed during hot and cold injection scenarios.

To simulate low-enthalpy geothermal conditions, an up-scaled model representing a porous medium (15 [m] × 8 [m]) of fully saturated sand, subjected to different flow rates and injection scenarios was simulated. Both, density and viscosity effects, together with thermal dispersion, were studied. The up-scaled numerical study on density and viscosity variations with temperature reveals that ignoring these effects leads, in hot injection scenarios, to overestimation of the geothermal system lifetime, and in cold injection scenarios, to underestimation of the system lifetime.

The up-scaled numerical study also reveals that, for Darcy velocities lower than 5×10^{-6} [m/s], thermal dispersion in both hot injection and cold injection scenarios, for a range of thermal dispersion coefficients of 0.003 [m]$<\alpha_L<$0.3 [m] and 0.001 [m]$<\alpha_T<$0.1 [m], is small. For higher Darcy velocity ranges, however, the effect of thermal dispersion within these ranges is more pronounced. Hence, it is important to consider thermal dispersion in the design of low-enthalpy geothermal systems.

Chapter 5

Wellbore-reservoir computational model

In this chapter, a computationally efficient finite element model for transient heat and fluid flow in a deep low-enthalpy geothermal system has been formulated. Emphasis is placed on coupling between the involved wellbores and a soil mass, represented by a geothermal reservoir and surrounding soil. The finite element package COMSOL has been utilized as a framework for implementing the model. In this model, thermal interactions between the wellbore components are included in the mathematical model, alleviating the need for typical 3D spatial discretization, and thus reducing the mesh size significantly.

This chapter is based on the paper "An efficient computational model for deep low-enthalpy geothermal systems" published in the Computers and Geosciences Journal (Saeid et al., 2013).

5.1 Introduction

Geothermal energy is being increasingly utilized for a wide range of applications, including heating and electricity generation (Bakos, 2007). It offers a number of advantages over conventional fossil-fuel resources. Particularly, it is renewable, sustainable, economic, and its environmental

impact in terms of CO_2 emissions is significantly lower. Geothermal systems with high-enthalpy and low-enthalpy are in use. The first is mostly utilized for electricity generation, and the second for residential heating and greenhouses (Gupta and Roy, 2006).

To obtain a highly productive low-enthalpy geothermal system, the reservoir should be able to maintain a desired temperature range and a sufficient flow rate. Heat flow in such a system is dominated by convection and conduction in the geothermal reservoir and along the wellbores. Thermal interaction between the reservoir, the wellbores and the surrounding soil mass is an important factor that needs to be considered, as it affects heat flow in the system, and hence influences heat production.

To achieve an efficient design, it is essential to obtain computational tools capable of modelling heat flow and thermal interactions between the reservoir, the wellbores and the surrounding soil mass. Importantly, the computational tool must be efficient, such that it can be utilized in engineering practice. Currently, several models have been developed to simulate heat flow in geothermal reservoirs and wellbores. Different computational tools are available. They can be divided into two categories: reservoir simulators, and wellbore simulators. TOUGH and its derivatives (Battistelli et al., 1997; Kiryukhin, 1996), Eclipse (Brouwer, et al., 2005), and FEFLOW (Blocher et al., 2010), among others, have been widely utilized for geothermal reservoir simulation. On the other hand, HOLA (Bjornsson and Bodvarsson, 1987; Kiryukhin and Yampolsky., 2004), and WELLSIM (Gunn and Freeston, 1991; Gunn et al., 1992), among others, are widely utilized wellbore simulators. Most of the existing wellbore simulators are capable of solving mass and energy conservation equations for geothermal fluid flow in wellbores. Reservoir and wellbore simulators have been coupled to simulate integrated reservoir-wellbore geothermal systems. Hadgu et al. (1995) coupled the wellbore simulator WFSA and the reservoir simulator TOUGH to model geothermal brine in wells and reservoir. Bhat et al. (2005) utilized HOLA and TOUGH2 to couple wellbores and reservoir heat and fluid flow. Recently, Gudmundsdottir et al. (2012) designed a 1D steady-state wellbore model, FloWell, which will be, according to the authors, coupled to the reservoir model TOUGH2.

In developing numerical tools for geothermal systems, important efforts are devoted to tackling the discretization of two main issues: geometry and heat convection. Deep geothermal systems consist of very slender wellbores embedded in a vast soil mass. This geometrical peculiarity exerts an enormous

computational burden, as a combination of very fine elements (or cells) and coarse elements (or cells) is normally needed to discretize the physical domain. For three-dimensional systems, this normally requires hundreds of thousands to millions of elements, making the CPU time unrealistic for engineering practice. This problem gets even more complicated in the presence of convection and groundwater flow. Governing equations for cases with relatively high Peclet numbers behave like hyperbolic functions, which require fine meshes (grids) and proper upwind schemes to reduce the numerical oscillation that probably occur in such cases. Different solutions have been proposed in literature for tacking these problems. Here, the author employs the numerical model proposed by Al-Khoury and Bonnier (2006) for modelling borehole heat exchangers for shallow geothermal systems, and tailors it for the case of heat flow in deep low-enthalpy geothermal wellbores. This model is a pseudo 3D simulation of a wellbore using 1D elements. This kind of dimensional reduction spares significant numbers of finite elements, and makes the numerical analysis of a coupled reservoir-wellbore system feasible. In this work, the mass balance in the wellbore is not taken into consideration; only the energy balance.

The finite element package COMSOL is utilized as a framework for implementing the proposed model and making the coupling between the wellbore and the soil mass. The thermal interaction between the wellbore, the surrounding soil mass and the reservoir is calculated simultaneously, and each of them is considered as a heat source/sink to the other one, located at the contact boundary between them. Heat flow in the surrounding soil mass is modelled as linear conductive, and in the reservoir it is modelled as nonlinear conductive-convective, due to fluid density and viscosity dependency on temperature.

5.2 Model formulation

The physical domain of the geothermal system is decomposed into two domains: a soil mass, representing a reservoir and surrounding soil, and two wellbores, representing an injection borehole and a production borehole. In this section, the governing heat equations of both domains are derived, together with the initial and boundary conditions.

5.2.1 Governing equations of the soil mass

5.2.1.1 *Soil heat and fluid flow equations*

Heat flow in a deep low-enthalpy geothermal system arises from thermal interactions between the injected fluid, the initial reservoir fluid, and the surrounding soil mass. In a homogeneous one-phase soil mass, constituting a solid skeleton, heat is merely conductive, while in the presence of groundwater flow, the soil mass constitutes a two-phase porous medium; heat flow in this case is conductive-convective. In a typical low-enthalpy geothermal system, the fluid flow plays a major role in carrying the heat from the injection well to the production well, Figure 5-1. The temperature distribution in such a system normally varies between 20 [°C] and 80 [°C]. This relatively high range of temperatures in the reservoir inevitably affects the formation fluid density and viscosity, and hence the heat flow rate and pattern. Therefore, it is vital to consider the fluid density and viscosity as functions of temperature.

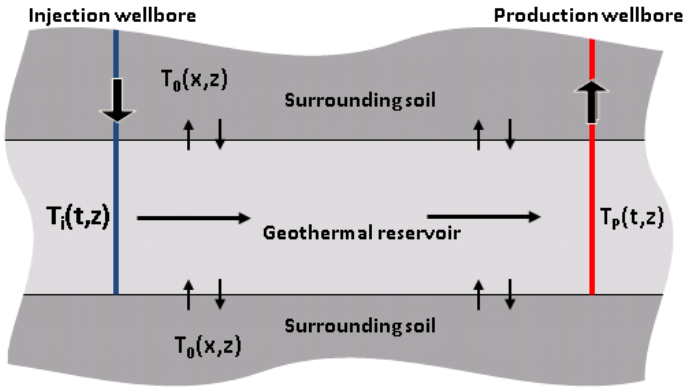

Figure 5-1. A schematic representation of a geothermal reservoir and its interaction with wellbores and surrounding soil

Heat flow in solid and fluid

In a rigid (non-deforming) fully saturated medium, the macroscopic energy balance equation for the solid phase can be described, using Fourier's law, as

$$\frac{\partial}{\partial t}\left[(1-\phi)\rho_s c_s T_s\right]-(1-\phi)\nabla\cdot(\boldsymbol{\lambda}_s\nabla T_s)=0 \qquad (5.1)$$

and for the fluid phase, as

$$\frac{\partial}{\partial t}(\phi\rho_f c_f T_f)+\nabla\cdot(\rho_f c_f\,\mathbf{q}T_f)-\phi\nabla\cdot(\boldsymbol{\lambda}_f\,\nabla T_f)=0 \tag{5.2}$$

where T_s [K] and T_f [K] are the solid and fluid temperatures, respectively, ϕ is the porosity, ρ is the mass density [kg/m^3], c [J/kg.K] is the specific heat capacity, $\boldsymbol{\lambda}$ [W/m.K] is the thermal conductivity, and $\mathbf{q}$ [m/s] is the Darcy velocity (considered anisotropic along the principal axis). The suffix *f refers* to the pore fluid and *s* to the solid matrix.

Working at the macroscopic level, it is reasonable to assume that the phases of a geothermal system are locally in a state of thermal equilibrium. Setting $T_s = T_f = T$, and adding Eqs.(5.1) and (5.2), the energy balance equation for a saturated porous medium can be described as

$$\frac{\partial}{\partial t}(\rho cT)+\nabla\cdot(\rho_f\,c_f\,\mathbf{q}T)-\nabla\cdot(\boldsymbol{\lambda}\nabla T)=0 \tag{5.3}$$

where the thermal conductivity and volumetric heat capacity are described in terms of a local volume average, as

$$\begin{aligned}\boldsymbol{\lambda}&=(1-\phi)\boldsymbol{\lambda}_s+\phi\boldsymbol{\lambda}_f\\ \rho c&=(1-\phi)\rho_s\,c_s+\phi\rho_f\,c_f\end{aligned} \tag{5.4}$$

For a two-phase medium, the velocity of the thermal field is slower than the velocity of the fluid field, defined by a retardation factor related to the ratio between the solid volumetric heat capacity and that of the fluid. By replacing the Darcy velocity $\mathbf{q}$ by the averaged fluid velocity, $\mathbf{v}=\mathbf{q}/\phi$, Eq. (5.3), for heat flow in the surrounding soil mass with constant fluid density, can be re-written as

$$\frac{\partial T}{\partial t}=-R_d\,\mathbf{v}\cdot\nabla T+\mathbf{D}\nabla^2 T \tag{5.5}$$

where

$$R_d=\frac{\phi\rho_f c_f}{(1-\phi)\rho_s c_s+\phi\rho_f c_f} \tag{5.6}$$

and

$$\mathbf{D} = \frac{\boldsymbol{\lambda}}{\rho c} \tag{5.7}$$

is the thermal diffusivity [m^2s^{-1}]. In the absence of groundwater flow, Eq.(5.5) becomes

$$\rho_s c_s \frac{\partial T}{\partial t} + \nabla.(-\boldsymbol{\lambda}_s \nabla T) = 0 \tag{5.8}$$

In the reservoir, the fluid density is assumed to be a function of the temperature, as described later in this chapter.

Fluid flow

The fluid flow in the reservoir can be expressed as

$$\phi \frac{\partial \rho_f}{\partial t} + \nabla.(\rho_f \mathbf{q}) = 0 \tag{5.9}$$

where **q** is the Darcy flow velocity, described, for a single phase flow, as

$$\mathbf{q} = -\frac{\boldsymbol{\kappa}}{\mu}(\nabla P - \rho_f \mathbf{g} \nabla z) \tag{5.10}$$

in which $\boldsymbol{\kappa}$ is the intrinsic permeability [m^2] of the porous medium, μ [Pa.s] is the fluid dynamic viscosity, **g** [m/s^2] is the gravity vector, and *P* is the hydraulic pressure. The intrinsic permeability is a property of the solid material, describing its ability to conduct water. In practice, the hydraulic conductivity is often used, defined as

$$\mathbf{K} = \boldsymbol{\kappa}\, \mathbf{g} \frac{\rho_f}{\mu} \tag{5.11}$$

Density and viscosity dependency on temperature

The variation of fluid density and viscosity with temperature, and other state variables, can be described by the equation of state of the specific fluid. In multiphase flow, the density is regarded as a function of temperature (*T*), pressure (*P*), and concentration (ω), as

$$\rho_f = \rho_f(T, P, \omega) \tag{5.12}$$

The total differential of Eq. 12 yields (Diersch and Kolditz, 2002)

$$\frac{1}{\rho_f}\partial\rho_f = \underbrace{\left(\frac{1}{\rho_f}\frac{\partial\rho_f}{\partial T}\right)}_{-\beta}\partial T + \underbrace{\left(\frac{1}{\rho_f}\frac{\partial\rho_f}{\partial P}\right)}_{\gamma}\partial P + \underbrace{\left(\frac{1}{\rho_f}\frac{\partial\rho_f}{\partial C}\right)}_{\alpha}\partial C \tag{5.13}$$

where the term β is the fluid thermal expansion, γ is fluid compressibility, and α is the volumetric solubility. Assuming α, β and γ are constants, integration of Eq. (4.13) leads to the equation of state of the fluid density, of the form:

$$\rho_f = \rho_{f0}\, e^{-\beta(T-T_0)+\gamma(P-P_0)+\alpha(C-C_0)} \tag{5.14}$$

in which ρ_{f0} is the initial density of the fluid at an initial temperature, T_0 , an initial pressure, P_0 , and an initial concentration,C_0.

This equation can be approximated linearly as (Diersch and Kolditz, 2002)

$$\rho_f = \rho_{f_0}(1-\beta(T-T_0)+\gamma(P-P_0)+\alpha(C-C_0)) \tag{5.15}$$

For a low-enthalpy geothermal system, the density variation with pressure and concentration is negligible, and hence the equation of state of the formation fluid may be described as

$$\rho_f = \rho_{f_0} e^{-\beta(T-T_0)} \tag{5.16}$$

The viscosity can be treated in the same way, yielding

$$\mu = \mu_0\, e^{-\beta(T-T_0)} \tag{5.17}$$

5.2.1.2 *Soil initial and boundary conditions*

For fluid flow, the initial and boundary conditions are often associated with a pressure difference between the injection and production wells. Initially, at time $t = 0$, the pressure is hydrostatic. Upon operating the geothermal system, the hydraulic boundary conditions may be described as

$$\begin{aligned} &P(x_{\text{inj}}, y_{\text{inj}}, z_{\text{inj}}) = P_1, && \text{at the injection well location} \\ &P(x_{\text{pro}}, y_{\text{pro}}, z_{\text{pro}}) = P_2, && \text{at the production well location} \end{aligned} \tag{5.18}$$

For heat flow, the initial condition of the soil mass, at time t = 0, is defined as the steady-state condition

$$T(x, y, z, 0) = T_0(x, y, z) \tag{5.19}$$

At the reservoir inlet, the boundary condition is:

$$T(x_{\text{inj}}, y_{\text{inj}}, z_{\text{inj}}, t) = T_{ip}(x_{\text{inj}}, y_{\text{inj}}, z_{\text{inj}}, t) \tag{5.20}$$

where T_{ip} is the temperature of the injection well in-contact with the reservoir.

5.2.2 Governing equations of the wellbore

5.2.2.1 *Wellbore heat equations*

Heat transfer in a wellbore is conductive-convective and arises from the flow of a working fluid running through an inner pipe, and the thermal interaction between the wellbore components and the surrounding soil mass. A wellbore is a highly slender cylinder consisting of an inner pipe carrying the fluid, surrounded by a cemented grout that is in contact with the soil mass, Figure 5-2. Such geometry exhibits a unique and challenging numerical problem. If a standard 3D finite element (finite volume or finite difference) formulation is utilized to model heat flow in the wellbore and the surrounding soil mass, meshes with an enormous number of finite elements will be needed, resulting in unrealistic CPU times.

To decrease the computational demands on geometrical discretization, Al-Khoury et al. (2005) proposed a pseudo 3D borehole model for shallow geothermal systems, capable of simulating heat flow in a multicomponent domain using a 1D line element. Despite this reduction in the pipe dimensions, preservation is made of the actual heat distribution in the wellbore components and their interactions. Hence, preservation is made of the involved physical and thermal properties of the pipe components, such as: the cross sectional areas; the thermal conductivities of the grout and the inner pipe materials; the fluid thermal properties and flow rate; and the properties of the contact surface with the surrounding soil. The 1D representation, however, implies that the variation of the temperature is along its axis, and that no temperature variation exists in its radial direction. The latter condition is reasonably valid because of the slenderness of the wellbore, where the radial variation of temperature is negligible. Nevertheless, heat fluxes normal

to the contact surfaces along the vertical axis are fully considered, and included explicitly in the mathematical model.

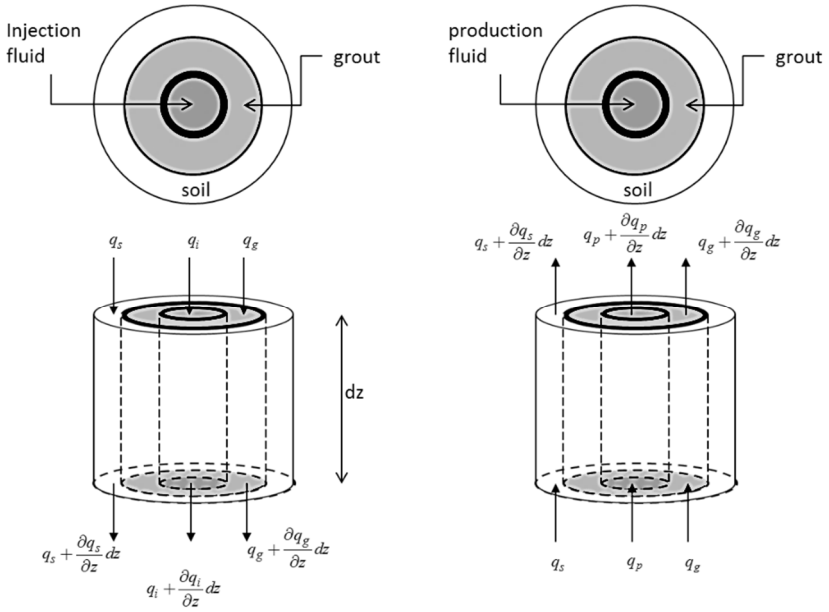

Figure 5-2. A cross-section and a control volume for: injection well (left) and production well (right)

In this work, this model is adopted and tailored to describe heat flow in wellbores typically utilized in deep low-enthalpy geothermal systems. The corresponding heat equations can be derived from the law of conservation of energy and Fourier's law of a multicomponent domain (Al-Khoury, 2012). Consider a wellbore with a control volume of length *dz*, consisting of coaxial well components: wellbore pipe, denoted for the injection well as *i* and for the production well as *p*; grout, denoted as *g*; and soil, denoted as *s*, and heat flux denoted as *q*, Figure 5-2. The pipe components transfer heat across their volumes (*V*), and exchange fluxes across their surface (*S*) areas. For a transient condition, equating the rate of energy entering the control volume to the rate of energy leaving it, the net heat flow into each of the pipe components can be expressed as follows:

Injection wellbore,

$$\rho_f c_f \frac{\partial T_i}{\partial t} dV_i - \lambda_f \frac{\partial^2 T_i}{\partial z^2} dV_i + \rho_f c_f u_i \frac{\partial T_i}{\partial z} = b_{ig}(T_i - T_g) dS_{ig} \tag{5.21}$$

$$\rho_g c_g \frac{\partial T_g}{\partial t} dV_g - \lambda_g \frac{\partial^2 T_g}{\partial z^2} dV_g = b_{ig}(T_g - T_i) dS_{ig} + b_{sg}(T_g - T_s) dS_{sg} \tag{5.22}$$

$$\rho_s c_s \frac{\partial T_s}{\partial t} dV_s - \lambda_s \frac{\partial^2 T_s}{\partial z^2} dV_s = b_{sg}(T_s - T_g) dS_{sg} \tag{5.23}$$

Production wellbore

$$\rho_f c_f \frac{\partial T_p}{\partial t} dV_p - \lambda_f \frac{\partial^2 T_p}{\partial z^2} dV_p - \rho_f c_f u_p \frac{\partial T_p}{\partial z} = b_{pg}(T_p - T_g) dS_{pg} \tag{5.24}$$

$$\rho_g c_g \frac{\partial T_g}{\partial t} dV_g - \lambda_g \frac{\partial^2 T_g}{\partial z^2} dV_g = b_{pg}(T_g - T_p) dS_{pg} + b_{sg}(T_g - T_s) dS_{sg} \tag{5.25}$$

$$\rho_s c_s \frac{\partial T_s}{\partial t} dV_s - \lambda_s \frac{\partial^2 T_s}{\partial z^2} dV_s = b_{sg}(T_s - T_g) dS_{sg} \tag{5.26}$$

where the subscript *f* represents the geothermal fluid, b_{ig} [W/m^{2}K] is the reciprocal of the thermal resistance between the injection well pipe and the grout, b_{pg} [W/m^{2}K] is the reciprocal of the thermal resistance between the production well pipe and the grout, and b_{sg} [W/m^{2}K] is the reciprocal of the contact resistance between the gout and the soil. dS_{ig} is the contact surface area between the injection well pipe and the grout, etc. Other parameters are similar to those described earlier.

This formulation emphasizes that, as manifested physically, the thermal interaction between the wellbore components occurs via the grout, which works as an intermediate medium, transferring heat from the well pipe to the soil and vice versa. It is important to note that the inclusion of the thermal interactions described on the right-hand side in the mathematical model, Eqs. (5.21) to (5.26), is crucial. It alleviates the need for three-dimensional finite element spatial discretization of the involved components, and allows for the use of a one-dimensional element. Such a reduction in the spatial

discretization reduces significantly the mesh size, making the computation of such a system feasible.

5.2.2.2 *Heat transfer coefficients*

Heat transfer coefficients can be calculated using three different methods: experimental; analytical or numerical; and analogy to electrical circuits (Al-Khoury, 2012). Here, the analogy to electrical circuits is utilized. Following this, heat transfer coefficients for the injection wellbore pipe - grout can be described as

$$b_{ig} = \frac{1}{R_{ig}} \tag{5.27}$$

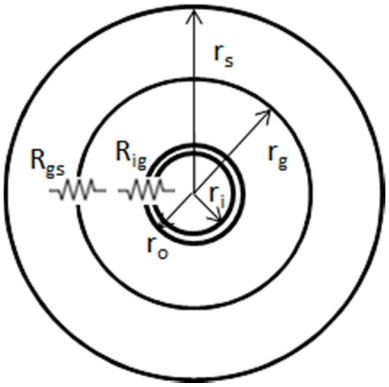

Figure 5-3. A cross-section of the injection wellbore showing its components thermal interactions

where

$$R_{ig} = R_{fluid} + R_{pipe\ material} = \frac{1}{r_o / r_i \,\bar{h}} + \frac{r_o \ln(r_o / r_i)}{\lambda_p} \tag{5.28}$$

is the wellbore pipe - grout thermal resistance, with r_i and r_o being the inner and the outer radius of the wellbore pipe respectively (Figure 5-3), λ_p is the thermal conductivity of the wellbore pipe material, and $\bar{h} = Nu\,\lambda / 2r_i$, where Nu is the Nusselt Number, which can be defined as (Al-Khoury, 2012):

***Laminar flow*:** For fully-developed internal laminar flow in cylindrical tubes, the Nusselt numbers are constant. For convection with constant surface heat flux, the Nusselt number is:

$$Nu = 4.36 \tag{5.29}$$

For convection with constant surface temperature, the Nusselt number is:

$$Nu = 3.66 \tag{5.30}$$

***Turbulent flow*:** Gnielinski correlation for turbulent flow in tubes is:

$$Nu = \frac{(f/8)(\mathrm{Re}-1000)\,\mathrm{Pr}}{1+12.7(f/8)^{1/2}(\mathrm{Pr}^{2/3}-1)}\ , \qquad \begin{matrix} 0.5 < \mathrm{Pr} < 200 \\ 3000 < \mathrm{Re} < 5\times 10^6 \end{matrix} \tag{5.31}$$

where *f* is the Darcy friction factor defined, for smooth tubes, as

$$f = (0.79\ln(\mathrm{Re}) - 1.64)^{-2} \tag{5.32}$$

Dittus-Boelter correlation for turbulent flow in tubes is:

$$\mathrm{Nu} = 0.023\,\mathrm{Re}^{4/5}\,\mathrm{Pr}^{n}, \qquad \begin{matrix} 0.7 < \mathrm{Pr} < 160 \\ \mathrm{Re} \geq 10\,000 \\ L/D \geq 10 \end{matrix} \tag{5.33}$$

where n = 0.4 for heating and n = 0.3 for cooling, Pr is the Prandtl number and Re is the Reynolds number defined as $\mathrm{Re} \equiv u D_i/\nu$, where u [m/s] is the average fluid velocity, and $\nu \equiv \mu_m/\rho$ is the kinematic viscosity [m^2/s] in which μ_m [N.s/m^2] is the fluid mass-based viscosity and ρ [kg/m^3] its mass density. In the literature, the motion is usually considered turbulent for $\mathrm{Re} > 2000$. In practice, Eq.(5.33) is used for smooth pipes.

The heat transfer coefficient for grout-soil is described as

$$b_{gs} = \frac{1}{R_{gs}} \tag{5.34}$$

where

$$R_{\mathrm{gs}} = \frac{r_g \ln(r_g / r_{\mathrm{o}})}{\lambda_{\mathrm{g}}} \tag{5.35}$$

in which r_g is the radius of the grout, and r_{o} is the inner radius of the grout, which is equal to the outer radius of wellbore pipe.

5.2.2.3 *Wellbore initial and boundary conditions*

Initially, at t = 0, the temperature in the wellbore is equal to the steady-state temperature in the soil before the system starts operating, i.e.

$$T_i(z,0) = T_p(z,0) = T_g(z,0) = T_s(z,0) \tag{5.36}$$

in which T_s is the soil temperature immediately around the wellbore.

The boundary conditions typically involved in an operating wellbore are of two types: Dirichlet and Neumann. At the injection well, an inlet temperature can be prescribed as

$$T_i(z=0,t) = T_{in}(t) \tag{5.37}$$

At the top of the production well, the heat flux can be set to zero:

$$-\lambda_f \frac{dT_p}{dz} = 0 \tag{5.38}$$

5.3 Finite element implementation: 1D-2D coupling

The finite element package, COMSOL, has been utilized as a framework for implementing the proposed wellbore model, coupled to a geothermal reservoir and surrounding soil mass. The physical model is decomposed into two domains: one representing the soil mass, and the other representing one or more wellbores. The soil mass is simulated as 2D, two-phase (solid and liquid) and fully saturated, to represent the reservoir; and as a single-phase homogeneous solid for the surrounding soil. Each wellbore is simulated as a 1D domain.

Heat flow in the reservoir is described by Eq.(5.3) and in the soil mass surrounding the reservoir it is described by Eq.(5.8). The fluid flow in the reservoir is described by Eq.(5.10). The dependency of density and viscosity

on temperature is taken into consideration according to Eqs.(5.16) and (5.17). Heat flow in the wellbore is described using Eqs.(5.21) to (5.26).

The thermal interaction between the wellbore and the soil mass is calculated simultaneously and the temperatures in the injection and production wellbores, represented by the 1D geometry, are treated as boundary values to the corresponding 2D geometry. Figure 5-4 shows schematically the coupling process. The calculated temperature at the bottom of the injection wellbore (Ti_p, Figure 5-4) is prescribed at the inlet boundary of the reservoir. The calculated temperature at the outlet boundary of the reservoir is averaged and prescribed at the bottom boundary of the production well (To_p in Figure 5-4).

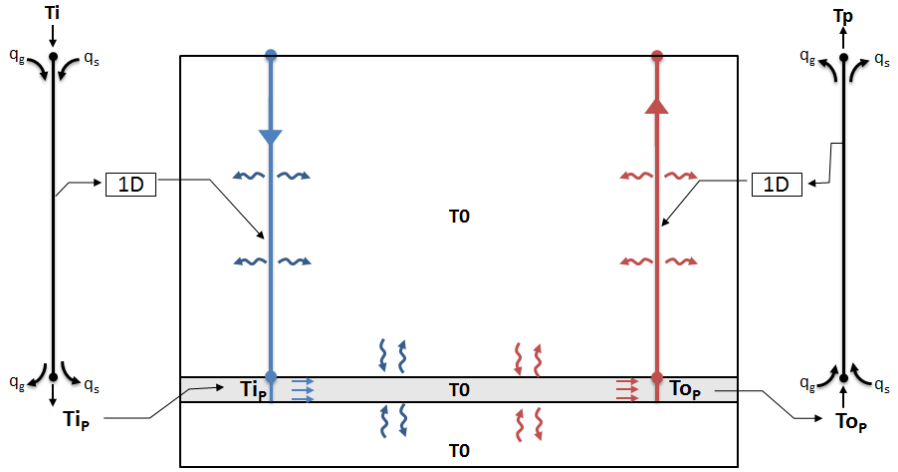

Figure 5-4. 1D-2D coupling in COMSOL

5.4 Numerical examples

In this section, a numerical example and a parametric analysis are presented. The first example shows the computational capability of the model for solving a deep low-enthalpy geothermal doublet at regional level. The parametric example describes the effect of viscosity and porosity on the life time of the geothermal system.

In the following examples, the following assumptions are considered:

- Sand and clay layers are assumed to be homogeneous, isotropic, and horizontal with constant thickness.

- Cap and bed clay layers are impermeable: no convection.
- Heat capacity and thermal conductivity are homogenous and isotopic in all layers.

5.4.1 Deep low-enthalpy geothermal doublet

A region representing a deep low-enthalpy geothermal system of 3300 [m] x 2400 [m] is considered. It consists of a homogeneous geothermal reservoir, located at 2 [km] under the ground surface, and a doublet, representing production and injection wellbores. The wellbores are 2 [km] away from each other and reach 2 [km] in depth. Figure 5-5-left shows the model geometry and the position of the injection and production wells. The thermal and hydrological properties of the geothermal system are shown in Table 5-1.

Table 5-1. Properties of the porous media

Parameter	Symbols	Value	Unit
Reservoir			
Permeability	K	5e-13	m^2
Porosity	ϕ	17	%
Fluid density at 60°C	ρ_f	984.96	$kg.m^{-3}$
Fluid density at 20°C	ρ_f	998.38	$kg.m^{-3}$
Soil (grain) density	ρ_s	2650	$kg.m^{-3}$
Fluid thermal conductivity at 60°C	λ_f	0.67	$W.m^{-1}.K^{-1}$
Soil thermal conductivity	λ_s	2.5	$W.m^{-1}.K^{-1}$
Fluid specific heat capacity at 60°C	c_f	4190	$J.kg^{-1}.K^{-1}$
Soil specific heat capacity	c_s	830	$J.kg^{-1}.K^{-1}$
Surrounding soil			
Soil density	ρ_s	1750	$kg.m^{-3}$
Thermal conductivity	λ_s	2	$W.m^{-1}.K^{-1}$
Specific heat capacity	c_s	2000	$J.kg^{-1}.K^{-1}$

5.4.1.1 *Initial and boundary conditions*

Initially, at t =0, the pore pressure is hydrostatic, and the temperature distribution is assumed to be

$$\begin{aligned} T &= -\alpha(z_0 - z) + T_0 && \text{at } z < 2000\ m \\ T &= T_0 && \text{at } z > 2000\ m \end{aligned} \tag{5.39}$$

in which α [K/m] is the underground thermal gradient, equal to 0.025, and T_0 = 60 [°C] , the known reservoir temperature at depth z_0 = 2000 [m], see Figure 5-5-right.

Upon system operation, the temperature at the top of the injection well is prescribed as

$$T_i(z=0,t) = T_{in}(t) = 20\ ^\circ C \tag{5.40}$$

At the bottom of the production well, the calculated reservoir temperature is averaged and prescribed as

$$T_p(z=2000\,\mathrm{m},t) = \mathrm{avg.}\left[T(x=2650\,\mathrm{m}, z=2000\,\mathrm{m} - z=2100\,\mathrm{m}), t\right] \tag{5.41}$$

A pressure difference of 35 [bar] (3.5 [MPa]) between the two wellbores is imposed, resulting in a fluid flow from the injection well towards the production well.

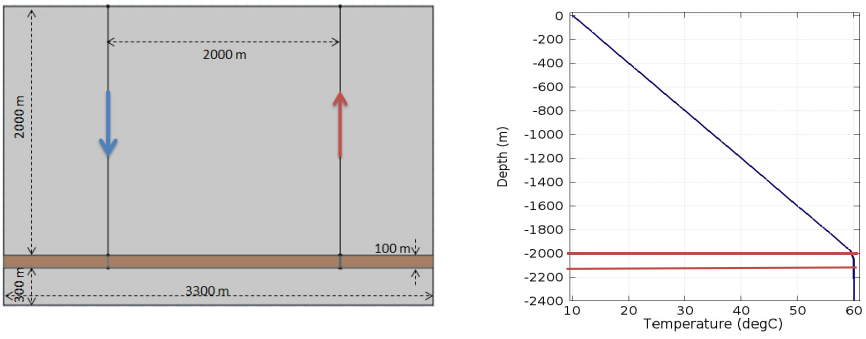

Figure 5-5. Model geometry (left), and initial thermal gradient of the soil mass (right).

5.4.1.2 *Computational results*

A finite element analysis for the calculation of heat flow in the geothermal system, subjected to cold water, T_{in} = 20 [°C], at the top of the injection

wellbore for 60 years is conducted. The finite element mesh is shown in Figure 5-6. The wellbores are discretized using 1D line Galerkin least-square elements, and the soil mass is discretized using 2D triangular- three node elements (COMSOL, 2011). The mesh consists of 6739, 2D elements, for the soil mass, and 50, 1D elements, for each wellbore. Fine elements for the reservoir and its boundaries have been employed because of the non-linearity involved in the density and viscosity of the fluid phase. However, due to the advantages of using the proposed 1D model, relatively coarse elements are utilized for the discretization of the wellbores. The Backward Euler time integration scheme has been utilized for the discretization of time.

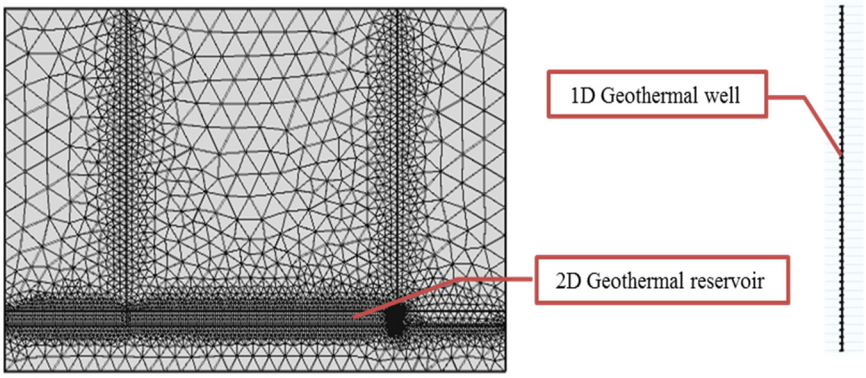

Figure 5-6. Finite element meshes for 2D and 1D domains

The calculated temperature distribution in the geothermal reservoir and its surroundings is shown in Figure 5-7. It shows the cold front movement from the injection well to the production well at different times. The results show the combined effect of the dependency of the water density and viscosity on temperature (Saeid and Barends, 2011). By decreasing the temperature in the reservoir, with the assumption of a constant intrinsic permeability, the hydraulic conductivity ***K*** decreases, see Eq. (4.11). The decrease in hydraulic conductivity causes a gradual slowdown in the cold front velocity. Cold water tends to move downward due to its greater weight (buoyancy effect). Hence, the water velocity is not uniform at any cross section of the reservoir. The underlying cold front is more obvious at later stages of the geothermal system. The figure also shows the influence area around the wellbores due to thermal

interactions (heat loss/gain) between the wellbores and surrounding soil mass.

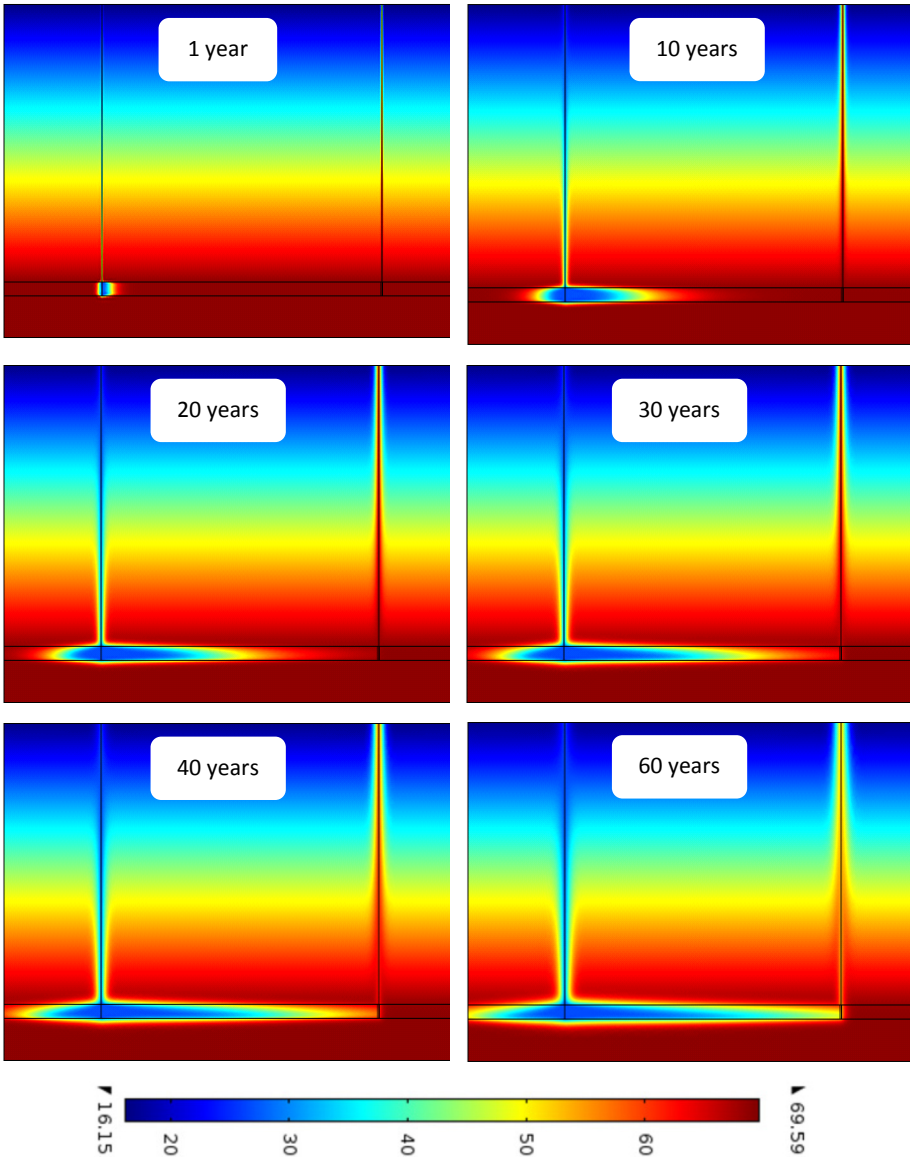

Figure 5-7. Heat flow at different times (temperature unit is degree centigrade)

Figure 5-8 shows the fluid temperature distribution along the wellbores at different times. It can be seen that the temperature variation is pronounced at the early stages of operation, after which the temperature becomes practically constant along the depth of the wellbores. The variation in temperature at the early stage is dominated by the large temperature difference between the initial temperature of the surrounding soil and the fluid.

Figure 5-9 shows the breakthrough curve at the outlet, where a 10 [^{o}C] temperature drop takes place after 40 years of production. Figure 5-10 and Figure 5-11 show the influence area around the injection and production wellbores at various times and depths, respectively. In these figures *x* axis shows the horizontal distance from the well center and the *y* axis shows the temperature at a specified depth. For the injection well, the influence area is relatively small at shallow depths and large at deeper depths, while for the production well, it is the reverse. The horizontal dashed arrows in Figure 5-10 and Figure 5-11 show the influence area after 30 years.

The CPU time for solving this system for 60 years is 49 seconds on a normal Intel 500 MHz, 4GB RAM PC. It is worth mentioning that the proposed model is capable of simulating more complex geology (e.g. lateral heterogeneity or Fault) and wellbore configurations.

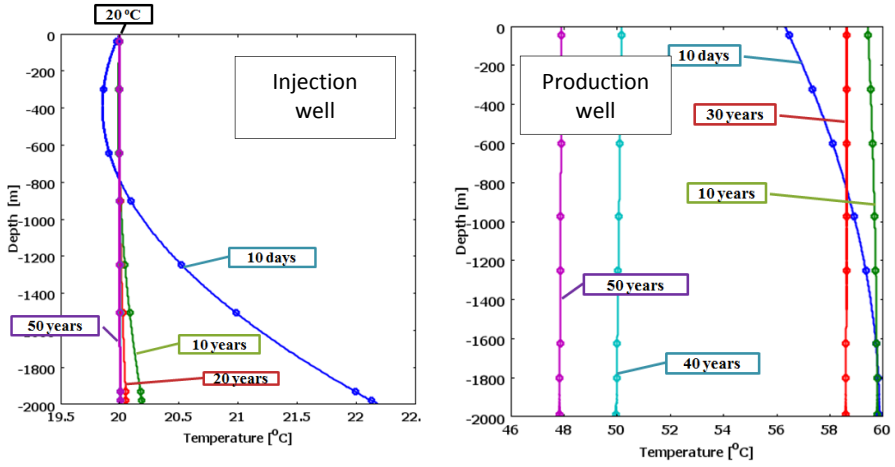

Figure 5-8. Fluid temperature distribution in injection well (left), and production well (right)

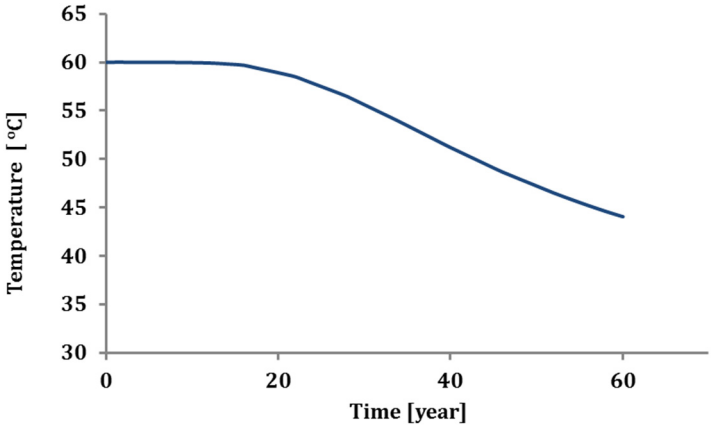

Figure 5-9. Breakthrough curve at the outlet in the reservoir

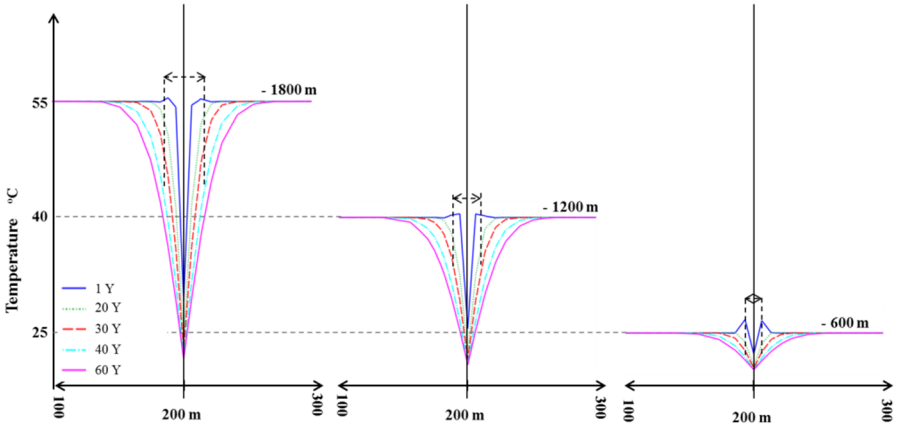

Figure 5-10. Qualitative analysis of influence areas surrounding the injection well at various times and depths. *x* axis shows the horizontal distance from well center.

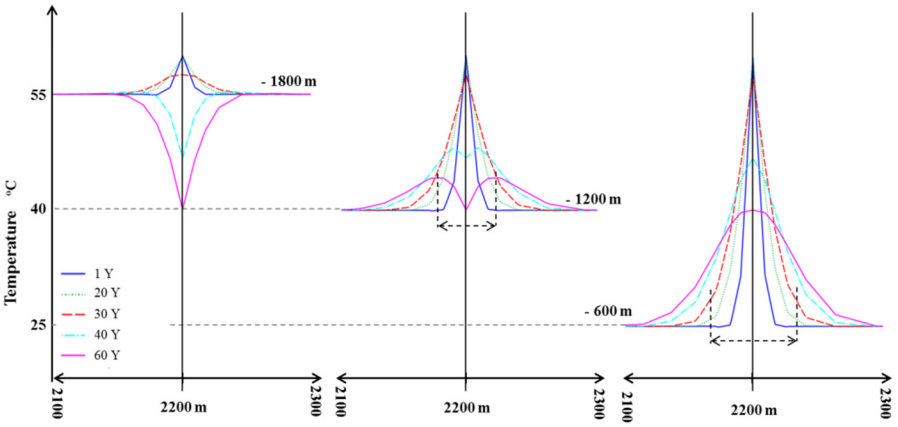

Figure 5-11. Qualitative analysis of influence areas surrounding the production well at various times and depths. *x* axis shows the horizontal distance from well center.

5.4.2 Parametric analysis

In deep low-enthalpy geothermal systems, the uncertainty of some parameters, such as reservoir porosity, has a significant effect on heat production rate and system lifetime. In this section, the effects of viscosity and porosity are evaluated. The previous numerical example is utilized, but with varying parameters.

5.4.2.1 *Viscosity effects*

Here the effect of viscosity on the reservoir lifetime is evaluated. Three different cases were considered: water with constant viscosity (viscosity of water at initial temperature of 60 [^{O}C] is considered), water with temperature dependent viscosity (Lide and David, 1990), and brine (salinity of 80 [gr/l] NaCl) with temperature dependent viscosity (Batzle and Wang, 1992). Figure 5-12 shows the dependency of viscosity of the three fluids with temperature. The life time prediction for the three cases is shown in Figure 5-13. Considering the threshold of 50 [^{o}C], the life time for the first case is about 27 years, for the second case it is about 44 years, and for the third case it is about 55 years.

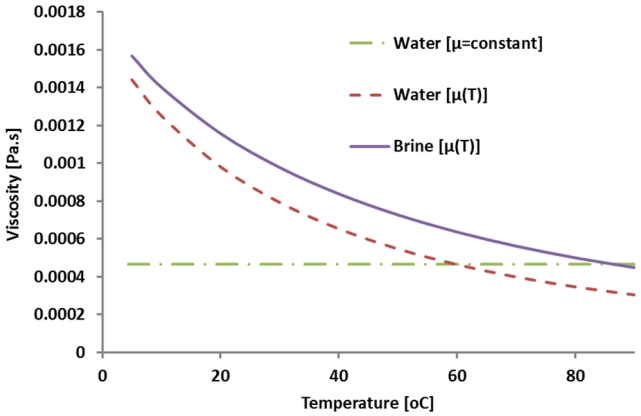

Figure 5-12. Viscosity versus temperature for three different fluids

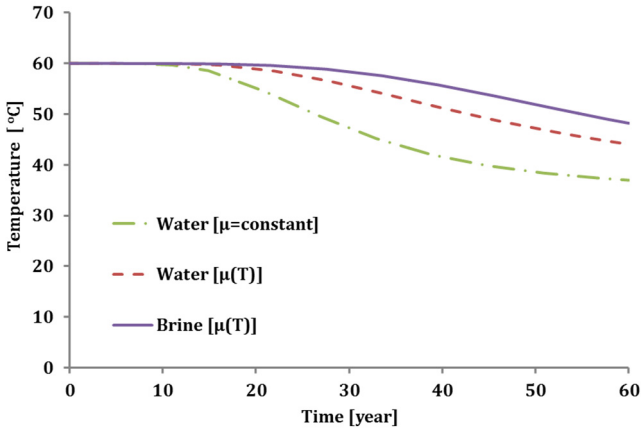

Figure 5-13. Breakthrough curves for cases with different viscosity

Comparison between the first case and the second case reveals that the dependency of viscosity on temperature causes a slowing down of the movement of the cold front. Therefore disregarding this dependency leads to underestimating the lifetime of the geothermal system. In this specific case, disregarding the dependency of viscosity on temperature causes a 37% underestimation of the expected lifetime of the system.

Comparing heat flow in water and in brine reveals that the movement of a cold fluid with higher viscosity is slower than that for the lesser viscosity, and hence, has a longer lifetime.

5.4.2.2 *Effect of porosity*

Figure 5-14 shows the sensitivity of the reservoir lifetime on porosity. It shows that a variation of ±3% in porosity causes a variation of ± 15% in the life time.

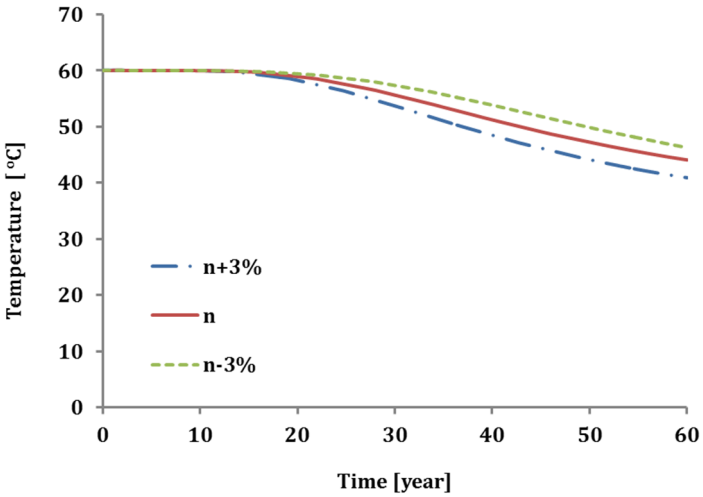

Figure 5-14. Breakthrough curves for cases with different porosity

5.5 Conclusion

In this contribution, a computationally efficient finite element model for transient heat and fluid flow in a deep low-enthalpy geothermal system is formulated. The finite element package COMSOL is utilized as a framework for implementing the model and coupling between the wellbores and the soil mass. This coupling provides a complete overview about heat transfer in all geothermal system constituents; namely the wellbore components, the reservoir and the surrounding soil. Normally, using standard finite element formulations, this kind of coupling is computationally expensive, but here it is made feasible as a result of the utilization of the proposed wellbore pseudo three-dimensional model. In this model, the thermal interaction between the wellbore components and the soil mass is explicitly included in the

mathematical formulation, allowing the reduction of the spatial discretization from 3D to 1D, and making the model highly efficient.

The numerical examples have shown that a deep low-enthalpy geothermal system of about 3 [km] x 2 [km] in dimensions, consisting of two wellbores of 2 [km] in length, can be modelled using 6739 2D elements, for the soil mass, and 50 1D elements, for each wellbore. The CPU time for conducting the calculations for 60 years of operation, using a normal Intel PC (500 MHz, 4GB RAM), is 49 seconds. Obviously such computational requirements are minor compared to typical finite element, finite volume or finite difference requirements, where hundreds of thousands of cells/elements are needed to simulate deep geothermal systems at regional levels.

The parametric examples have shown the sensitivity of geothermal systems to hydrological parameters, namely the viscosity and the porosity. The first parametric example shows that the dependency of viscosity on temperature can affect the lifetime of the system: with higher viscosity, the propagation of the cold front slows down, thus increasing the expected lifetime of the geothermal system. Hence, for the temperature ranges involve in deep low-enthalpy geothermal systems, it is important to model the dependency of viscosity (and also density) on temperature. The second parametric example shows that variation of the porosity can affect the expected lifetime of the system.

As a result of the computational efficiency and accuracy, the proposed model provides the means for more insight into heat flow in deep low-enthalpy geothermal systems that might assist in improving the procedure for wellbore design. Also, the computational efficiency of the wellbore model encourages the extension of the coupling between the wellbores and the soil mass from 1D-2D to 1D-3D.

Chapter 6

A prototype design model for deep low-enthalpy geothermal systems

In this chapter, a prototype design model for low-enthalpy hydrothermal systems has been introduced. The model is developed based on the findings presented in the previous chapters and an extensive parametric analysis based on typical physical and human controlled parameters. The model predicts, empirically, the lifetime of a hydrothermal system as a function of reservoir porosity, discharge rate, well spacing, average initial temperature of the reservoir, and injection temperature. The finite element method is utilized for this purpose. An extensive parametric analysis for a wide range of physical parameters and operational scenarios for typical geometry has been conducted to derive the model. The proposed model can provide geothermal engineers and decision makers with a preliminary conjecture about the lifetime of a deep low-enthalpy hydrothermal system. The proposed modeling technique can be utilized as a base to derive elaborate models that include more parameters and operational scenarios.

This chapter is based on the paper “A prototype design model for deep low-enthalpy hydrothermal systems” published in the Renewable Energy Journal (Saeid et al., 2015).

6.1 Introduction

Geothermal heat is an important potential source of renewable energy that is sustainable and generates minimal CO_2 emissions. Hydrothermal systems (also known as doublets) are the most common method of geothermal energy recovery that utilize two wells, one for hot water production and another for cold water injection. Accurate prediction of both the lifetime and energy production of geothermal doublets is essential for the successful design of such systems (Blöcher et al., 2010).

Significant numbers of studies have identified various factors influencing heat flow in geothermal reservoirs and their lifetime, including: viscosity and density dependence on temperature (Ma and Zheng, 2010; Watanabe et al., 2010; Saeid et al., 2014); porosity and permeability (Mottaghy et al., 2010; Chandrasiri Ekneligoda and Min, 2013; Vogt et al., 2013); geothermal fluid salinity; flow rate (Franco and Vaccaro, 2014); well spacing (Sauty et al., 1980); injection temperature (Bedre and Anderson, 2012) and reservoir geometry (Sippel et al., 2013). These studies qualitatively identified the significance of the examined factors on the lifetime of geothermal systems, but no quantitative models have yet been introduced that combine these factors in a simple mathematical formulation. This chapter focuses on this issue.

The objective of this work is the development of a prototype model capable of estimating the lifetime of hydrothermal systems. The model is suitable for conducting a preliminary design that can be utilized by geothermal engineers and decision makers at an early stage of a project. The model estimates the lifetime as a function of typical physical and human controlled parameters, including reservoir porosity, reservoir initial temperature, discharge rate, well spacing, and injection temperature. Reaching this objective requires formulating mathematical relationships linking the involved parameters and operational scenarios. This necessitates conducting an extensive parametric analysis examining the behavior of the system for different reservoir parameters subjected to different operational scenarios. As the model is taking this combination of physical and human controlled parameters into consideration, the geometry should comprise all significant components, including the wellbores, the reservoir and the surrounding formation.

Modeling deep geothermal systems involves solving nonlinear conductive-convective heat flow occurring in a complicated and disproportionate geometry. This inevitably requires a numerical tool, of which the finite element method is one of the most suitable. Deep geothermal systems consist

of very slender wellbores embedded in a vast soil mass. This geometrical peculiarity exerts an enormous computational burden, as a combination of very fine elements and coarse elements is normally needed to discretize the physical domain. The problem gets even more complicated in the presence of nonlinear convection and fluid flow. For a three-dimensional system at a regional level, this normally requires hundreds of thousands to millions of elements, making the CPU time unrealistic for engineering practice.

To tackle this problem, and as the parametric analysis necessitates a large number of numerical analyses, a hybrid meshing technique is adopted. This technique entails reducing the spatial discretization of the wellbore from 3D to 1D and the surrounding soil formation from 3D to 2D, whereas the reservoir is kept 3D. The pseudo 3D model presented in Chapter 5 of this thesis (Saied et al., 2013) is used to simulate the wellbores using 1D elements. The soil formation surrounding the wellbores and the reservoir are modelled using standard 2D and 3D finite elements, respectively. This kind of dimensional reduction saves a significant number of finite elements, and makes the numerical analysis of a coupled reservoir-wellbore system feasible.

The finite element package COMSOL is utilized as a framework for implementing the proposed model and making the necessary coupling between the wellbores, soil formation and reservoir. The thermal interaction between these sub-domains is calculated simultaneously. Heat flow in the surrounding soil mass is modelled as linear conductive, and in the reservoir, it is modelled as nonlinear conductive-convective due to fluid density and viscosity dependency on temperature.

6.2 Model formulation

The finite element package, COMSOL, has been utilized as a framework to implement the wellbore model and couple it to the geothermal reservoir and the surrounding soil formation. The physical model is decomposed into three sub-domains: 3D, 2D, and 1D, representing the geothermal reservoir and its overburden and underburden layers, the overlying soil formation, and wellbores respectively (Figure 6-2). In this section, the governing heat equations of these sub-domains are presented, together with the initial and boundary conditions.

6.2.1 Soil formation and reservoir governing equations

Heat flow in a deep low-enthalpy geothermal system arises from thermal interactions between the injected wellbore fluid, the reservoir fluid and the surrounding soil mass. The governing equations describing heat and fluid flow in a porous medium have already been given in Chapter 5 (Eqs. (5.1) to (5.20)). Eqs. (5.1) to (5.8) describe heat flow in the solid matrix and formation fluid, whereas Eqs.(5.10) to (5.17) describe fluid flow in a porous medium taking into consideration the variation of density and viscosity with temperature. Eqs. (5.18) to (5.20) describe the relevant initial and boundary conditions.

It is also possible to calculate the rate of thermal energy extracted from a hydrothermal field in its lifetime. The thermal energy extracted from the reservoir per year of production ΔE_i can be calculated as (Bedre and Anderson, 2012),

$$\Delta E_i = \dot{m}_i c_p \Delta T_i \tag{6.1}$$

where, ΔE_i [W/year] is the annual thermal energy extracted in the i^{th} year, $\dot{m}_i$ [kg/year] is the total mass production of hot water in the i^{th} year, c_p [J/kg.K] is the specific heat of the circulating fluid and ΔT_i [K] is the temperature difference between produced and injected fluid in the i^{th} year. The total energy extracted from the system during its lifetime can obtained by

$$\Delta E = \sum_{i=1}^{n} \Delta E_i \tag{6.2}$$

in which, n is the total number of years of production.

6.2.2 Wellbore governing equations

Heat flow in a wellbore is conductive-convective and arises from the fluid flow and the thermal interaction between the wellbore components and the surrounding soil mass. Heat also generates in the pipes due to friction between the circulating fluid and the pipe tubing.

6.2.2.1 *Fluid flow in wells*

The mass flow inside the wellbore can be described using the conservation of mass equation:

$$\frac{\partial A\rho_f}{\partial t} + \frac{\partial}{\partial z}(A\rho_f u) = 0 \tag{6.3}$$

where , $A = \pi d_i^2 / 4$ [m²] is the cross sectional area of the pipe, d_i [m] is the inner pipe diameter, ρ_f [kg/m³] is the density, and u [m/s] is the fluid velocity.

The pressure drop along the wellbore (ΔP^w) can be described as (Livescu et al., 2010):

$$\Delta P^w = \Delta P_h^w + \Delta P_a^w + \Delta P_f^w \tag{6.4}$$

in which, ΔP_h^w is the hydrostatic pressure loss, ΔP_a^w is the pressure loss due to acceleration, and ΔP_f^w is the pressure loss due to frictional effects. The pressure loss due to acceleration in a typical reservoir simulation problem is smaller than the heat loss due to gravitation and friction (Livescu et al., 2010). These terms are defined as (Livescu et al., 2010):

$$\Delta P_h^w = -\rho_f g \sin\theta \tag{6.5}$$

$$\Delta P_a^w = -\rho_f \frac{\partial u}{\partial t} - \rho_f \frac{\partial^2 u}{\partial z^2} \tag{6.6}$$

$$\Delta P_f^w = -\frac{1}{2} f_D \frac{\rho_f}{d_i} |u| u \tag{6.7}$$

where P [N/m²] stands for pressure, superscript w stands for well, g [m/s²] is the gravitational acceleration, Θ is the wellbore inclination angle from the ground surface, and f_D is the Darcy friction factor.

The Darcy friction factor, $f_{D,}$ is a dimensionless quantity used for the description of friction losses in pipe flow as well as open channel flow. It is a function of the Reynolds number and the surface roughness divided by the hydraulic pipe diameter. Churchill's (1977) relation, which is valid for the entire range of laminar flow, turbulent flow, and the transient region in between (Lin et al., 1991), has been used to describe friction in pipes:

$$f_D = 8\left[\left(\frac{8}{\mathrm{Re}}\right)^{12} + (c_A + c_B)^{-1.5}\right]^{1/12} \tag{6.8}$$

in which C_A and C_B are defined as

$$C_A = \left[-2.457 \ln\left(\left(\frac{7}{\mathrm{Re}} \right)^{0.9} + 0.27 \left(\frac{e}{d} \right) \right) \right]^{16}$$
$$C_B = \left(\frac{37530}{\mathrm{Re}} \right)^{16} \tag{6.9}$$

e [m] is the tubing surface roughness, *d* [m] is the tubing diameter, and Re is the Reynolds number. Eq (6.8) shows that the Darcy friction factor is also a function of the fluid properties, through the Reynolds number, defined as:

$$\mathrm{Re} = \frac{\rho u d}{\mu} \tag{6.10}$$

For a low Reynolds number (laminar flow, Re < 2000), the friction factor is 64/Re (Brill and Mukherjee, 1999), and for a very high Reynolds number, the friction factor is independent of Re.

6.2.2.2 ***Heat flow in wells***

Heat flow in a wellbore is conductive-convective and arises from the flow of a working fluid running through an inner pipe (tubing), and the thermal interaction between the wellbore components and the surrounding soil mass, plus heat created by friction. Due to the high slenderness of the wellbore, heat variation is dominant in the axial direction and negligible in the radial direction. Hence, the heat equation of a wellbore can be described as

$$\rho_f c_f \frac{\partial T_i}{\partial t} - \lambda_f \frac{\partial^2 T_i}{\partial z^2} + \rho_f c_f u_i \frac{\partial T_i}{\partial z} = Q_{friction} + Q_{wall} \tag{6.11}$$

in which T_i describes the temperature in the working fluid, $Q_{friction}$ is the heat created by the friction inside the well and Q_{wall} describes the heat loss/gain to the surroundings. They are described as

$$Q_{friction} = \frac{1}{2} f_D \frac{\rho}{d_i} |u| u^2 \tag{6.12}$$

$$Q_{wall} = b_{is} \pi d_i (T_s - T_i) \tag{6.13}$$

where T_s is the temperature of the soil formation adjacent to the well, i.e. the 2D subdomain. b_{is} [W/m^{2}K] is the overall reciprocal of the thermal resistance

coefficient, which can be written as the sum of the thermal resistances between fluid, tubing, cement, and soil mass, as

$$b_{is} = \frac{1}{R_{\text{fluid}} + R_{\text{pipe material}} + R_{\text{gs}}} = \frac{1}{r_o / r_i \, \bar{h}} + \frac{r_o \ln(r_o / r_i)}{\lambda_{\text{p}}} + \frac{r_g \ln(r_g / r_{\text{o}})}{\lambda_{\text{g}}} \tag{6.14}$$

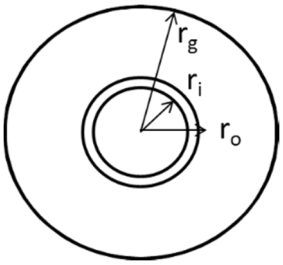

Figure 6-1. A cross-section of the wellbore

where r_i and r_o are the inner and the outer radius of the wellbore pipe respectively (Figure 6-1), r_g is the outer radius of the cement (grout), λ_p is the thermal conductivity of the wellbore pipe material, λ_g is the thermal conductivity of the cement, and $\bar{h} = Nu\,\lambda / 2r_i$, where Nu is the Nusselt Number (Saeid et al., 2013). For details, see Chapter 5, Section 5.2.2.2.

6.2.3 Initial and boundary conditions

Initially, at t = 0, the pressure is hydrostatic and the temperature in the wellbore is equal to the steady-state temperature in the soil (thermal gradient of the ground) before the system starts operating, as

$$T_i(z,0) = T_p(z,0) = T_g(z,0) = T_s(z,0) \tag{6.15}$$

in which T_s is the soil temperature immediately around the wellbore.

The boundary conditions typically involved in an operating wellbore are of two types: Dirichlet and Neumann. At the injection well, an inlet temperature and flow rate are prescribed as

$$T_i(z = 0, t) = T_{in}(t) \tag{6.16}$$

$$Q_i(z=0,t)=Q(t) \tag{6.17}$$

At the top of the production well, the heat flux and flow rate are prescribed as

$$-\lambda_f \frac{dT_p(z=0,t)}{dz}=0 \tag{6.18}$$

$$Q_p(z=0,t)=-Q(t) \tag{6.19}$$

At the bottom of the production well, the temperature is equal to the reservoir temperature at any time, i.e.

$$T_p(z=d_{\text{bottomhole}},t)=T_{reservoir}(z=d_{\text{bottomhole}},t) \tag{6.20}$$

where $d_{bottomhole}$ is the depth at which the bottom of the wellbore is located. Similarly, the pressure at the bottom of the production well is made equal to the reservoir pressure at any time, giving

$$P_p(z=d_{\text{bottomhole}},t)=P_{reservoir}(z=d_{\text{bottomhole}},t) \tag{6.21}$$

6.3 Finite element 1D–2D–3D hybrid modeling

A hybrid numerical discretization scheme is utilized to simulate a deep low-enthalpy geothermal system at a regional level. The geothermal system is assumed to consist of a reservoir; overburden and underburden; soil formation around the wells; and two wellbores. This system comprises highly disproportionate geometries. The wellbores are very slender, while the reservoir and the soil formations are large. Modelling such a system using standard 3D finite element discretization would require a huge number of elements and a large CPU time. To circumvent this numerical inefficiency, here, the reservoir and its overburden and underburden are discretised by 3D tetrahedral finite elements, the soil formation above the overburden is discretised by 2D triangular elements and the wellbores are discretised by 1D line elements. The finite element package COMSOL was utilized as a framework for this purpose. In the investigation, a series of parametric analyses was carried out and compared to the base case.

At every time step, the three sub-domains are fully coupled. Heat flow in the wellbore is described using Eq. (6.11). Fluid flow inside the wells is described

using Eqs. (6.3) and (6.4). The calculated temperature and pressure at the bottom hole of the injection well are prescribed at the inlet boundary of the 3D reservoir. Heat and fluid flow in the reservoir are described by Eqs. (5.3) and (5.9), Chapter 5. The dependency of density and viscosity on temperature are taken into consideration according to Eqs. (6.24) and (6.25). The calculated temperature and pressure at the production well location in the 3D sub-domain are prescribed as boundary conditions at the bottom inlet of the production well in the 1D sub-domain.

The 1D-2D and 3D sub-domains have been illustrated in Figure 6-5 and Figure 6-4, respectively. A cuboid of 900 [m] height, models the reservoir and its top and bottom impermeable layers (Figure 6-4). It is assumed that both wells fully penetrate the reservoir with vertical completion. The hydrothermal reservoir is considered to be homogenous and isotropic.

6.3.1 Geometry of the base case

Figure 6-2 shows a schematic presentation of the base case geometry. It represents a deep low-enthalpy geothermal system with dimensions of 2000 [m] x 1600 [m] x 2400 [m]. The reservoir is assumed to be 100 [m] in thickness and located at about 2 km below the ground surface. It constitutes a homogeneous sandstone with an average porosity of 0.15 and an average permeability of 725 [mD] (7.16 e-13 [m^2]). Its profile is inclined at an angle of 20^o to the horizon. The reservoir is bounded at the top and bottom by impermeable clay layers. The thermal and hydrological properties of the reservoir are shown in Table 6-1.

The soil formation is assumed to be a homogeneous clay layer with the same characteristics as the reservoir bounding layers. The wellbores constitute a doublet, 5 [m] apart at the ground surface and 1 [km] apart laterally at the reservoir level. Both wells are made of a composite material with 15 [cm] diameter, roughness of 0.0015 [mm], and a thermal conductivity of 0.42 [W/mK]. A layer of 4 [cm] cement with a thermal conductivity of 1.6 [W/mK] surrounds both wells. The production discharge is assumed to be 150 [m^3/h] and the injection temperature is set to 30 [^{o}C].

For inclined wells, where the top parts of the injection well and the production well are parallel and close to each other, knowing the influence area of each well is important for design purposes. It can help to place the infrastructure facilities which are sensible to temperature at the right distance from the wells.

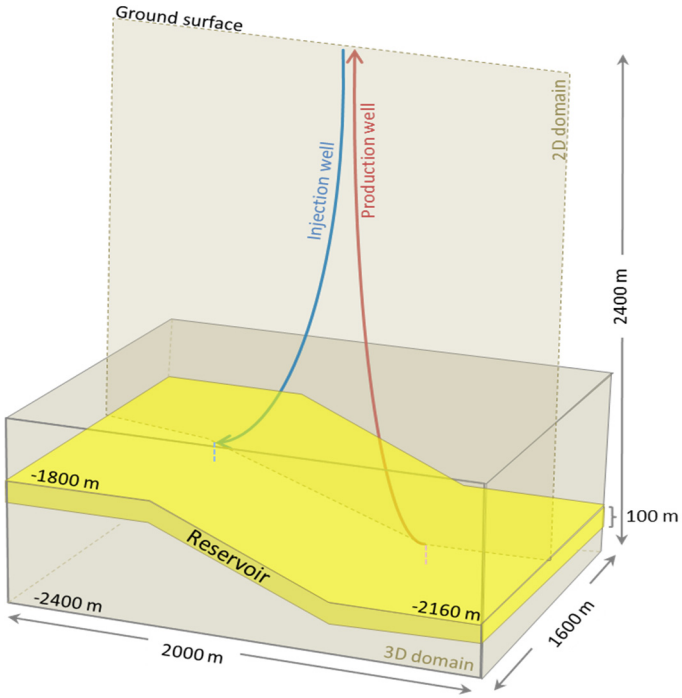

Figure 6-2. Schematic shape of reservoir, wells, and soil formation

Initially, at *t=0*, the pore pressure is hydrostatic, and the temperature distribution in all subdomains is assumed to be

$$T = 15 + 0.027z \tag{6.22}$$

in which T is temperature [°C] and z is the depth [m] from the surface. This provides initially a temperature of ~63 [°C] at the outlet of the injection well and ~76.3 [°C] at the inlet of the production well.

Upon system operation, Dirichlet boundary conditions for heat and fluid flow are imposed at the head of the injection well, Eqs. (6.16) and (6.17). The fluid temperature at the inlet of the injection well (well head) is prescribed as 30 [°C] and the flow rate as 150 [m^3/h].

Table 6-1. General properties of the reservoir model

Parameter	Symbols	Value	Unit
Reservoir			
Permeability	*K*	7.155 e-13	m^2
Porosity	ϕ	15	%
Fluid salinity	S	80	$gr.l^{-1}$
Soil density	ρ_s	2650	$kg.m^{-3}$
Fluid thermal conductivity	λ_f	0.67	$W.m^{-1}.K^{-1}$
Soil thermal conductivity	λ_s	3	$W.m^{-1}.K^{-1}$
Fluid specific heat capacity at	c_f	4190	$J.kg^{-1}.K^{-1}$
Soil specific heat capacity	c_s	980	$J.kg^{-1}.K^{-1}$
Adjacent layers			
Soil density	ρ_s	1750	$kg.m^{-3}$
Thermal conductivity	λ_s	2.2	$W.m^{-1}.K^{-1}$
Specific heat capacity	c_s	920	$J.kg^{-1}.K^{-1}$

6.3.1.1 *Mesh analysis*

To minimize numerical uncertainties, such as numerical errors or dispersion, in the finite element analysis, it is essential to choose a proper mesh size, constituting proper element sizes and numbers. The base case has been modelled by different mesh sizes, just in the 3D reservoir, from course to fine. It should be noted that special attention was given to create homogeneous mesh sizes inside the reservoir. The mesh size has been gradually increased until there is no significant difference in the numerical results between two successive mesh sizes (e.g. Nick et al., 2008). The finest mesh size is considered to be the reference case, from which an average error has been calculated as

$$\overline{error} = \frac{1}{i}\sum_{t=0}^{t=i}\frac{\left|T_{ref}^{t} - T_{x}^{t}\right|}{T_{ref}^{t}} \qquad (6.23)$$

in which, T_{ref}^{t} is the temperature at any time step of the reference case, T_{x}^{t} is the corresponding temperature of the mesh under examination, and *i* is the final time step. Table 6-2 and Figure 6-3 show the mesh sizes and the corresponding errors. They show that a mesh with an average element size of 35 [m] is proper for an accurate calculation.

Table 6-2. Different mesh sizes and calculated error at each step for mesh analysis

Max element size [m]	100	50	35	30	25	17
Number of elements	347786	372908	433004	492796	619250	1355229
Average Error	2.03E-02	6.37E-03	2.46E-03	1.74E-03	1.13E-03	(reference)
Run time [minutes]	7	10	35	70	130	320

The reservoir is discretized using 4-node 3D tetrahedral elements (COMSOL User's guid, 2011). Because of the non-linearity due to the density and viscosity variation with temperature, a relatively fine mesh for the reservoir is necessary. The soil formation is discretized using 3-node 2D triangular elements, and the wellbore is discretized using 2-node 1D line elements.

The Backward Euler time integration scheme has been utilized for the discretization of the time domain.

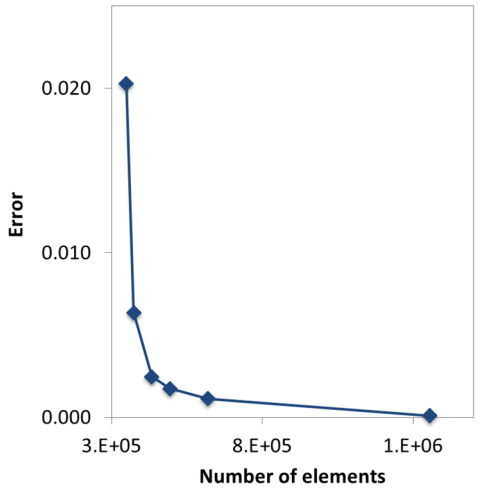

Figure 6-3. Mesh analysis for base case

6.3.1.2 *Computational results*

The base case represents a hydrothermal system subjected to cold water, T_{in} = 30 [°C], at the top of the injection well for 60 years of operation. Figure 6-4 shows the temperature distribution in the reservoir after 25 years of operation, displaying the injected cold water plume between the injection well and the production well.

Figure 6-5 shows the temperature distribution after 25 years of operation along the wellbores and is the surrounding soil formation. The temperature profiles for different times along the injection and production wells are depicted in Figure 6-6, left and right respectively, for different time intervals. It can be seen that the temperature gradient inside the wells after one day becomes closer to the inserted temperature, and becomes uniform at a later stage.

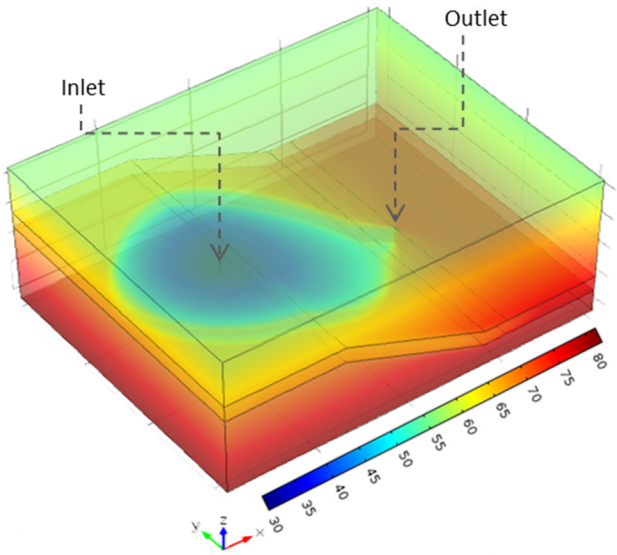

Figure 6-4. 3D model of cold water front after 25 years. Colors show the temperature in Celsius.

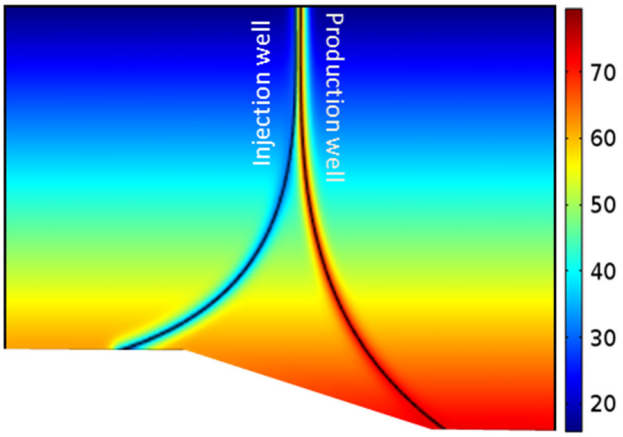

Figure 6-5. 1D- 2D model of wellbore interaction and soil formation after 25 years

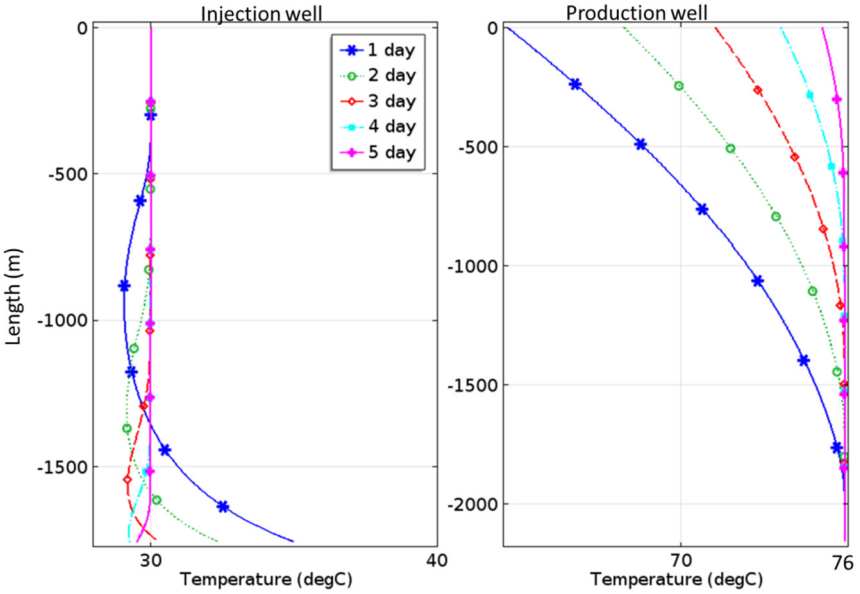

Figure 6-6. Temperature profile along injection (left) and production (right) well at different times

The influence area around the wells has been studied for the base case. For this specific geometry, material properties, initial conditions and boundary

conditions, the computational results show that (Figure 6-7) the wells have no noticeable thermal effect on each other. Heat transfer in the soil formation between the two wells has no effect on the fluid temperature inside the wells, but heat flow inside the wells has a significant effect on their surrounding soil formation. This is attributed to the dominant heat convection mechanism in the wells.

Figure 6-7 shows the influence areas around the injection and production wells at 50 [m] depth, at various times. As demonstrated, the influence radius around wells grows to more than 100 m after 60 years of injection and production. For the injection well, the influence area is relatively small at shallow depths, due to the small temperature difference between the injected temperature and the formation temperature, while, for the production well, it is the reverse. The area between the two wells is, in this case, affected by the temperature gradient between them.

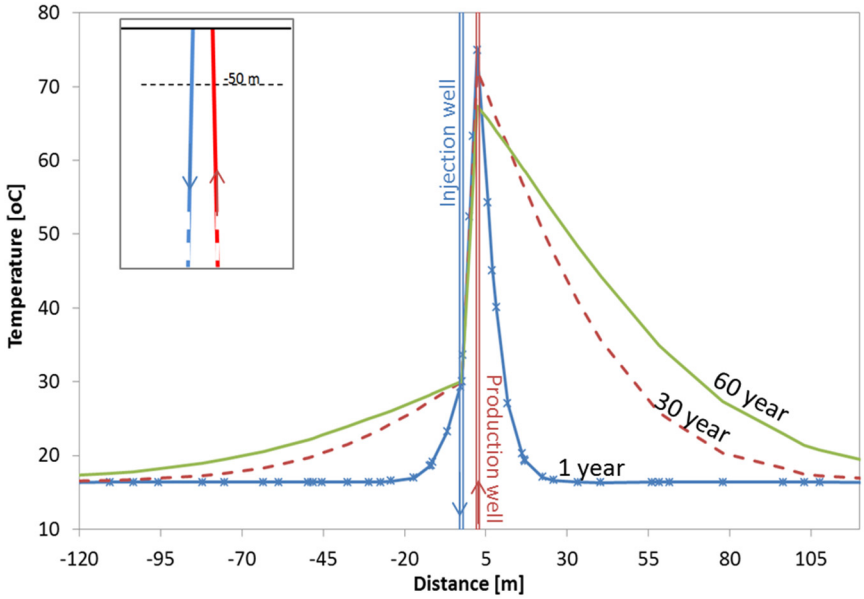

Figure 6-7. Temperature around injection and production wells at 50 m depth; after 1, 30, and 60 years.

6.4 Parametric analysis

To formulate a design model capable of giving an estimate on the lifetime of a geothermal reservoir, an extensive parametric study has been conducted. Three issues are considered: 1) determining the significance and insignificance of the different parameters, 2) quantifying the effect of the significant parameters on the system lifetime, and 3) coupling the effects of the significant parameters such that the model is physically interpretable.
The studied parameters are divided in two categories:

- Physical parameters
    - Reservoir initial temperature
    - Salinity
    - Porosity
- Human controlled parameters
    - Injection temperature
    - Well spacing
    - Discharge
    - Injection scenarios
    - Tubing material

The parametric analysis is performed by varying one parameter at a time, while keeping the rest constant at the base case values. The lifetime of the system was taken as the comparison parameter. The lifetime is defined as the time at which the temperature at the production well drops to 60 [^{o}C].

6.4.1 Reservoir initial temperature effect

Reservoir initial temperature can play a significant role on the lifetime of the geothermal system. It is defined by the thermal gradient of the ground and the reservoir depth and its inclination.

To study the effects of the initial temperature, reservoir depth and inclination on the system lifetime, 9 different scenarios have been examined. The first three scenarios (A, B, C) represent three reservoirs with three different slopes (inclined, horizontal, highly inclined), in which the initial temperature of the reservoir is a function of depth (Figure 6-8). The second three scenarios (D, E, F) have the same geometry as A, B, and C respectively, but the initial temperature is assumed constant (not a function of depth). The third three scenarios (G, H, I) have the same geometry as case A (base case), while being located at different depths, and therefore having different initial temperatures.

In all scenarios, the shortest distance between the two well bottoms is kept constant at 1000 [m]. All nine reservoirs have the same reservoir thickness and similar thermal and hydraulic properties as that of the base case (see Table 6-1).

The first three scenarios are:

A. Inclined reservoir; with 20^{o} dip (Base case); $T_{initial}$=*f(depth),* D_{ave}=2050 [m]
B. Horizontal reservoir; $T_{initial}$=*f(depth),* D_{ave}=2250 [m]
C. Highly inclined reservoir; with 30^{o} dip; $T_{initial}$=*f(depth),* D_{ave}=1950 [m]

Figure 6-8 shows the geometry and initial temperature distribution in scenarios A, B, and C. The position of the production well is fixed; thus the initial temperature at this well is constant in these scenarios.

The initial thermal gradient is assumed to vary according to Eq.(6.22), giving a temperature of around 76 [^{o}C] at the bottom of the production well. The temperature range between the injection and production wells varies in different scenarios, based on the reservoir dip. In the base case (case A), the temperature range between the top and the bottom of the reservoir varies between 65 [^{o}C] and 76 [^{o}C], in the horizontal case (case B) it is constant, at about 76 [^{o}C], and in the highly inclined case (case C) it varies between 55 [^{o}C] and 76 [^{o}C]. More detailed information about the geometry and the initial temperature of these scenarios is given in Table 6-3.

The breakthrough curves (at the production well) for these scenarios are shown in Figure 6-9. Scenario B shows a plateau in the breakthrough curve during the first 10 years. After that, it exhibits a dropdown. Scenarios A and C exhibit a rapid dropdown from the very beginning. The reason for this significant difference is attributed to the difference in the geometry/inclination of the reservoir and its associated initial temperature difference. In scenarios A and C, because of the reservoir inclination, a non-isothermal zone is created around the production well from the very beginning. In case B, due to the horizontal oriantation of the reservoir, the initial temperature around the production well stays uniform, for about 10 years, after which, the temperature declines.

Scenarios D,E,F are modelled to evaluate merely the effect of the reservoir inclination on the system's lifetime. The geometry of scenarios D, E, and F are identical to A, B, and C respectively. The initial temperature is in this case considered independent of depth, i.e. constant.

The scenarios are:

D. Inclined reservoir; with 20° dip; $T_{initial}$=*constant*
E. Horizontal reservoir; $T_{initial}$= *constant*
F. Highly inclined reservoir; with 30° dip; $T_{initial}$=*constant*

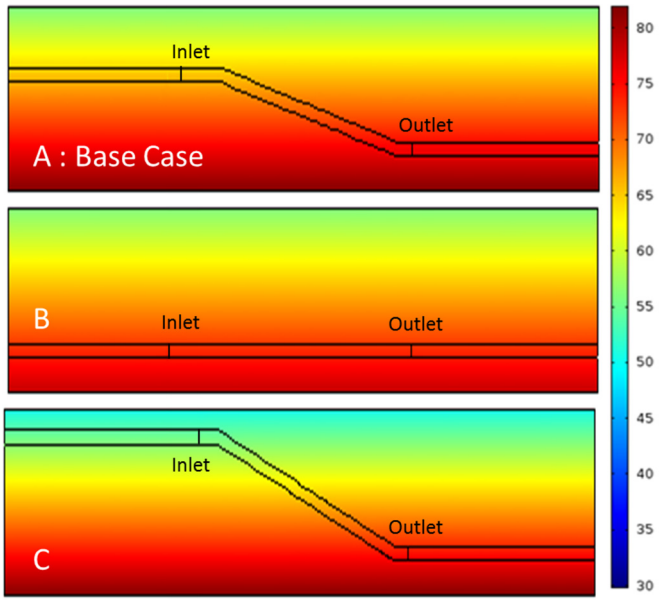

Figure 6-8. Geometry and initial thermal conditions of three scenarios

In these scenarios the initial temperature is assumed to be 76 [°C] (similar to the initial temperature at the production well in scenarios A, B, and C). Figure 6-10 shows the three scenarios when T_0=*f*(depth) (A, B, and C) and when T_0=constant (D,E, and F). Cases D, E, and F clearly show a similar trend; a constant production for about 10 years and a gradual dropdown afterwards. It can be concluded that the initial temperature gradient in the reservoir is an important parameter and must not be neglected or unrealistically estimated. Otherwise, a non-realistic (mostly optimistic) prediction of lifetime is obtained.

Scenarios G,H,I are modelled to evaluate merely the effect of the "average" initial temperature of the reservoir on the system's lifetime. All three scenarios have the same geometry as case A (base case), while being located at different depths and therefore having different initial temperatures.

The scenarios are:

G. *Inclined reservoir; with 20^o dip; $T_{initial}$=f(depth),* D_{ave}=1850 [m]
H. *Inclined reservoir; with 20^o dip; $T_{initial}$=f(depth),* D_{ave}=2250 [m]
I. *Inclined reservoir; with 20^o dip; $T_{initial}$=f(depth),* D_{ave}=2450 [m]

The geometry and the initial temperature at the injection and production wells are given in Table 6-3. The breakthrough curves of these scenarios are plotted in Figure 6-11 and compared with the base case. The figure shows that, as the average reservoir temperature increases, the breakthrough curve shifts parallel upward.

Table 6-3. Depth and initial temperature at injection and production well in different scenarios

	Injection well		Production well	
Scenarios	Depth [m]	$T_{initial}$ [^{o}C]	Depth [m]	$T_{initial}$ [^{o}C]
A	1850	64.95	2260	76.02
B	2260	76.02	2260	76.02
C	1500	55.5	2260	76.02
D	1850	76.02	2260	76.02
E	2260	76.02	2260	76.02
F	1500	76.02	2260	76.02
G	1650	59.55	2050	70.35
H	2050	70.35	2450	81.15
I	2200	74.4	2600	85.2

Figure 6-12 shows the dependency of the reservoir lifetime on the reservoir average initial temperature. For Scenarios A, B, and C, it can be concluded that, as the dip angle increases, the lifetime decreases. This is due to the thermal gradient in the ground which is manifested more in the highly inclined reservoir.

For D, E and F it can be concluded that the effect of inclination of the reservoir on fluid velocity is not significant on the system's lifetime. Comparing scenarios G, H, I, and A shows that the lifetime increases linearly as the average initial reservoir temperature increases.

Comparing all scenarios together demonstrates that the effect of the reservoir initial temperature, independently of the reservoir depth and inclination, is very important and has to be considered in the model.

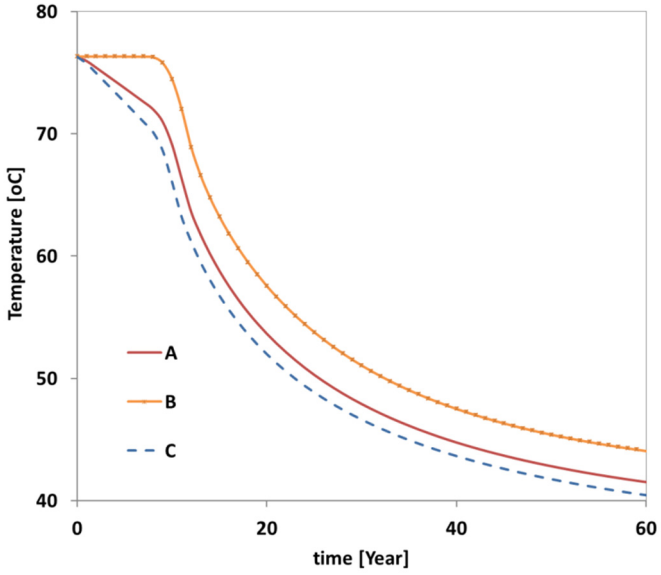

Figure 6-9. Breakthrough curves for scenarios A, B, and C.

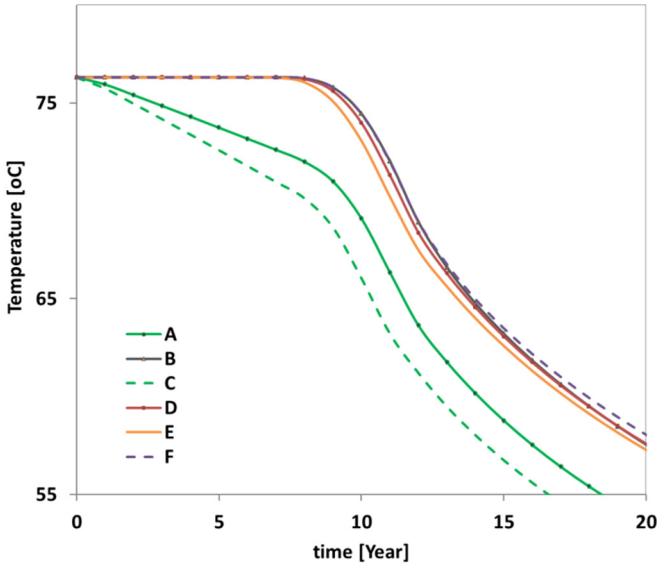

Figure 6-10. Breakthrough curves for scenarios A, B, C, D, E, and F.

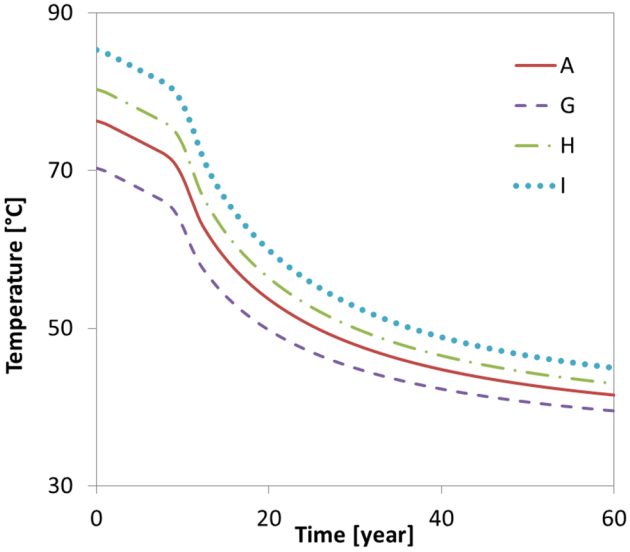

Figure 6-11. Breakthrough curves for scenarios A, G, H, and I.

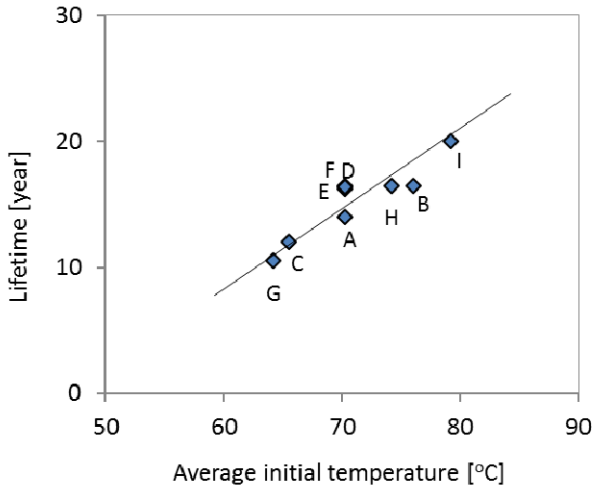

Figure 6-12. System lifetime versus average initial temperature of the reservoir for scenarios A to I

6.4.2 Salinity effect

In this section, the effect of the reservoir fluid salinity on the lifetime of the geothermal system is evaluated. Fluids with different salinities have different densities and viscosities, and the variation of their densities and viscosities with temperature is different for different salinities.

Four cases are considered: water with temperature-dependent density and viscosity (Lide and David, 1990), and brines 40 [gr/l], 80 [gr/l] (base case) and 160 [gr/l] with temperature-dependent density and viscosity (Batzle and Wang, 1992). All cases are similar in terms of hydrothermal parameters and initial and boundary conditions as the base case, but different in terms of density and viscosity.

The brine viscosity variation with salinity and temperature is described as (Adams and Bachu, 2002):

$$\mu_{_B} = 0.1 + 0.333S + \left(1.65 + 91.9S^3\right)\exp\left\{-\left[0.42\left(S^{0.8} - 0.17\right)^2 + 0.045\right]T^{0.8}\right\} \qquad (6.24)$$

and the brine density variation with salinity and temperature is described as

$$\rho_{_B} = \rho_{_W} + S\left\{0.668 + 0.44S + 1e-6\left[300P - 2400PS + T\left(80 + 3T - 3300S - 13P + 47PS\right)\right]\right\} \qquad (6.25)$$

where ρ_s and ρ_W are the saline and water density [g/cm^3], S is the brine mass fraction [ppm/10^6], p is the pressure [MPa], μ_s is the viscosity in [cp], and T is the temperature [^{o}C].

The breakthrough curves for four cases are shown in Figure 6-13. As is shown, as the salinity increases, the breakthrough curve become sharper, and consequently the lifetime of the geothermal system decreases. Figure 6-14 shows a decrease of the lifetime due to an increase in the geothermal reservoir salinity. The same trend is observed for the total energy extracted from the reservoir during its lifetime.

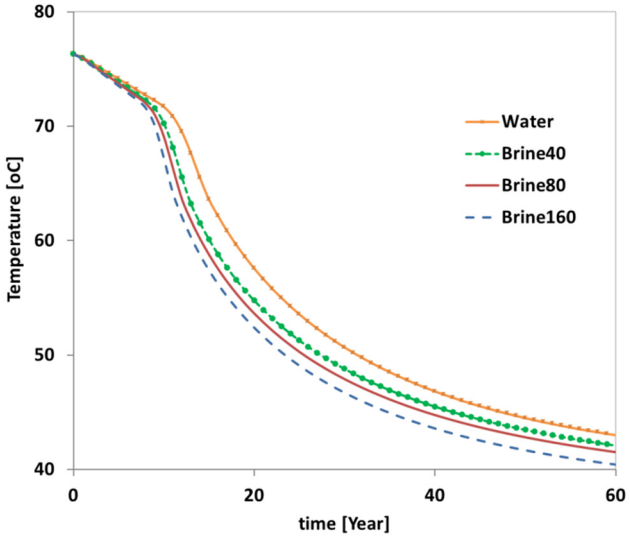

Figure 6-13. Breakthrough curves for water and brine 40, 80 (Base case), and 160 [gr/l]

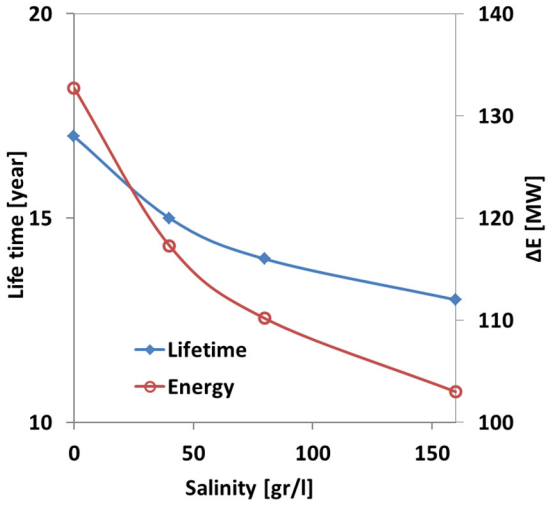

Figure 6-14. Decrease of lifetime and energy by increase in geothermal reservoir salinity

6.4.3 Porosity effect

The porosity of a geothermal reservoir formation is considered to be one of the important parameters that can affect the system lifetime. To quantify this effect, four scenarios have been studied based on the base case, using five different porosities; 10%, 15% , 20%, 30%, and 40%.

Figure 6-15 shows the breakthrough curves of these scenarios. It shows that, as the porosity increases, the breakthrough curves become sharper and the lifetime becomes shorter.

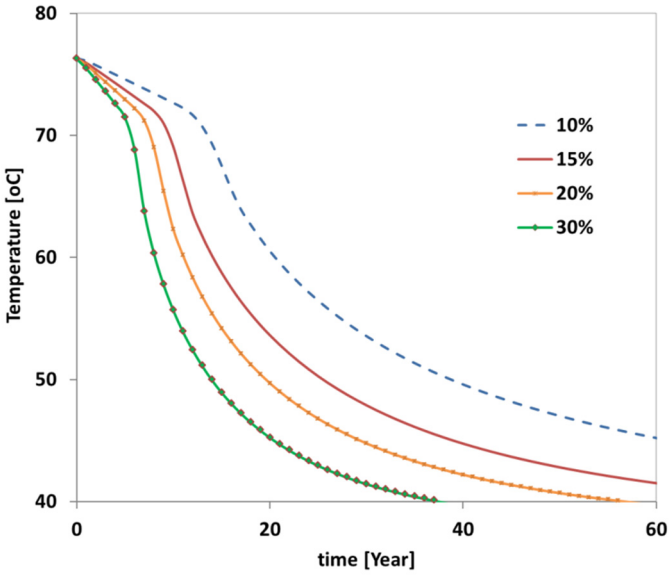

Figure 6-15. Breakthrough curves for cases with different porosity

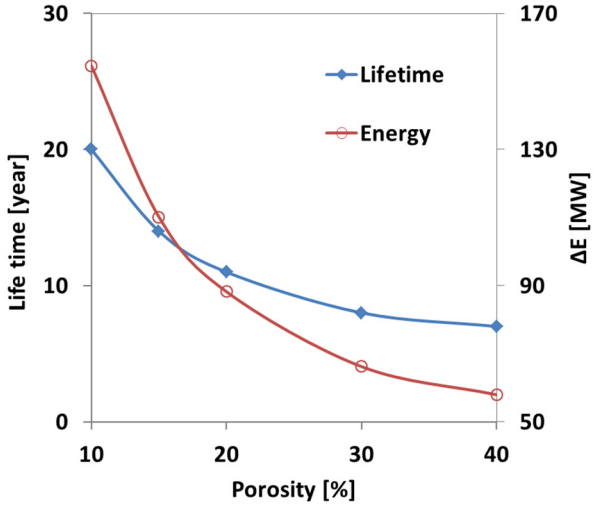

Figure 6-16. Effect of porosity on lifetime and total energy

Figure 6-16 shows the effect of porosity on the lifetime for these cases: as the porosity increases, the system's lifetime and the total thermal energy extracted from the reservoir during its lifetime decrease. It is notable that the inverse relation of the geothermal reservoir porosity and its lifetime shows an exponential decay, meaning that the effect of porosity on the lifetime is more important at low values of porosity, compared to high porosity values (Figure 6-16).

6.4.4 Injection temperature effect

The injection fluid temperature is representative of the heat enthalpy being returned to the reservoir. Higher injection fluid temperatures provide lower thermal drawdown and thus a longer lifetime of the reservoir. However, higher injection temperatures result in lower rates of energy extraction from the reservoir (Eq.(6.1)). Therefore, the injection temperature is a critical parameter that needs to be studied. It has to be chosen carefully, such that the demanded energy extraction is maintained within the desirable lifetime.

In order to study the effect of injection temperature on the lifetime of the low-enthalpy hydrothermal system and the energy extracted from it, four scenarios with different injection temperatures have been considered. The first scenario is the base case in which the injection temperature equals 30 [^{o}C]. The other scenarios are defined relative to the base case with injection temperatures of 35, 40, and 50 [^{o}C].

Figure 6-17 shows the breakthrough curves for these scenarios. For this example, according to the defined criterion for lifetime, the injection temperature effect is not significant within the lifetime of the system, especially for the first three scenarios. Figure 6-18 shows the variation of the lifetime and the energy extracted versus the injection temperature. As the injection temperature increases, the lifetime of the system increases, while the extracted energy from the system decreases.

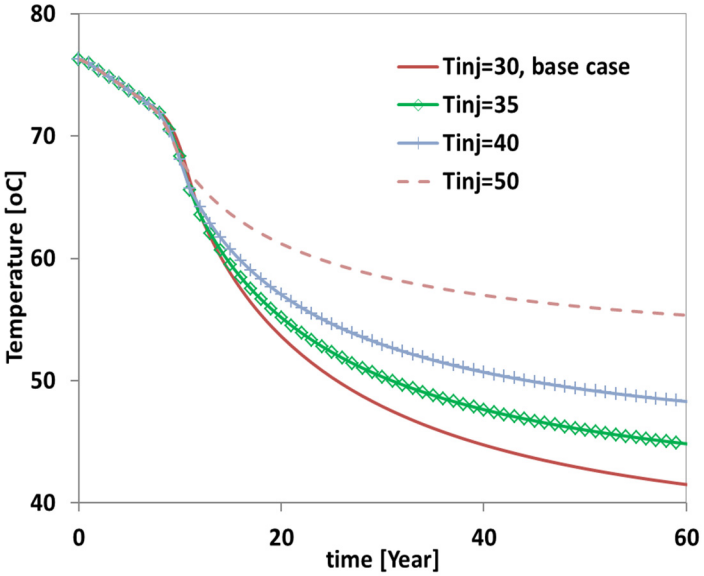

Figure 6-17. Breakthrough curves for scenarios with different injection temperature. Injection temperatures are in °C in this figure

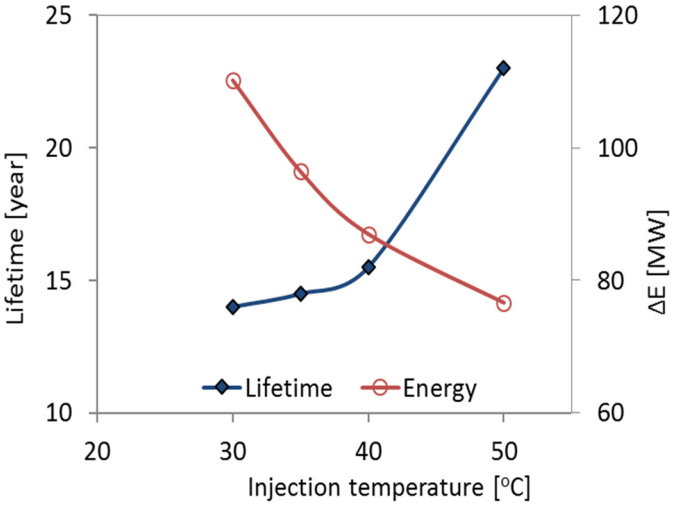

Figure 6-18. Variation of lifetime and the energy extracted from the system by variation of injection temperature

6.4.5 Well spacing effect

The wellbores in the reservoir are always recommended to be placed at an optimum distance from each other. A large well spacing provides a larger reservoir size, and hence a longer lifetime. However, the possibility of fluid loss and less recovery increases with larger reservoirs (Bedre and Anderson, 2012). In contrast, a smaller well spacing provides a smaller reservoir, and hence a shorter lifetime, although most of the fluid can be recovered.

Well locations are determined by geology, ease of drilling and operation, and maximum production flow rates (Bedre and Anderson, 2012). Geological factors such as existence of faults and fractures, and heterogeneities in porosity and permeability, play an important role in locating the wells. Overall, the well spacing needs to be optimized to provide proper reservoir size and lifetime, and maximum production flow rate.

To show the effect of well spacing, the base case has been simulated for different well distances. Seven well spacings have been considered: 1000, 1200, 1500, 1750, 2000, 2500, and 4000 [m].

Figure 6-19, shows the well spacing versus the system lifetime. As shown, the lifetime increases linearly with the well spacing (according to the specified definition of lifetime). There are three explanations for this linear growth:

- The reservoir is considered to be homogeneous with no geological complexity or barriers. Thus any increase in well spacing just increases the reservoir size and volume.
- The flow boundaries have been defined with a fixed discharge. This means that there is always enough pressure for production, independent of the size of the reservoir.
- The lifetime has been defined as the time at which the temperature in the production well reaches 60 [^{o}C] in all cases. If the lifetime is defined differently, for example by a certain number of years, different trends would be expected (Bedre and Anderson, 2012).

It is important to mention that, in all cases, the lateral well spacing has been altered while the average initial temperature of the reservoir has been kept the same as the base case. This means that the reservoir inclination and therefore the lateral location of the production well have been altered, but the depth, and therefore the temperature at both well locations have not been changed. As has been shown before, Figure 6-10 and Figure 6-12, reservoir inclinations do not have a significant effect on the system lifetime,

when the initial temperature of the reservoirs is the same. Therefore, it is reasonable to relate all these variations in lifetimes only to the well spacing.

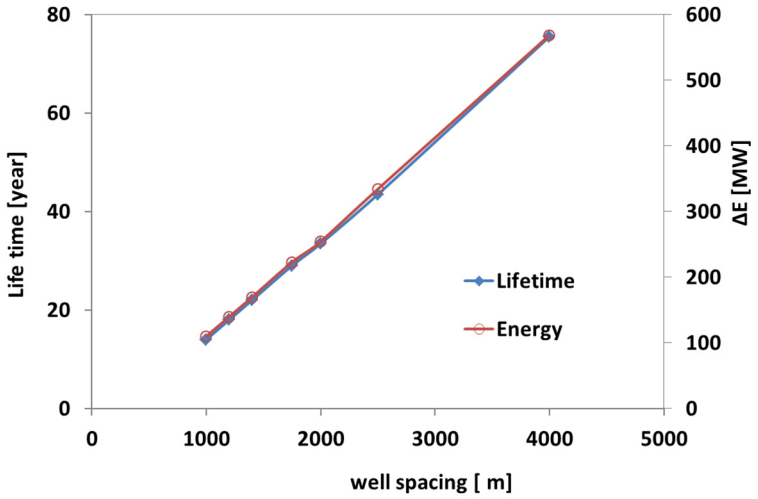

Figure 6-19. Effect of well spacing on lifetime and energy extracted

6.4.6 Discharge effect

Discharge is not considered as an ambiguous or uncertain parameter in geothermal fields, but its variation has a direct effect and, perhaps, the most significant effect on the project lifetime. To quantify the discharge effect, four scenarios are studied. All cases are identical to the base case except for the discharge rate. The cases are:

I. Discharge=150[m^3/h] (base case)
II. Discharge=50[m^3/h]
III. Discharge=100[m^3/h]
IV. Discharge=250[m^3/h]

Figure 6-20 shows the breakthrough curves of these cases. Higher discharge rates exhibit sharper breakthrough curves. Figure 6-21 shows the relationship between the flow rate and the system lifetime. As the figure illustrates, in this example, there is a significant reduction in the system's lifetime when the discharge increases from 50[m^3/h] to 100[m^3/h]. However, for higher discharge values this becomes less significant.

It is noticeable that, for lower discharge rates, the viscosity and density effects are more visible and more important. Density and viscosity effects, combined with heat loss to the adjacent layers plus the geometric effect of the inclined reservoir, causes a slight underlying of the cold water (cold water tends to move downward due to its higher density). By decreasing the temperature in the reservoir, the kinematic viscosity (ν) of the fluid decreases and, with the assumption of a constant intrinsic permeability, the hydraulic conductivity (K) decreases, see Eq.5.11. The corresponding decrease in hydraulic conductivity causes a gradual slowdown in the cold front velocity. For higher discharge rates, the front is very convective and therefore sharp (Figure 6-22-A, B, C), while for lower flow rates, the front is more conductive and less sharp (Figure 6-22-A', B', C'). Underlying of cold water, which is caused due to density-viscosity effects, is more visible for lower discharge rates.

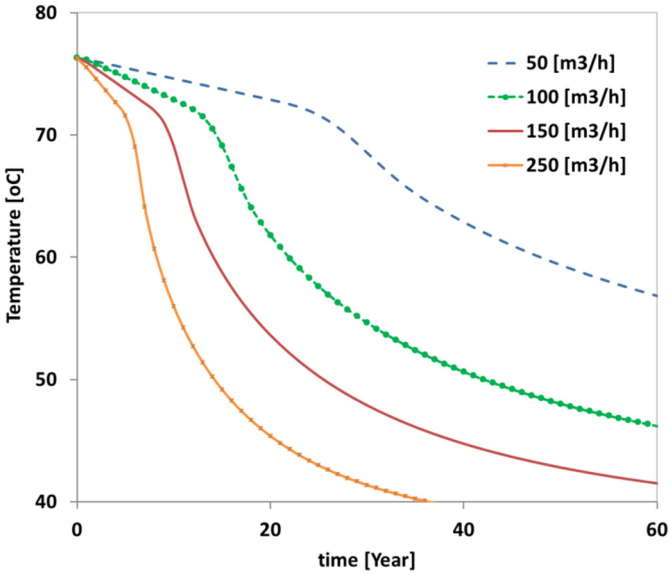

Figure 6-20. Breakthrough curves for scenarios with different flow rate

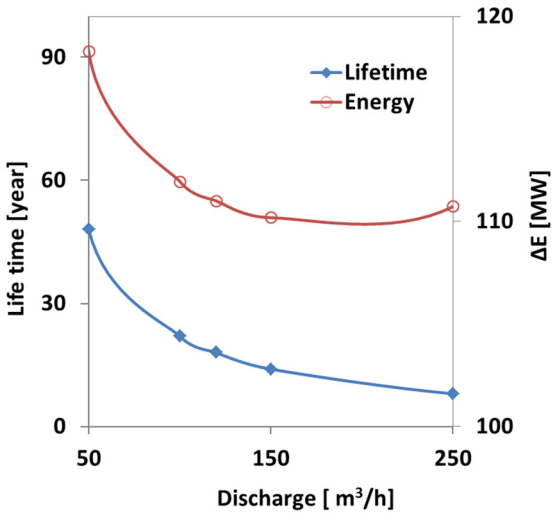

Figure 6-21. Dependency of lifetime on fluid flow rate

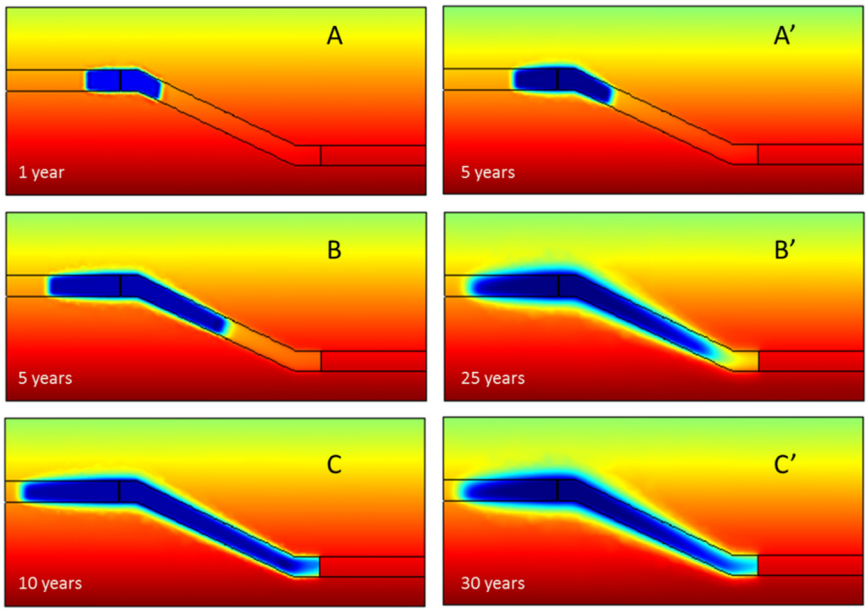

Figure 6-22. Cold front shape for flow rate of 150 [m³/h] (A, B, and C) and 50 [m³/h] (A', B', and C')

6.4.7 Injection scenario effect

In low enthalpy geothermal systems, often the injection temperature varies based on demand. For example, during winters, a lower temperature is injected into the reservoir, compared to summer times when normally less thermal energy is needed. Or it might happen that the demand of thermal energy varies for different years, and thus the injection and production scenarios change accordingly. In this section, the variation of injection temperature on the whole geothermal system is evaluated.

Three scenarios have been studied and compared:

I. Constant injection temperature (base case); Ti=30 [°C]
II. Periodic injection temperature; Ti_{min}=15 [°C], Ti_{max}=45 [°C], with period range of 6 month
III. Periodic injection temperature; Ti_{min}=15 [°C], Ti_{maxr}=45 [°C], with period range of 1 year

The first scenario is the base case with a constant injection temperature of 30 [°C], whereas, the second and third are periodic injection scenarios, in which the temperature varies between 15[°C] and 45 [°C], for the period of 6 months and 1 year, respectively. A square signal has been utilized for the periodic injection temperature scenarios, Figure 6-23. The average injection temperature of the periodic scenarios is made identical to the base case, for the sake of comparison.

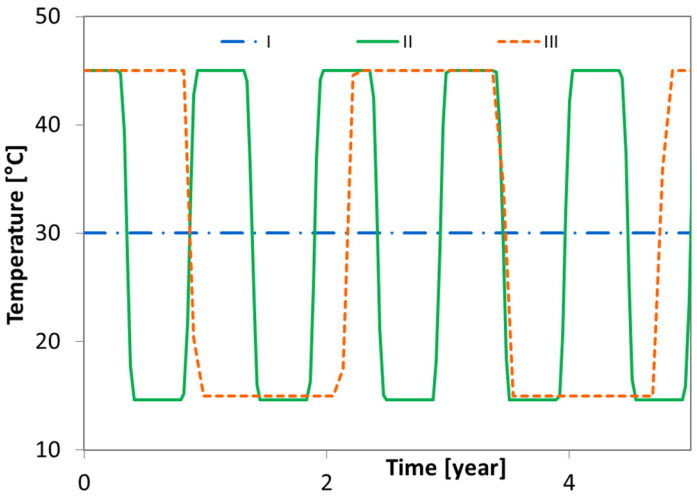

Figure 6-23. Temperature at the bottom and top of the injection well over 5 years, for the base case and periodic injection cases, scenarios II and III

The computational results for the three scenarios are shown in Figure 6-24. The temperature distribution at the bottom of the production well is shown. According to Figure 6-24, for scenario III, after the breakthrough, a periodic wave can be seen at the production well, in this case after 13 years. Looking at the beginning and tail of the curve, it can be seen that just after the breakthrough, the amplitude and period of the signal is different to the tail. At the beginning, the amplitude is smaller and the period is longer. In contrast, for scenario II almost no wave is visible at the beginning and, just at the very end, a wave signal with very small amplitude appears.

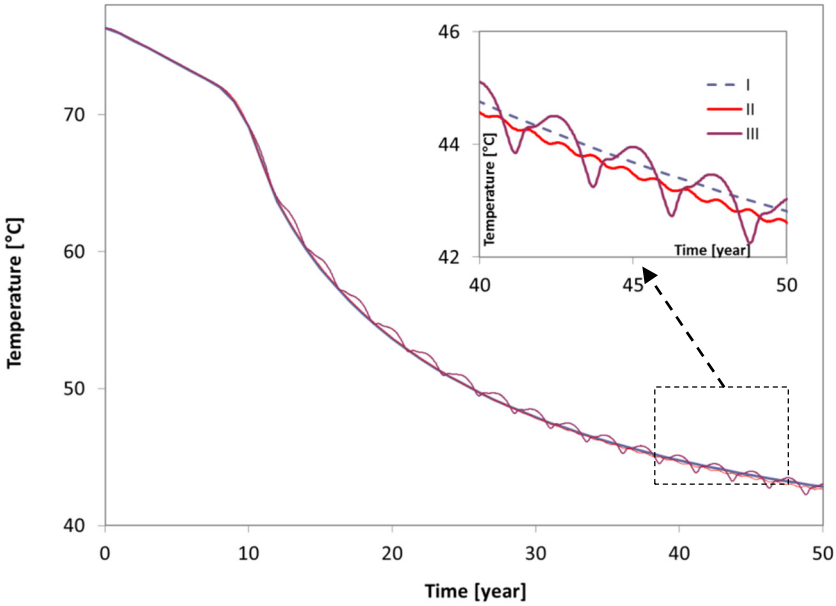

Figure 6-24. Breakthrough curves at the bottom hole of production well for scenarios I, II, and III

It is notable that, although the periodic injection causes a periodic output, it gives on average a temperature similar to that of the constant injection rate scenario. As the temperature difference between the minimum and maximum of the input signal amplitude decreases, the periodic injection effect become less and less visible in the breakthrough curve.

It is noticeable that including a periodic injection in the model needs special attention to the time step size, which has to be much smaller than the temperature variation period.

It can be concluded that the seasonal injection does not make a significant difference to the average heat flow in the production well, as long as the average injection temperature and discharge are kept similar to the base case. In such cases, a simple model with a constant injection temperature can be used for predictions.

6.4.8 Tubing material effect

Steel tubing has been used conventionally for oil, gas and geothermal wells. Recently, composites with higher stiffness to weight ratio, greater thermal resistance (lower thermal conductivity), and less subjected to fatigue have been examined and used for drilling. These materials have a positive effect on the drilling process and system efficiency. Here, their effect on the thermal transport in geothermal wellbores is tested.

The most important characteristics of the different tubing materials that influence the heat transport inside the tubes are their thermal conductivity and roughness. The effect of geothermal tubing materials on heat transport inside the wellbore is studied for two tubing materials: 1) steel with a thermal conductivity of 8 [W/m.K] and roughness of 0.15 [mm]; 2) composite with a thermal conductivity of 0.42 [W/m.K] and roughness of 0.0015 [mm]. The study is conducted for a discharge rate of 150[m^3/h].

Figure 6-25 shows the temperature profile along the injection and production wells, after 1 and 24 hours, for the steel and the composite pipes. As shown in this figure, the steel pipe has more interaction with the soil formation, as heat conduction to the soil formation (heat loss/gain) occurs more in the steel pipe, compared to the composite pipe. As a result of this heat loss to the soil formation, the fluid temperature in the steel pipe production well is less than the fluid temperature in the composite pipe.

Figure 6-26 demonstrates the transition period needed in the injection and production wells with both tubing materials. This period is about 5 days in the production well and about 4 days in the injection well. The point is that both materials show almost the same transition period.

Figure 6-25 and Figure 6-26 show that the effect of the tubing material on heat transfer is not significant and can be ignored. Nevertheless, the tubing material can play a significant role on the drilling, which is not considered here.

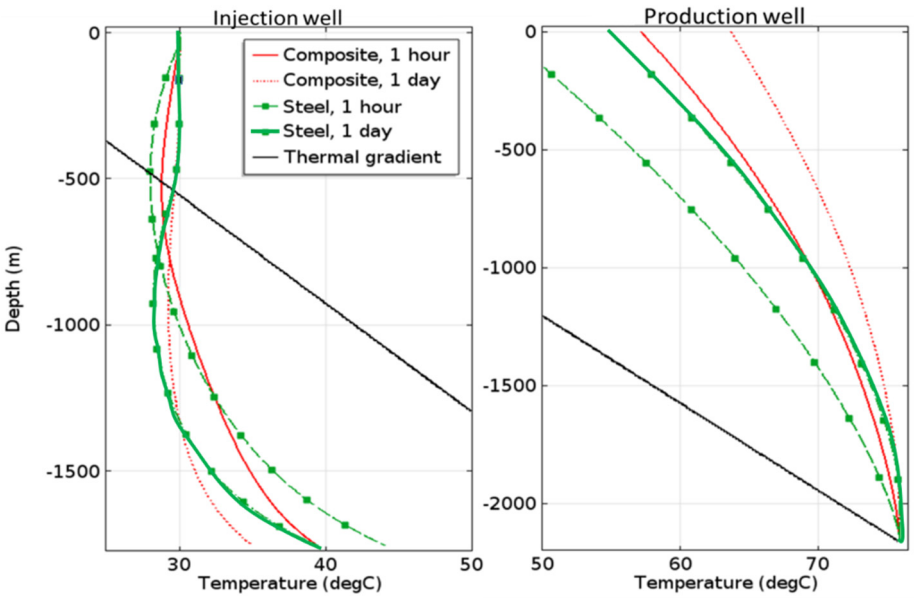

Figure 6-25. Temperature profiles after 1 and 24 hours of project start up in composite and steel tubing (note: thermal gradient refers to in-situ condition)

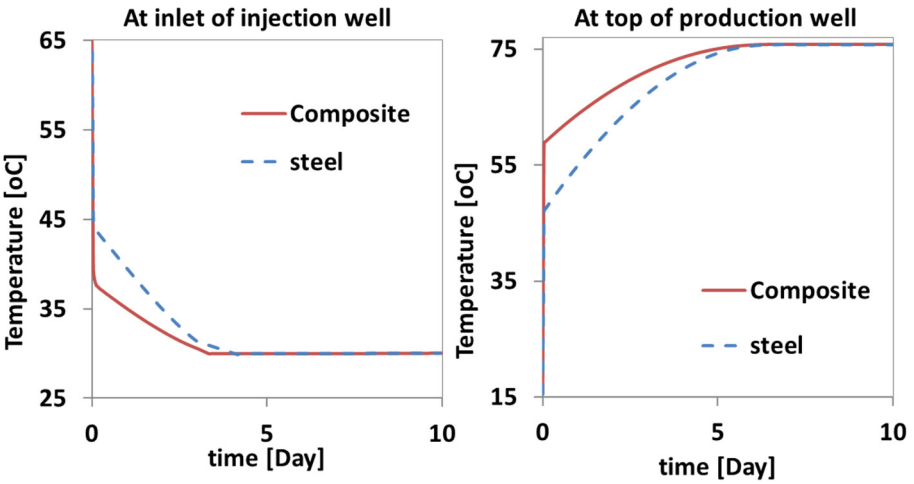

Figure 6-26. Thermal breakthrough at the bottom of the injection well (left) and top of the production well (right) for composite and steel tubing

6.5 A prototype design model

As discussed before, in geothermal systems, the lifetime of the reservoir is one criterion which is very important in decision making. It describes how long a geothermal system can operate while providing desirable energy. That can help in estimating how economic and viable the system is. It is therefore useful to have a reliable estimate of a system's lifetime before starting detailed study and modeling. In this section, a prototype model capable of predicting the lifetime of a low-enthalpy hydrothermal system is introduced. The model is formed based on the outcomes of the parametric analysis which have been carried out in section 6.4.

The parametric analysis showed that, among all the studied natural and human controlled parameters, reservoir porosity, discharge rate, well spacing, average initial temperature of the reservoir and injection temperature have a significant impact on the reservoir lifetime. Porosity and the initial temperature of the reservoir are important natural parameters, whereas discharge rate, the injected temperature and the well spacing are important human controlled parameters that can be optimized to obtain the highest lifetime with the highest energy production rate. In addition, the study demonstrates that there is a clear trend in the variation of lifetime with the variation of each parameter.

Knowing the main parameters which have the highest impact on a system's lifetime, a model can be made which relates all five parameters to lifetime. For this, several simulations were carried out relative to the base case by varying porosity, discharge, well spacing, and initial and injection temperature. Lifetime has been measured for each set. The lifetime is defined, as mentioned before in this chapter, as the time in which the fluid temperature reaches 60 [^{o}C] at the production well.

The model is formulated: first, by correlating the lifetime to the porosity and the discharge; then the lifetime is weighted by adding the effect of well spacing, reservoir initial temperature and injection temperature.

6.5.1 Lifetime as a function of porosity and discharge

To study the co-relation between the reservoir porosity and discharge and the system's lifetime, several simulations were carried out on the base case by varying the porosity between 0.1 and 0.4, and the discharge between 50 [m^3/h] and 250 [m^3/h]. The computed lifetimes in years of operation for the different cases are given in Table 6-4.

Table 6-4. Lifetime measured for different combinations of porosity and discharge rate

ϕ / Q [m³/h]	0.1	0.15	0.2	0.3	0.4
50	74	48	37.5	27	22
100	33	22	17.9	13	11
150	20	14	11	8	7
250	12	8	6.5	4.8	4

Figure 6-27 demonstrates the variation of lifetime with discharge for different porosities. Apparently, there is an exponential trend in this relationship that can elegantly be put in a mathematical model, which relates all these parameters together. The model can be formulated by fitting curves to each set of lifetime-discharge data for different porosities. All curves can be expressed in a general form as:

$$L_1 = a + b\,\mathrm{e}^{-Q/c} \tag{6.26}$$

in which L is the lifetime in years and Q is the discharge in [m³/h]. a, b and c are constants.

The fitting curve for each set is expressed as:

$$\begin{aligned}
&\phi = 0.1 \quad ; \quad L_1 = 11.25 + 165e^{-Q/46.5} \\
&\phi = 0.15 \; ; \quad L_1 = 7.5 + 110e^{-Q/50} \\
&\phi = 0.2 \quad ; \quad L_1 = 5.6 + 82.5e^{-Q/53} \\
&\phi = 0.3 \quad ; \quad L_1 = 3.75 + 55e^{-Q/60} \\
&\phi = 0.4 \quad ; \quad L_1 = 2.8 + 41.2e^{-Q/65.5}
\end{aligned} \tag{6.27}$$

where a, b and c are functions of porosity. Parameter a represents the lifetime of the reservoir for an "infinitely" high discharge, and parameter b represents the lifetime for a small discharge (minus a). By inspecting Eq. (6.26), it can be seen that these parameters are directly related to the porosity, such that:

$$a = \frac{1.125}{\phi}$$
$$b = 14.7a = \frac{16.53}{\phi} \tag{6.28}$$

Parameter *c* represents the shape of the lifetime decay with increasing discharge. Figure 6-28 shows a linear relationship between parameter *c* and porosity. It can be described as:

$$c = 40.207 + 63.45\phi \tag{6.29}$$

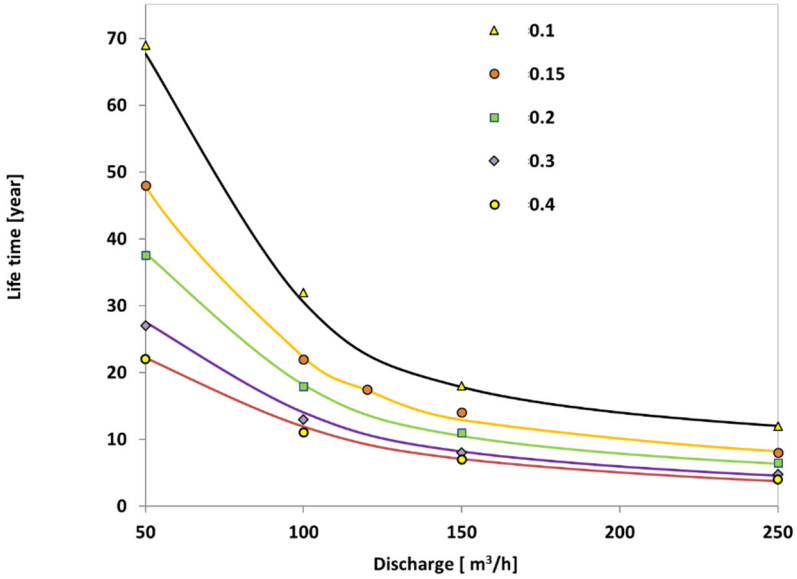

Figure 6-27. Lifetime as a function of discharge rate and porosity. Legend shows porosity values.

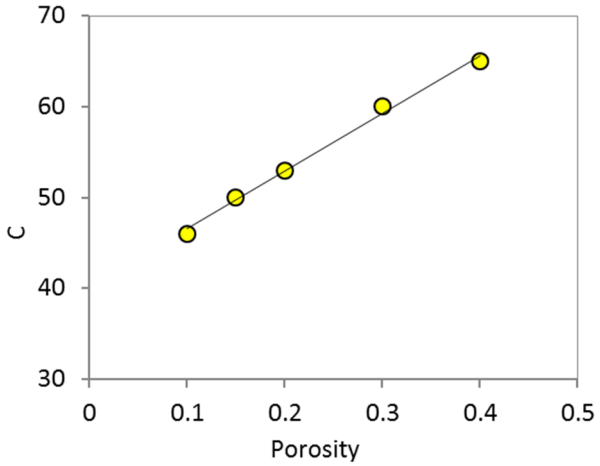

Figure 6-28. Parameter *c* as a linear function of porosity

Collecting all terms together, gives:

$$L_1 = \frac{1.125}{\phi}\left(1 + 14.7e^{-Q/(63.45\phi + 40.207)}\right) \tag{6.30}$$

in which L_1 is the system's lifetime [years], which is a function of discharge Q [m^3/h] and reservoir porosity n. This relationship represents the base model that needs to be modified to include the well spacing, the reservoir initial temperature and the injection temperature. This is developed in the following sections.

6.5.2 Lifetime as a function of porosity, discharge and well spacing

As explained in section 6.4.5, well spacing is an important parameter that needs to be taken into consideration in the design and lifetime prediction of a low-enthalpy hydrothermal system. It has a linear relationship with lifetime, as has been shown in Figure 6-19. In order to add its effect to Eq.(6.30), a series of simulations were carried out.

Four cases have been defined based on the base case with 4 different well spacings (1000, 1750, 2000, and 2500 [m]). Discharge rate has been altered in these four cases to 50, 100, 150, and 250 [m^3/h]. In all these 16 cases, the lateral location of the production well has been varied, while its depth, and thus the initial temperature, is kept constant. Figure 6-29 shows the results for these different sets and the fitted curves.

By inspecting the curves in Figure 6-29, it can be seen that they have a similar exponential decay as that in Eq. (6.30). Therefore, the effect of the well spacing can be readily included by multiplying the lifetime equation by a factor. For this, Eq. (6.30) has been utilized together with a multiplier to enable the fitting to the data sets. The multipliers for each fitting curve have been plotted versus well spacing in Figure 6-30. This figure shows a linear relationship between the multipliers and the well spacing, that can be described as

$$M_{ws} = 1.672 \times 10^{-3} ws - 0.668 \tag{6.31}$$

Adding this multiplier to Eq. (6.30) gives

$$L_2 = M_{ws} L_1 \tag{6.32}$$

in which L_2 is the lifetime of the reservoir as a function of discharge, porosity and well spacing *ws*[m].

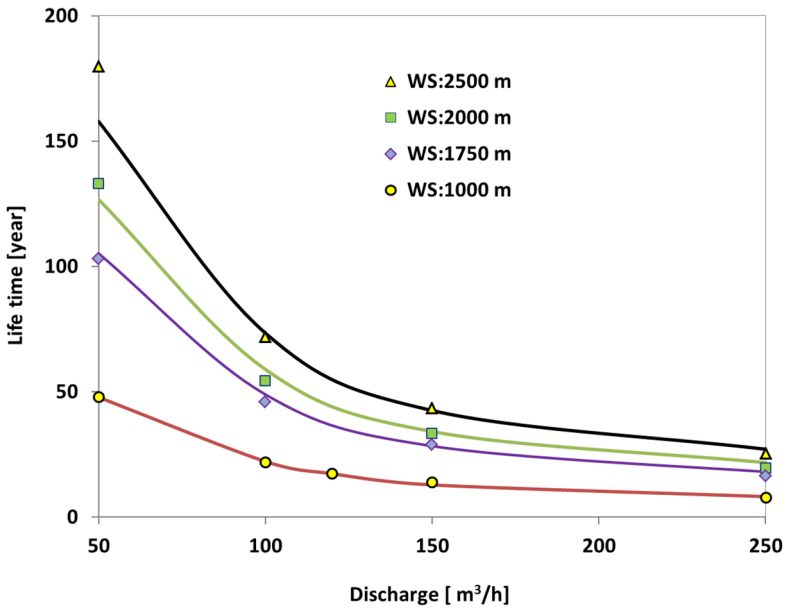

Figure 6-29. Lifetime as a function of discharge and well spacing

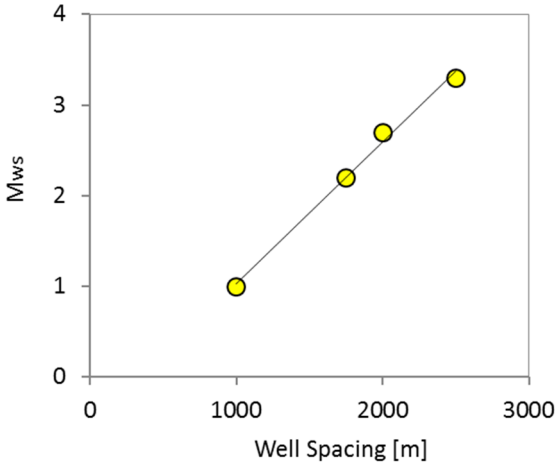

Figure 6-30. Relation between multiplier and well spacing at reservoir level

6.5.3 Lifetime as a function of discharge, porosity, well spacing and initial temperature

As has been shown in section 6.4.1, the initial temperature of the reservoir plays an important role in the heat transfer process in the system, and therefore on its lifetime. Figure 6-12 shows that system's lifetime has a linear relationship with the initial reservoir temperature.

Similar to the well spacing effect, the effect of the reservoir initial temperature can be included in the model by factoring Eq. (6.32) by a multiplier. Scenarios A to I, introduced in section 6.4.1, are utilized for this purpose. The multipliers are obtained by adjusting the curves to fit the different combinations of initial temperature and discharge. Figure 6-31 shows a linear relationship between the fitted multipliers and the reservoir initial temperatures. The initial temperature of the reservoir is taken as the average between, in the case of an inclined reservoir, the top and bottom temperature of the reservoir. This relationship can be described as:

$$M_{T_r} = 0.0415 T_r - 1.7635 \tag{6.33}$$

in which T_r [°C] is the average initial reservoir temperature. The multiplier is added to Eq. (6.32) to give the lifetime as a function of discharge, porosity, well spacing, and average initial reservoir temperature, i.e.

$$L_3 = M_{Tr} L_2 \tag{6.34}$$

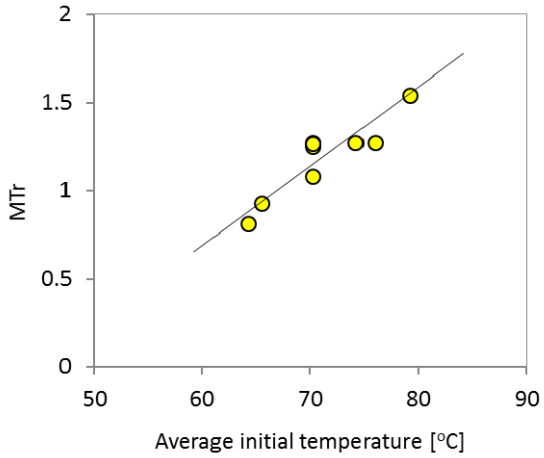

Figure 6-31. Relation between multiplier and initial reservoir average temperature

6.5.4 Lifetime as a function of discharge, porosity, well spacing, initial temperature and injection temperature

The variation of the system's lifetime with the injection temperature has been discussed in Section 6.4.4. Figure 6-18 shows that, as the injection temperature increases, the lifetime of the system increases.

Similar to the previous cases, Eq. (6.34) is utilized together with a multiplier to predict the lifetime as a function of discharge, porosity, well spacing, initial temperature and injection temperature. The scenarios given in section 1.3.4 are utilized for this purpose. The fitted multipliers are plotted versus the injection temperature in Figure 6-32. Apparently there is an exponential relationship between the multiplier and injection temperature that can be expressed as:

$$M_{T_{inj}} = 0.96621 + 0.0002112\, e^{(0.16103 * T_{inj})} \tag{6.35}$$

in which T_{inj} [°C] is the injection temperature and M_{Tinj} is the multiplier. This multiplier is incorporated in Eq. (6.34), giving:

$$L_4 = M_{T_{inj}} L_3 \tag{6.36}$$

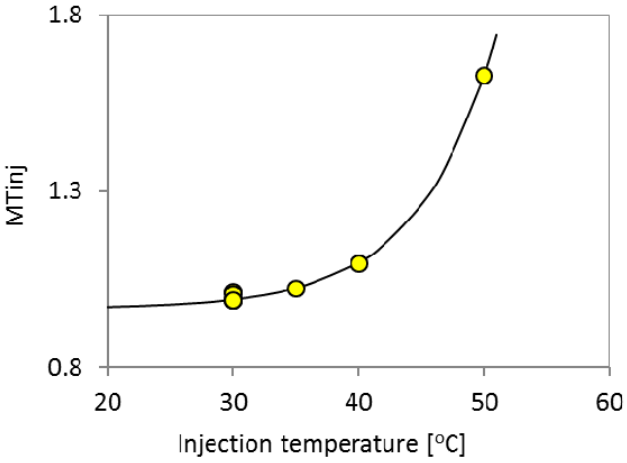

Figure 6-32. Relation between multiplier and injection temperature

6.6 A design model

Collecting all terms, a prototype design model describing the system lifetime as a function of discharge, porosity, well spacing, initial temperature and injection temperature, is given as

$$L = M_{ws}\, M_{Tr}\, M_{T_{inj}}\, \frac{1.125}{\phi}\left(1+14.7e^{-Q/(63.45n+40.207)}\right) \qquad (6.37)$$

in which

$$M_{ws} = 1.672\times10^{-3}\, ws - 0.668$$

$$M_{T_r} = 0.0415\, T_r - 1.7635$$

$$M_{T_{inj}} = 0.96621 + 0.0002112\; e^{(0.16103*T_{inj})}$$

6.7 Model verification

All scenarios that have been utilized in the parametric analysis and their lifetimes calculated using COMSOL, are re-calculated here using the proposed

design model (Eq. (6.37)). The calculated lifetimes from both techniques are plotted versus the lifetime in a logarithmic scale in Figure 6-33 (yellow circles). The figure clearly shows that there is a good match between the two models.

Using an average error of the form:

$$\text{average error} = \frac{1}{i}\sum_{0}^{i}\frac{\left|L_{\text{numerical model}} - L_{\text{proposed model}}\right|}{L_{\text{numerical model}}} \tag{6.38}$$

where *i* is the total number of cases, the average error for all the data points in Figure 6-33 is within 7%.

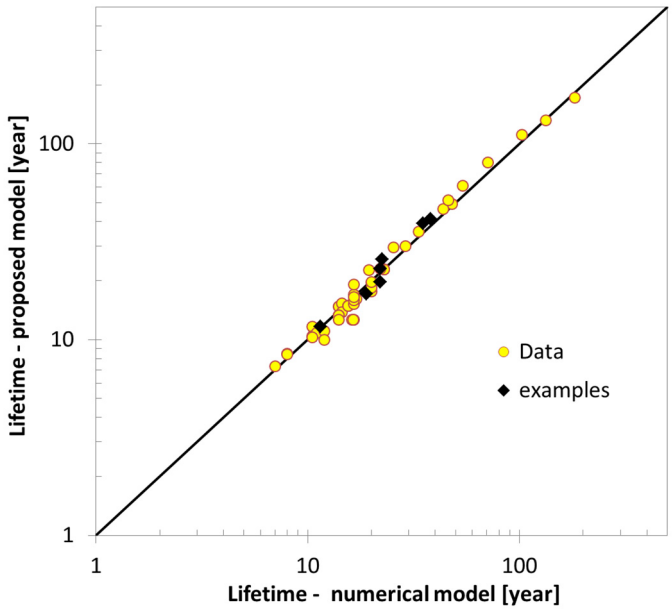

Figure 6-33. Lifetime calculated by proposed model versus lifetime calculated by numerical model

To verify the proposed model (Eq. (6.37)) against scenarios not considered in the curve fitting, a couple of extra scenarios have been modeled numerically and their lifetimes are compared with the value calculated by Eq. (6.37). Table 6-5 shows the configuration of these examples. The lifetimes of these scenarios are included in Figure 6-33 and are shown as black diamonds. The figure shows that they have a reasonable match, with an average error of 9%.

Table 6-5. Examples configuration

Example	Porosity	Well spacing	Discharge rate	average reservoir temperature	Injection temperature	lifetime-numerical model	lifetime-proposed model
	[ ]	[m]	[m3/h]	[^{o}C]	[^{o}C]	[year]	[year]
1	0.25	2500	200	70.2	30	22	23.0
2	0.18	1800	110	70.2	30	38	41.3
3	0.22	1600	100	70.2	40	35	39.3
4	0.15	1000	100	70.2	40	22.5	25.7
5	0.15	1000	150	79.2	40	22	19.7
6	0.15	1000	150	74.2	40	19	17.0
7	0.15	1000	150	64.2	40	11.5	11.7

6.8 Model limitation

Overall, it can be concluded that the proposed model is capable of predicting the lifetime of a low-enthalpy geothermal system with less than 10% error. However, it is notable that the proposed model is only valid for the range of parameters which has been assessed in the parametric analysis. Beyond this range, the model might not be valid. The parameters ranges are:

- Porosity: from 0.1 to 0.4
- Discharge: from 50 to 250 [m^3/h]
- Well spacing: from 1000 to 2500 [m]
- Average initial temperature: from 65 to 80 [^{o}C]
- Injection temperature: from 30 to 50 [^{o}C]
- Lifetime temperature limit: 60 [^{o}C]

Therefore, in order to cover a wider range, other cases with different scenarios need to be studied using the same modeling techniques as given in the previous section.

6.9 Conclusion

In this chapter, a new prototype design model for deep low-enthalpy hydrothermal systems is introduced. The model predicts, empirically, the lifetime of a hydrothermal system as a function of reservoir porosity, discharge rate, well spacing, average initial temperature of the reservoir, and

injection temperature. The finite element package COMSOL was utilized to conduct an extensive parametric analysis for a wide range of physical parameters and operational scenarios, for typical hydrothermal regional geometries, from which empirical mathematical relationships were derived to formulate the model.

To facilitate the parametric analysis, a hybrid modelling technique coupling 1D to 2D and 3D physical geometries has been adopted. This has reduced the number of finite elements, typically needed for such a case, significantly.

Three advantages can be deduced from this work:

- Providing geothermal engineers and decision makers a simple empirical calculation tool capable of giving them a preliminary conjecture about the lifetime of a deep low-enthalpy hydrothermal system.
- Introduction of a modelling technique that can be utilized to derive more elaborate models which cover more parameters and a wider range of applications.
- Identification of the significant and insignificant parameters influencing geothermal production.

Based on the parametric analysis, it can be concluded that:

- The discharge has the most significant effect on the project lifetime.
- The seasonal variation of injection temperature does not make a significant difference on the average heat and mass flow in the production well.
- Accurate knowledge of the reservoir initial temperature, independently of the reservoir depth and inclination, is very important in geothermal reservoir modelling.

Chapter 7

Conclusions and recommendations

In this thesis, an intensive experimental-numerical study has been conducted for an in-depth understanding of heat flow in a low-enthalpy hydrothermal system. A deep understanding of the physics of a geothermal system is indispensable for a safe, economic and viable project. In a typical hydrothermal system, heat conduction and convection take place inside a complicated and highly disproportionate geometry. This combination of physical processes and geometry makes the numerical analysis of such a system challenging, due to the high computer storage and run-time requirements. In developing numerical tools for geothermal systems, important efforts are devoted to tackling the discretization of two main issues: geometry and heat convection. Deep geothermal systems consist of very slender wellbores embedded in a vast soil mass. This geometrical peculiarity exerts an enormous computational burden, as a combination of very fine elements (cells) and coarse elements (cells) is normally needed to discretize the physical domain. For three-dimensional systems, this normally requires hundreds of thousands to millions of elements, necessitating parallel computing using multiple processor computers and making the CPU times unrealistic for engineering practice. Additionally, heat flow in a hydrothermal system involves density and viscosity variation with temperature, and thermal dispersion, making the numerical analysis even more complicated. In optimizing a geothermal system, these geometrical features and phenomena must be well understood and taken into consideration.

In this thesis, these physical and geometrical issues have been studied experimentally and numerically. The objectives of this thesis are:

1. Investigating the variation of the formation fluid density and viscosity with temperatures typically existing under hydrothermal conditions.
2. Investigating thermal dispersion due to heat flow in a porous domain.
3. Establishing a discretization technique that covers all important features of the hydrothermal system geometry and physical processes, and, at the same time, is computationally efficient so that it can be run on a normal PC (500 MHz, 4GB RAM).
4. Formulating a prototype model for a preliminary estimation of the reservoir lifetime, by knowing its porosity and initial temperature for different design parameters, namely, discharge, well spacing and injection temperature.

An experimental-numerical study is conducted to analyze heat transport in a porous domain subjected to cold and hot injection scenarios. The experimental set-up and initial and boundary conditions are made similar to those existing in a natural low-enthalpy geothermal system. The focus was placed on the nonlinear behavior of the fluid density and viscosity due to temperature variation, and their effect on heat and fluid flow and the thermal front shape inside the porous medium. The experimental set-up consists of a fully saturated sand layer surrounded by two impermeable clay layers, subjected to different fluid flow rates and injection temperatures. Vertical and horizontal test set-ups were utilized. Measurements showed that, in the horizontal experiments, the heat front was asymmetric, and, in the vertical experiments, it was symmetric. This behavior strongly indicates the effect of buoyancy due to fluid density and viscosity variation with the temperature range of the experimental set-up.

To quantify the effect of density, viscosity and thermal dispersion on heat flow, all experiments have been numerically modeled. A backcalculation study comparing the numerical to the experimental results was conducted. The backcalculation results revealed that, within the range of the studied Darcy velocity, thermal dispersion in the vertical tests was very small and increases linearly with fluid velocity; but thermal dispersion in the horizontal experiments was more significant and increases nonlinearly with fluid velocity. Furthermore, thermal dispersion in the horizontal experiments exhibited different behavior in the hot injection scenario than in the cold injection scenario. In the horizontal hot injection scenario, the longitudinal dispersion was more significant than the transversal dispersion. In contrast, in the

horizontal cold injection scenario, the transversal thermal dispersion was more significant. Based on these results, a thermal dispersion constitutive model was developed. This model is a function of flow rate, density, viscosity and pore geometry. It is capable of describing longitudinal and transversal thermal dispersion in a porous domain, taking into consideration the opposite behavior of thermal dispersion observed during hot and cold injection scenarios.

Three numerical models have been developed in this thesis: a computational model and two empirical models. The models are respectively:

1. A transient conduction-convection computational model for heat flow in coaxial wellbores, including thermal resistances between the tubing materials and thermal interaction with the soil formation.
2. A thermal dispersion model, which is a function of flow rate, density, viscosity and pore geometry.
3. A prototype design model capable of predicting, empirically, the lifetime of a hydrothermal system as a function of reservoir porosity, discharge rate, well spacing, average initial temperature of the reservoir, and injection temperature.

The finite element method is utilized for modeling heat flow in the experimental set-up and in typical hydrothermal reservoir geometry and physical conditions. The finite element package COMSOL was utilized as a framework for this purpose. The above mentioned numerical models developed in this thesis are implemented in COMSOL and coupled to its standard features, including the finite element mesh generation and solvers, together with its pre- and post-processing facilities.

Analyzing the above mentioned physical parameters and processes using standard finite element discretization requires vary large mesh sizes with large CPU times that can hamper modeling efforts and limit the number of studied cases. To tackle this problem, a combination of 1D, 2D and 3D numerical geometries describing different parts of the system are utilized and coupled. The wellbore geometry is modeled using 1D elements, yet the physical processes of heat conduction and convection in all involved components, and their thermal interactions, are taken into consideration in a pseudo 3D modeling technique. The reservoir is modelled as a 3D geometry and the surrounding soil formations as a 2D geometry. The 1D-2D-3D model is computationally efficient due to the enormous reduction in the number of the

required finite elements. As a result of the computational efficiency and accuracy, the proposed model provides the tool for more insight into heat flow in deep low-enthalpy hydrothermal systems.

As a result of this intensive study, a prototype model is developed that accounts for the most significant factors affecting the lifetime of a hydrothermal system. The model predicts, empirically, the lifetime of a hydrothermal system as a function of reservoir porosity, discharge rate, well spacing, average initial temperature of the reservoir, and injection temperature

The model is straightforward and can be utilized as a pre-design tool in the preliminary decision making process.

7.1 Recommendations

In spite of the intensive experimental—numerical study that has been conducted in this thesis, there are still some questions that should be addressed in future research, including:

- Experimentally studying thermal dispersion under a wider range of temperature and velocity variations.
- Considering the thermo-mechanical and thermo-chemical mechanisms in computational models.
- Considering geological complexities such as heterogeneity and fracture mechanisms in computational models.
- Elaborating the prototype model to cover a wider range of parameters. Issues that could be investigated include a wider range of reservoir initial temperatures, a wider range of the injection temperature, reservoir thickness, and the reservoir lifetime limit.

References

Adams, J.J., Bachu, S. "Equations of state for basin geofluids: algorithm review and intercomparison for brines." Geofluids 2(4), 2002: 257-271.

Al-Khoury, R. "Computational Modeling of Shallow Geothermal Systems", CRC Press/Balkema. 2012. 233pp.

Al-Khoury, R., Bonnier, P.G. "Efficient finite element formulation for geothermal heating systems. Part II: transient." International journal for numerical methods in engineering 67(5) (2006): 725-745.

Al-Khoury, R., Bonnier, P.G., Brinkgreve, R.B.J. "Efficient finite element formulation for geothermal heating systems. Part I: steady state." International journal for numerical methods in engineering 63(7) (2005): 988-1013.

Anderson, M.P. "Heat as a ground water tracer.", Ground water, 43(6), 2005: 951-968.

Bakos, G.C. "Low enthalpy geothermal energy for greenhouse heating at Nea Kessani Xanthi, Greece." Energy Sources, Part A: Recovery, Utilization, and Environmental Effects, 29(6), 2007: 571-579.

Barends, F.B.J. "Complete Solution for Transient Heat Transport in Porous Media Following Lauwerier." SPE Annual Technical Conference and Exhibition. Society of Petroleum Engineers, 2010.

Barends, F.B.J., Saeid, S. "Physical aspects of heat transport in porous media." First International Conference on Frontiers in Shallow Subsurface Technology, Delft, 2010.

Battistelli, A., Claudio C., Pruess, K. "The simulator TOUGH2/EWASG for modelling geothermal reservoirs with brines and non-condensible gas." Geothermics, 26(4), 1997: 437-464.

Batty, W.J., Probert, S.D., Ball, M., O'Callaghan, P.W. "Use of the thermal-probe technique for the measurement of the apparent thermal conductivities of moist materials." Applied energy, 18(4), 1984: 301-317.

Batzle, M., Wang, Z. "Seismic properties of pore fluids."Geophysics, 57(11), 1992: 1396-1408.

Bear, J., Bachmat, Y. “Introduction to modeling of transport phenomena in porous media.” Vol. 4. Springer, 1990.

Bear, J., Cheng, A. H-D. “Modelling groundwater flow and contaminant transport”, Springer, 23, 2010: 834.

Bedre, M.G., Anderson, B.J. "Sensitivity analysis of low-temperature geothermal reservoirs: effect of reservoir parameters on the direct use of geothermal energy: Geothermal Resources Council Transactions.", Geothermal Resources Council 2012 Annual Meeting, 2012, Vol.36: 1255-1262

Bhat, A., Swenson, D., Gosavi S. "Coupling the HOLA wellbore simulator with TOUGH2.” Proceedings of the 20th workshop on geothermal reservoir engineering. Stanford University, Stanford, California. 2005.

Bjornsson, G. , Bodvarsson, G.S. “A Multi-feedzone Geothermal Wellbore Simulator.”, Geothermal Resources Council Trans 11, 1987: 503-507.

Blöcher, M.G., Zimmermann, G., Moeck I., Brandt, W., Hassanzadegan, A., Magri, F. "3D numerical modeling of hydrothermal processes during the lifetime of a deep geothermal reservoir." Geofluids, 10(3), 2010: 406-421.

Brill, J.P., Mukherjee, H. “Multiphase flow in wells.” Richardson, Tex.: Henry L. Doherty Memorial Fund of AIME, Society of Petroleum Engineers, 1999.

Brouwer, G.K., Lokhorst A., Orlic, B. "Geothermal heat and abandoned gas reservoirs in the Netherlands." In Proceedings World Geothermal Congress, 2005: pp. 24-29.

Chandrasiri Ekneligoda, T., Min, K.B. “Determination of optimum parameters of doublet system in a horizontally fractured geothermal reservoir.” Renewable Energy, 65, 2013: 152–160.

Chen, S.X. "Thermal conductivity of sands.” Heat and Mass Transfer, 44(10), 2008: 1241-1246.

Churchill, S.W. "Friction-factor equation spans all fluid-flow regimes.” Chemical Engineering, 84(24), 1977: 91-92.

Clauser, C., “Geothermal Energy”, In: K. Heinloth (ed), Landolt-Börnstein, Group VIII: Advanced Materials and Technologies, Vol. 3: Energy

Technologies, Subvol. C: Renewable Energies, Springer Verlag, Heidelberg-Berlin, 2006. DOI: 10.1007/10858992_20.

COMSOL multiphysics, User's guid Version 4.2a, 2011, 1166pp.

De Marsily, G. "Flow of miscible fluids: Dispersion, retention, and heat transfer.", Quantitative hydrogeology: Groundwater hydrology for engineers. Academic Press, San Diego, 1986: 278-281.

Dickson, M. H., Fanelli, M. “Geothermal energy: utilization and technology.” Routledge, 2013.

Diersch, H.J., Kolditz, O. "Variable-density flow and transport in porous media: approaches and challenges." Advances in Water Resources, 25(8), 2002: 899-944.

Elbashbeshy, E.M.A., Bazid, M. A. A. "The effect of temperature-dependent viscosity on heat transfer over a continuous moving surface." Journal of Physics D: Applied Physics, 33 (21), 2000: 2716.

Fossoul, F., Orban, P., Dassargues, A. "Numerical simulation of heat transfer associated with low enthalpy geothermal pumping in an alluvial aquifer." Geologica Belgica, 14(1-2), 2011.

Franco, A., Vaccaro, M. "Numerical simulation of geothermal reservoirs for the sustainable design of energy plants: A review."Renewable and Sustainable Energy Reviews, 30, 2014: 987-1002.

Greenberg, D.B., Cresap, R.S., Malone, T.A. "Intrinsic permeability of hydrological porous mediums: Variation with temperature.", Water Resources Research, 4(4), 1968: 791-800.

Gudmundsdottir, H., Jonsson, M. T., Palsson, H. "Coupling wellbore simulator with reservoir simulator." Proceeding, 37th Workshop on Geothermal Reservoir Engineering, Stanford University, Stanford, California, 2012.

Gunn, C., Freeston, D., “An integrated steady-state wellbore simulation and analysis package.” Proceeding 13th New Zealand Geothermal Workshop, 1991: 161-166.

Gunn, C.I.M., Freeston, D. H., Hadgu, T. "Principles for wellbore simulator validation and calibration using matching analysis—I. Analytical techniques."Geothermics, 21(3), 1992: 341-361.

Gupta, H.K., Roy, S. “Geothermal energy: an alternative resource for the 21st century.” Elsevier, 2006.

Hadgu, T., Zimmerman, R.W., Bodvarsson, G.S. "Coupled reservoir-wellbore simulation of geothermal reservoir behavior." Geothermics, 24(2), 1995: 145-166.

Hecht-Méndez, J., Molina-Giraldo, N., Blum, P., Bayer, P. "Evaluating MT3DMS for heat transport simulation of closed geothermal systems." Ground water, 48(5), 2010: 741-756.

Hidalgo, J.J., Carrera, J., Dentz, M. "Steady state heat transport in 3D heterogeneous porous media." Advances in water resources, 32(8), 2009: 1206-1212.

Hopmans, J.W., Šimunek, j., Bristow, K.L. "Indirect estimation of soil thermal properties and water flux using heat pulse probe measurements: Geometry and dispersion effects." Water Resources Research, 38(1), 2002: 7-1.

Hsu, C.T., Cheng, P. "Thermal dispersion in a porous medium", International Journal of Heat and Mass Transfer, 33(8), 1990: 1587-1597.

Ingebritsen, S.E., Stanford, W.E. "Groundwater in geologic processes." Cambridge University Press, 1999.

Kaltschmitt, M., Streicher, W., Wiese, A. "Renewable Energy: Technology, Economics and Environment", Springer, 2007. p. 596.

Kiryukhin, A.V. "Modeling studies: the Dachny geothermal reservoir, Kamchatka, Russia." Geothermics, 25(1), 1996: 63-90.

Kiryukhin, A.V., Yampolsky V.A. "Modeling study of the Pauzhetsky geothermal field, Kamchatka, Russia." Geothermics, 33(4), 2004: 421-442.

Klaus, H., "Advanced materials and technologies - Energy Technologies", Springer, 2006. Vol. 3.

Kocabas, I. "Thermal transients during nonisothermal fluid injection into oil reservoirs." Journal of Petroleum Science and Engineering, 42(2), 2004: 133-144.

Lauwerier, H.A. "The transport of heat in an oil layer caused by the injection of hot fluid." Applied Scientific Research, 5(2-3), 1955: 145-150.

Lide, E., David, R., "CRC Handbook of Chemistry and Physics, 90th Edn." CRC Press., Boca Raton (FL), 1990 (version 2010), 2760 pp.

Lighty, J.S., Silcox, G.D., Pershing, D.W., Cundy, V.A., Linz, D.G. "Fundamentals for the thermal remediation of contaminated soils. Particle and bed

desorption models." Environmental science & technology, 24(5), 1990: 750-757.

Lin, S., Kwok, C.C.K., Li, R-Y., Chen, Z-H., Chen, Z-Y. "Local frictional pressure drop during vaporization of R-12 through capillary tubes." International Journal of Multiphase Flow, 17(1), 1991: 95-102.

Livescu, S., Durlofsky, L.J., Aziz, K., Ginestra, J. C. "A fully-coupled thermal multiphase wellbore flow model for use in reservoir simulation." Journal of Petroleum Science and Engineering, 71(3), 2010: 138-146.

Lu, X., Ren, T., Gong, Y. "Experimental investigation of thermal dispersion in saturated soils with one-dimensional water flow." Soil Science Society of America Journal, 73(6), 2009: 1912-1920.

Ma, R., Zheng, C. "Effects of density and viscosity in modeling heat as a groundwater tracer." Ground water, 48(3), 2010: 380-389.

Metzger, T., Didierjean, S., Maillet, D. "Optimal experimental estimation of thermal dispersion coefficients in porous media.", International Journal of Heat and Mass Transfer, 47(14), 2004: 3341-3353.

Molina-Giraldo, N., Bayer, P., Blum, P. "Evaluating the influence of thermal dispersion on temperature plumes from geothermal systems using analytical solutions." International Journal of Thermal Sciences, 50(7), 2011: 1223-1231.

Mori, Y., Hopmans, J.W., Mortensen, A.P., Kluitenberg, G.J. "Estimation of vadose zone water flux from multi-functional heat pulse probe measurements." Soil Science Society of America Journal, 69(3), 2005: 599-606.

Mottaghy, D., Pechnig, R., Vogt, C. “The geothermal project Den Haag: 3D numerical models for temperature prediction and reservoir simulation.” Geothermics, 40(3), 2011:199-210.

Nick, H.M., Schotting, R., Gutierrez-Neri, M., Johannsen, K. “Modeling transverse dispersion and variable density flow in porous media.” Transport in porous media, 78(1), 2009: 11-35.

Nield, D.A., Bejan, A. Convection in porous media. springer, 2006.

Nixon, J.F. "The role of convective heat transport in the thawing of frozen soils." Canadian Geotechnical Journal, 12(3), 1975: 425-429.

Ogata, A., Banks, R.B. "A solution of the differential equation of longitudinal dispersion in porous media." US Geological Survey, 1961.

Pollock, D.W. "Simulation of Fluid Flow and Energy Transport Processes Associated With High-Level Radioactive Waste Disposal in Unsaturated Alluvium." Water Resources Research, 22(5), 1986: 765-775.

Rau, G.C., Andersen, M.S., Acworth, R. I. "Experimental investigation of the thermal dispersivity term and its significance in the heat transport equation for flow in sediments.", Water Resources Research, 48(3) 2012.

Saeid, S., Al-Khoury, R., Barends, F.B.J. "An efficient computational model for deep low-enthalpy geothermal systems.", Computers & Geosciences, 51, 2013: 400-409. ISSN 0098-3004.

Saeid, S., Al-Khoury, R., Nick, H.M., Barends, F.B.J. "Experimental–numerical study of heat flow in deep low-enthalpy geothermal conditions." Renewable Energy 62, 2014: 716-730.

Saeid, S., Al-Khoury, R., Nick, H.M., Hicks, M.A. "A prototype design model for deep low-enthalpy hydrothermal systems." Renewable Energy 77, 2015: 408-422. ISSN 0960-1481.

Saeid, S., Barends, F.B.J. "An extension of Lauwerier's Solution for heat flow in saturated porous media." COMSOL Conference Milan, 2009.

Saeid, S., Barends, F.B.J. "Density and viscosity effects on thermal transport." EAGE, 1st Sustainable Earth Sciences Conference & Exhibition (SES). 2011.

Salimi, H., Groenenberg, R., Wolf, K-H.A.A "Compositional flow simulation of mixed CO2-Water injection into geothermal reservoirs: Geothermal energy combined with CO2 storage, Thirty-Sixth Workshop on Geothermal Reservoir Engineering Stanford University, 2011.

Sauty, J. P., Gringarten, A. C., Landel, P. A., & Menjoz, A. (1980). "Lifetime optimization of low enthalpy geothermal doublets." In Advances in European Geothermal Research, Springer Netherlands, 1980: 706-719

Sauty, J., Gringarten, A., Menjoz, A., and Landel, P., "Sensible energy storage in aquifers: 1. Theoretical study," 18(1), 1982: 245-252.

Schulz, R. "Analytical model calculations for heat exchange in a confined aquifer." Journal of Geophysics-Zeitschrift fur Geophysik, 61(1), 1987: 12-20.

Simmons, C.T. “Variable density groundwater flow: From current challenges to future possibilities”, Hydrogeology Journal, 13(1), 2005.

Sippel, J., Fuchs, S., Cacace, M., Braatz, A., Kastner, O., Huenges, E., Scheck-Wenderoth, M. “Deep 3D thermal modelling for the city of Berlin (Germany).” Environmental Earth Sciences, 70(8), 2013: 3545-3566.

Smith, L., Chapman, D.S. "On the thermal effects of groundwater flow: 1. Regional scale systems.", Journal of Geophysical Research, 88(B1), 1983: 593-608.

Van der Poel, J.T., Schenkeveld, F.M. "A preparation technique for very homogenous sand models and CPT research." Tokyo: Centrifuge. 98(1), 1998.

Van Genuchten, M. Th. “Analytical solutions for chemical transport with simultaneous adsorption, zero-order production and first-order decay” Journal of Hydrology, 49(3), 1981: 213-233.

Van Poollen, H.K. "Fundamentals of enhanced oil recovery." Tulsa: Pennwell Corp, 1980.

Vandenbohede, A., Louwyck, A., Lebbe, L. "Conservative solute versus heat transport in porous media during push-pull tests.” Transport in porous media, 76(2), 2009: 265-287.

Vogt, C., Iwanowski-Strahser, K., Marquart, G., Arnold, J., Mottaghy, D., Pechnig, R., Clauser, C. “Modeling contribution to risk assessment of thermal production power for geothermal reservoirs.” Renewable Energy, 53, 2013: 230-241.

Watanabe, N., Wang, W., McDermott, C.I., Taniguchi, T., Kolditz, O. “Uncertainty analysis of thermo-hydro-mechanical coupled processes in heterogeneous porous media.” Computational Mechanics, 45(4), 2010: 263-280.

Wolf, K. A., Willemsen, A., Bakker, T. W., Wever, A. K. T., Gilding, D. T.”The Development of a Multi-purpose Geothermal Site in an Urban Area.” In 70th EAGE Conference & Exhibition, 2008.

Wong, T. E., Batjes, D. A., & de Jager, J. (Eds.). “Geology of the Netherlands.” Amsterdam: Royal Netherlands Academy of Arts and Sciences, 2007, pp. 341-346.

Woodbury, A.D., Smith, L. "On the thermal effects of three-dimensional groundwater flow." Journal of Geophysical Research: Solid Earth, 90(B1), 1985: 759-767.

Zalba, B., Marín, J.M., Cabeza, L.F., Mehling, H. "Review on thermal energy storage with phase change: materials, heat transfer analysis and applications." Applied thermal engineering, 23(3), 2003: 251-283.

List of mathematical symbols

Symbol	Definition	Unit
A	Area	[m^2]
A_L	Longitudinal thermal dispersion coefficient	[m]
A_T	Transversal thermal dispersion coefficient	[m]
b	Reciprocal of the contact resistance between two objects	[W/m^2K]
B	Fluid viscosity at T = 0 [°C]	[Pa.s]
Bl	Bleeding number	[-]
c	Heat capacity	[J/kg.K]
C	Concentration	[mol/m^3]
d	Tubing/pipe diameter	[m]
D	Thermal diffusivity, depth, diameter	[m^2/s], [m], [m]
D_{10}	Grain diameter	[m]
e	Surface roughness	[m]
E	Annual thermal energy extracted	[W/year]
error	Error	[-]
f_D	Darcy friction factor	[-]
g	Gravity	[m/s^2]
H	Height, Thickness	[m],[m]
J	Water flux	[m/s]
k	Intrinsic permeability , fitting parameter related to soil texture	[m^2], [-]
K	Hydraulic conductivity	[m/s] or [mD]
L	Characteristic length of the reservoir/element , lifetime	[m], [year]
M	Multiplier	[-]
$\dot{m}$	total mass production of hot water per year	[kg/year]
n	Normal vector to the surface	[-]
Nu	Nusselt number	[-]
P	Pressure	[Pa] or [N/m^2]
Pe	Peclet number	[-]
Pr	Prandtl number	[-]
q	Darcy velocity , Flux	[m/s]

Q	Discharge , heat source/sink	[m^3/h], [W/m^3]
r	Radius	[m]
R	Thermal resistance between two materials	[m^2K/W]
R_d	Retardation factor	[-]
Re	Reynolds number	[-]
S	Surface, salinity	[m^2], [ppm]
t	Time	[s]
T	Temperature	[K] or [°C]
u	Fluid velocity	[m/s]
v	Velocity	[m/s]
V	Volume, velocity	[m^3], [m/s]
ws	Well spacing	[m]
x	X-direction	[-]
y	Y-direction	[-]
z	Z-direction, depth	[-], [m]
α	Thermal dispersion coefficient, constant	[m], [-]
β	Thermal expansion coefficient, constant, Thermal dispersion coefficient	[1/K], [-], [m]
γ	Constant	[-]
δ	Lauwerier extension parameter	[-]
Θ	A fluid parameter describing the shape of the μ-T curve, wellbore inclination angle, constant	[1/°C], [°], [-]
λ	Thermal conductivity	[W/mK]
μ	Viscosity	[Pa.s]
ν	Kinematic viscosity	[m^2/s]
ρ	Density	[kg/m^3]
ϕ	Porosity	[-]

List of subscripts

Subscript	**Definition**
0	Initial condition
a	Acceleration
dis	Dispersion
f	Fluid, friction
eq	equivalent
g	Grout/cement
h	Hydrostatic
i	Injected condition, counter, inner
in	Input
inj	Injection
L,l	Longitudinal
out	Output
p	Pipe, production well
pro	Production
ref	Reference
S	Sand , soil formation
t	Adjacent layers
T,t	Transversal
w	Water

List of superscripts

Superscript	**Definition**
'	Adjacent layers
g	Gravitational acceleration
w	Well

Acknowledgment

The research presented in this dissertation has been conducted at the Geo-Engineering Section in the Faculty of Civil Engineering and Geosciences at Delft University of Technology. The research was mainly funded by TU Delft and partially by Deltares. I wish to extend my sincere gratitude to these organizations for their financial and technical support.

This research project started under the supervision of Professor Frans Barends. After three major changes in the research objective and scope, it was finally decided to conduct an experimental and numerical study of heat flow under low-enthalpy hydrothermal conditions. Unfortunately, Professor Frans Barends could not continue with supervising this project due to ill health. The research work continued under the supervision of Professor Michael Hicks, as the promoter, and Dr. Rafid Al-Khoury, as the daily supervisor.

I am very grateful to Frans Barends for his supervision and providing me the opportunity to conduct my experimental work in the Deltares Laboratory. Frans, thank you very much and I wish you good health and strength.

I would like to express my gratitude to my promoter, Michael Hicks, for his support and advice, and his careful review of the thesis. Mike, thank you very much for accepting being my promoter.

I would like to express my utmost gratitude to my daily supervisor, Rafid Al-Khoury. He supported me at the very special moment of my PhD period, when I was alone with no supervisor. His positive attitude and encouragement were essential in finalizing this research work. He shared with me a lot of his expertise and research insights. The brainstorming and discussions with him were always fruitful and led to key developments. His detailed comments on my publications were greatly appreciated. I doubt if I will ever be able to convey my appreciation fully, but I owe him my eternal gratitude. Rafid, thank you a million times for all your support!

I also would like to thank my PhD exam committee members for accepting taking part in this committee and for the valuable reviews.

The experimental part of this work required the professional assistance and support of the technicians at the Deltares Laboratory. Here, I would like to particularly thank Ferry Schenkeveld, who kindly helped me in setting up the experiment. His attention, precision and finesse were a key in the

experimental success. I am also thankful to Karel Heller from the Laboratory of Geoscience and Engineering at TU Delft for his wise, quick and sincere support and advice during my experimental work.

I would like to thank Dominique Ngan-Tillard for her involvement at the early stages of this project, and for giving me the opportunity to teach in a part of the "Site characterization, testing and physical modelling" course. That was a great experience for me. I am also grateful to Karl-Heinz Wolf for his support, advice, motivation, and providing me the opportunity to teach on the "Geothermal Energy" course; furthermore, for his careful editing of the translation of the summary of this manuscript.

A very sincere gratitude to Bert Sluys and all colleagues in the Computational Mechanics Group who kindly hospitalized me in their section. The friendly environment of this group is unforgettable. I would also like to thank all colleagues and staff members of the Geo-Engineering Section and Department of Geoscience and Engineering for all the friendship and moments that we shared.

I am so grateful to all my friends and colleagues who technically helped and supported me in this work; Hamidreza Salimi, John van Esch, Ruhi Farajzadeh, Saeed Hosseinzadeh, Mehdi Musivand, Salar Mostofizadeh, among the many others. In particular, I would like to acknowledge Hamid M. Nick for the useful discussions and contributions in two of my papers; moreover, for his positive attitude and motivation.

I would like also to thank all colleagues in SGS-Horizons; especially Leila Bagherian and Mehlika Tonga-Oner, who always emotionally supported and motivated me during the last two years. Also, I would like to thank Gijs Stradhoef for translating the summary of my dissertation and propositions into Dutch.

In addition, I would like to thank my dear friend Sara Fekri for her kind help for this book cover design and other illustrations in this dissertation.

Last, but not least, I most want to thank my dear family, my mom, dad, and brother, for their endless love, support, and understanding. Without them this doctoral degree would not have been possible. My special gratitude to my dear boyfriend, Sadegh, for his understanding, encouragement, endless support and for helping me to get through all the difficulties of my PhD study.